Ore Geology Reviews
July 2020, Volume 122, Pages 103550 (27p.)
https://doi.org/10.1016/j.oregeorev.2020.103550
https://archimer.ifremer.fr/doc/00624/73591/

Origin of the Oligocene manganese deposit at Obrochishte (Bulgaria): Insights from C, O, Fe, Sr, Nd, and Pb isotopes

Dekov Vesselin M. [1, 2, *], Barry Maynard J. [3], Kamenov George D. [4], Rouxel Olivier [2, 5], Lalonde Stefan [6], Juranov Sava [7]

[1] Department of Marine Resources and Energy, Tokyo University of Marine Science and Technology, 4-5-7 Konan, Minato-ku, Tokyo, Japan
[2] Unité de Géosciences Marines, IFREMER, Z.I. Pointe du diable, BP 70 - 29280, Plouzané, France
[3] Department of Geology, University of Cincinnati, P.O. Box 210013, Cincinnati, OH 45221-0013, USA
[4] Department of Geological Sciences, University of Florida, 241 Williamson Hall, Gainesville, FL 32611, USA
[5] Department of Oceanography, School of Ocean and Earth Science and Technology, University of Hawaii at Manoa, 1000 Pope Road, MSB 510, Honolulu, HI 96822, USA
[6] CNRS-UMR6538 Laboratoire Géosciences Océan, European Institute for Marine Studies, Technopôle Brest-Iroise, Place Nicolas Copernic, 29280 Plouzané, France
[7] Department of Geology and Paleontology, University of Sofia, 15 Tzar Osvoboditel Blvd., 1000 Sofia, Bulgaria

* Corresponding author : Vesselin M. Dekov, email address : vdekov0@kaiyodai.ac.jp

Abstract :

The large manganese (Mn) deposit at Obrochishte (NE Bulgaria) is part of a cluster of similar Early Oligocene deposits located around present-day Black Sea. They collectively constitute the Earth's second largest endowment of Mn, after the Kalahari Manganese Field in Africa. We have employed a battery of isotopic techniques (C, O, Fe, Sr, Nd, Pb) to help understand the genesis of this deposit. Carbon isotope data indicates that some sections of the Mn-ore layer have diagenetic MnCO3 mineralization, formed by reaction of Mn oxides with organic carbon (Corg), whereas other sections have MnCO3 precipitated directly from the seawater column. Oxygen isotopes show that the high-grade Mn mineralization had seawater as the fluid source, whereas some lower-grade sections had a mix of ground water and seawater as fluid sources. Sr and Nd isotope values of ore leachates also indicate that the Mn deposition occurred in normal Early Oligocene seawater. Nd and Pb isotope values suggest that the clastic host sediments were sourced from continental bedrock rather than younger arc volcanic rocks to the west. Iron isotope composition of the Mn ore implies deposition in a redox-stratified basin, similar to the modern Black Sea, with much of the Fe sequestered in deep, anoxic-euxinic water as sulfides. Similar to the modern Black Sea, most of the detrital Fe was transferred from shallow oxic sediments into deep, anoxic-euxinic water by an "iron shuttle" and remobilized Mn sequestered in the upper suboxic water layer. However, during the Oligocene, the "iron shuttle" operated intermittently due to the chemocline falling mostly below the shelf break, thereby limiting the efficiency of the shuttle mechanism. We propose a model for the Lower Oligocene strata in which intense weathering during the Eocene weathering phase produced a thick lateritic crust on the southern European continent. The drastic sea-level drop at the end of the Eocene initiated downcutting of streams through this weathered material, transferring Fe- and Mn-oxides to the redox-stratified Western Black Sea. Here, these oxides were partly or entirely dissolved in the suboxic

(Mn-oxides partly, Fe-oxyhydroxides entirely dissolved) and anoxic-euxinic (Mn-oxides entirely dissolved, dissolved Fe2+ re-precipitated) water layers. Eventually, Fe was re-precipitated as sulfide in the deep anoxic-euxinic water, while Mn accumulated in the suboxic water layer. Transgression in the Early Oligocene brought this Mn-rich water onto the shallow shelf where it precipitated as Mn-oxide, then converted to Mn-carbonates during early diagenesis. Some Mn was also contributed by submarine groundwater discharge. Further transgression brought lower-oxygen water onto the shelf and Mn-carbonate precipitated directly from the water column. The findings from this work provide insights about the unique Oligocene geochemical event in the region that lead to the formation of the 2nd largest cluster of Mn deposits in the world.

Graphical abstract

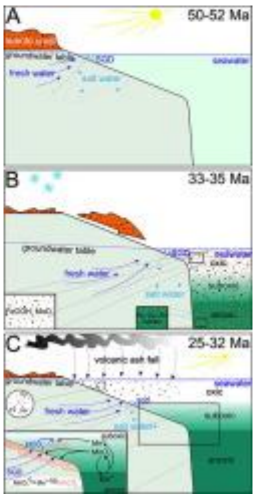

Highlights

►Mn-carbonate ore at the Obrochishte has dual origin: diagenetic and authigenic. ► Mn deposition was a result of the climatic events at the Late Eocene-Early Oligocene. ► Mn ore was deposited in a redox-stratified basin, similar to the modern Black Sea.

Keywords : Mn metallogenesis, C-O-Fe-Sr-Nd-Pb isotopes, Early Oligocene, submarine groundwater discharge, water column anoxia, proto-Black Sea geochemistry

1. Introduction

The Oligocene Mn deposit in north-east Bulgaria (known as Obrochishte, or in older literature as Varna deposit) is one of a group of large deposits of Oligocene age that encircle the Black Sea. These include the deposits from the Chiatura (Georgia), Laba (Russia), Nikopol and

Bol'shoy Tokmak deposits (Ukraine) and Binkiliç deposit (NE Turkey) (Varentsov, 2002; Kuleshov, 2003, 2017). Collective reserves of all of these deposits are on the order of 600×10^6 metric tons of Mn making this region the world's second largest repository of Mn, after the supergiant Kalahari Manganese Field of South Africa (Maynard, 2010; Beukes et al., 2016). Recent information on reserves at Obrochishte itself is scarce. One source (GIS/GEODE 2016) gives a figure of 16×10^6 metric tons at 28% Mn. Data in the USGS minerals yearbooks shows cumulative production in 1963-2016 was $2.2x10^6$ metric tons per year of ore with 28.6% Mn.

Mn-ore bed in outcrops (Vassilev et al., 1958; Stoyanov, 1961, 1963; Vangelova et al., 2005), in drill cores (Aleksiev, 1959; Stoyanov, 1961, 1963; Gnoevaya et al., 1982), and in mine sections (Obrochishte mine) in NE Bulgaria has been the subject of a number of studies aiming at shedding light on its geology (Mandev, 1954; Vassilev et al., 1958; Stoyanov, 1961, 1963; Bogdanova, 1968), sedimentology (Aleksiev, 1960b; Stoyanov, 1963; Aleksiev and Nacheva, 1966; Vangelova et al., 2005), mineralogy (Vassilev et al., 1958; Aleksiev and Nacheva, 1966; Vassilev, 1967; Bogdanova, 1968; Puliev and Alexiev, 1972; Milakovska et al., 2006; Atanasova et al., 2009), and major element geochemistry (Vassilev et al., 1958; Aleksiev and Nacheva, 1966; Vassilev, 1967; Puliev and Alexiev, 1972; Vangelova et al., 2005; Milakovska et al., 2006).

The comprehensive mineralogy work of Vassilev et al. (1958) found that the only primary Mn-minerals (and at the same time the major ore minerals) in the deposit were Ca-rhodochrosite and Mn-calcite. Less abundant Mn-oxyhydroxides were secondary minerals formed as weathering products on the primary Mn-carbonates (Vassilev et al., 1958). Thus, two Mn-ore types can be distinguished on the basis of major Mn minerals determined in the ore bed: carbonate (primary) and oxyhydroxide (secondary). Later studies (Aleksiev, 1960a; Aleksiev and Nacheva, 1966; Puliev and Alexiev, 1972) claimed that a part of some of the Mn-ore layers was composed of Mnsilicates (e.g., neotocite), but they did not provide any solid proofs for presence of these minerals in the deposit. (Neotocite was determined on the basis of: three unclear peaks at the Debye-Scherrer X-ray diffraction pattern, three peaks at the differential thermal curve, major element concentrations measured through unknown method, optical microscopy, and hand specimen description.) The results of these studies were accepted without any criticism by later workers and this led to creation and wide circulation of incorrect classifications of the major ore types in this deposit: e.g., Mn-carbonate, Mn-carbonate/Mn-silicate, Mn-silicate, and Mn-oxyhydroxide/Mn-carbonate (Gnoevaya et al., 1982). In addition to the imprecise mineralogy determinations there has been no attempt to investigate in detail the geochemistry (including radiogenic and stable isotopes) of the Mn-ore bed in order to shed light on the fluid and metal sources. Therefore, the suggested genetic models for this deposit (Vassilev et al., 1958; Aleksiev and Nacheva, 1966; Vangelova et al., 2005) based on geological, mineralogical, and geochemical (major elements) considerations were mostly speculative.

The size of the deposit at Obrochishte (largest in Europe), and its similarity to the group of deposits of the same age around the Black Sea, makes it an ideal site to investigate the genesis of the sedimentary Mn ores. Detailed trace element and isotope investigation can provide information about why so much Mn was deposited over such a short period of time around Black Sea? The answer must lie in the geochemistry of the basin seawater at this time and place. In this work, we provide a comprehensive set of geochemical and isotopic (C, O, Fe, Sr, Nd, and Pb) data for samples from the Obrochishte deposit and its host rocks, in order to decipher the processes that lead to the formation of the largest European Mn mineralization.

2. Geological setting

Mn mineralization in NE Bulgaria and the adjacent Black Sea shelf is located within the Ruslar Formation (Tenchov, 1993), which is a part of the Oligocene Series (Lower and Upper) (Fig. 1A, B). Thickness of this Formation varies from a few tens of meters up to ~900 m (based on drill core data). At the majority of the studied sites, it overlies both the Avren and Aladan Formations (Tenchov, 1993) (Fig. 1B, lithostratigraphic core logs). The lower boundary of the Ruslar Formation marks a hiatus stratigraphically interpreted to have varying time span: from Late Cretaceous to Late Eocene. When the hiatus in sedimentation had been long (Fig. 1B, uppermost lithostratigraphic core log) the lower boundary of the Formation is sharp. In the southern part of the region the hiatus had likely been short (Fig. 1B, middle and lowermost lithostratigraphic core logs) and the lower boundary of the Formation is gradational and unclear. The Ruslar Formation is overlain by different stratigraphic units (with hiatus) of the Neogene System (Fig. 1B, lithostratigraphic core logs).

Biostratigraphically, the Mn horizon was deposited in the Early Oligocene during the Pshekian stage at the transition from Nannoplankton (NP) zone 21 to zone 22 (Sachsenhofer et al., 2009, their Figure 2). At the Eocene-Oligocene boundary, which occurs in the NP zone 21, there was a brief, but extensive regression that created an erosional unconformity. Following this regressive episode, sea-level rapidly recovered and by the beginning of NP22, when Mn deposition began, had returned close to pre-regression level (Mayer et al., 2017, their Figure 2). Throughout the succeeding NP22 zone, sea-level fell, but slowly. Surface water salinity also fell until brackish conditions developed at the beginning of the NP23 zone. This has been referred to as the “Solenovian Event” (e.g., Sachsenhofer et al., 2017).

The Ruslar Formation is composed of clays, sandstones, siltstones, and marls (Aleksiev and Nacheva, 1966). The dominance of clays makes it easily recognizable among the other Formations. The clays are finely laminated, gray to brown, with varying silt component, and non-calcareous. Siltstones are gray-green and often grade into silty clays and silty sandstones. Marls are light-gray to green and show unclear laminations. They form a compact body at the middle of the Ruslar Formation. Thus, the Formation is clearly divided into three units north of Varna: under-marl unit (R1), marl unit (R2), and over-marl unit (R3) (Fig. 1B). South of Varna, the marls are presented as single isolated layers. The Ruslar Formation contains also spongolites, diatomites, and bentonites, which form scattered, single, isolated layers.

Manganese mineralization forms 1 to 4 beds within the lower part of the Ruslar Formation (Gnoevaya et al., 1982). The thickest Mn-ore beds are within the siltstones and sandstones of the under-marl unit (R1) north-east of Varna and within the clays of the lower part of the Formation south of the Kamchia River. The ore bed thickness varies from 2 to 24 m, with 11.3 m within the Obrochishte mine area.

3. Samples and methods of investigation

3.1. Samples

We investigated 27 samples from the Mn-ore bed and 5 samples from the host-rock (both below and above the Mn-ore bed) all located at the basal part of the Ruslar Formation recovered at 11 sampling sites (Fig. 1): 12 samples from 5 drill cores, 12 samples from 5 outcrops, and 8 samples from the Obrochishte mine (Table 1). The eight mine samples were collected across the Mn-ore bed crossed and mined at shaft #1 (~320 m below the surface) of the Obrochishte mine located near the Tzarkva village (Dobrich district, northeast Bulgaria). Drill core and outcrop samples were collected by us. Samples from the Obrochishte mine were provided by the mine geologist Mr. Plamen Neychev following our requirements based on the mine report description of the Mn-ore bed. Pisoliths from 6 mine samples and the matrix among them from one sample were selected by hand picking for further analyses.

3.2. Methods of investigation

Initial characterization of the samples was with a binocular microscope, followed by examination of polished thin sections with an optical polarizing microscope (Eclipse LV100N POL, Nikon; Department of Marine Resources and Energy, Tokyo University of Marine Science and Technology). Subsequent qualitative X-ray fluorescence mapping of the thin sections was performed on a Bruker Tornado μXRF using a Rh source operating at 50 kV and 600 μA under 20 mbar vacuum (Laboratory for Ocean Geosciences, European Institute for Marine Studies). Spot size was 20 μm and dwell times were 6 ms/pixel. Images of the areal distribution of elements along the thin sections were produced using M4 Tornado software package with spectra deconvolution and averaging every 3 pixels. All elements were represented by their K_α emission lines except for Fe, for which K_β emission was chosen for imaging due to significant overlap of the K_α Fe emission signal with the stronger K_α emission of Mn in the samples. Scanning electron microscope (SEM) imaging and energy dispersive X-ray analysis (EDX) using a FEI XL30 ESEM and an associated EDX system were performed in order to investigate mineral morphology and chemistry on a smaller scale.

Bulk samples, separated pisoliths and matrix among the pisoliths were ground to fine powder in an agate mortar and sieved to less than 200 mesh in acid-washed stainless-steel sieves prior to the bulk mineralogy and geochemistry investigations.

Bulk mineralogy was determined by X-ray diffractometry (XRD) on the powdered samples mounted on glass slides by dispersing grains in alcohol. This standard specimen preparation is necessary when working with small amounts of samples. It provides an even coating of powder that adheres to the sample holder and helps alleviate problems with preferred crystal orientation. Instrumentation was a Siemens D500 X-ray diffractometer with Cu K_α radiation (Department of Geology, University of Cincinnati). Scans were conducted from 5° to 55° 2θ with a step size of 0.2° 2θ and a count time of 10 s/step. Quantification of the X-ray diffraction patterns was done by Rietveld refinement using the software Panalytical HighScore Plus and the reference patterns stored in the ICSD 2013 database distributed by FIZ Karlsruhe.

Bulk chemistry of the samples was determined by X-ray fluorescence (XRF) using a Rigaku 3070 spectrometer (Department of Geology, University of Cincinnati). Sample powders were pressed into thin pellets using a Spex 3624B X-Press 20-ton press. Samples were analyzed for major and selected trace elements. Concentrations of major elements were calculated by multiple regression using data from a set of USGS and NIST standards selected to bracket the range of compositions in the samples. Trace elements were calibrated by simple regression after correcting for peak overlaps (e.g., Sr K_β on Zr K_α).

A set of powdered sub-samples (~50 mg each; bulk and pisoliths) were dissolved with HF-HCl-HNO_3 in clean Teflon vials for whole-rock elemental concentration and radiogenic isotopes measurements (Department of Geological Sciences, University of Florida). According to the previous studies (Vassilev et al., 1958), the Mn-ore bed is composed of both ore (Mn- carbonates and oxyhydroxides) and detrital components. Therefore, we decided to investigate the chemical composition of both components. For this reason, we prepared another set of powdered sub-samples (bulk and pisoliths) for two-step dissolution. About 80 mg of sample powder was dissolved with 2*M* HCl for 2 hours on a hot (100°C) plate aiming at leaching of the ore component (Mn-carbonates and -oxyhydroxides) only. The resultant leachates were separated from the residues in clean Teflon vials and evaporated to dryness. The remaining residues (supposed to be detrital component) were further dissolved with HF-HNO_3. Chemical compositions of produced solutions (bulk samples, leachates, and residues) were analyzed with Inductively Coupled Plasma Mass Spectrometry (ICP-MS) using Thermo-Finnigan Element 2 instrument, and Re and Rh as internal standards. Quantification of the results was done by external calibration using a combination of USGS rock standards (AGV-1, BCR-2, and BIR-1) and following methods described in Kamenov et al. (2008). The error for the trace elements was less than 5%.

Strontium, Nd and Pb isotopes were separated from bulk and pisolith samples (bulk, leachate, and residue) using standard ion-exchange procedures and measured on a Nu Plasma Multiple Collector Inductively Coupled Plasma Mass Spectrometer (MC-ICP-MS) following methods described in Kamenov et al. (2008). The reported $^{87}Sr/^{86}Sr$ ratios are relative to NBS 987 $^{87}Sr/^{86}Sr$=0.71025 (+/-0.00003, 2σ). The Nd isotopic compositions are relative to JNdi-1 $^{143}Nd/^{144}Nd$=0.512115 (+/-0.000018, 2σ). The Pb isotope data are relative to the following values of NBS 981: $^{206}Pb/^{204}Pb$=16.937 (+/-0.004, 2σ), $^{207}Pb/^{204}Pb$=15.490 (+/-0.003, 2σ), and $^{208}Pb/^{204}Pb$=36.695 (+/-0.009, 2σ).

For C and O isotope analyses, bulk (carbonate) samples, separated pisoliths and standards were reacted in He purged exetainer vials (10 min at 110 mL/min He flow) with 100% phosphoric acid in a water bath at 25ºC. The C and O isotopic composition of the CO_2 headspace gas was analyzed on a Thermo Delta V Advantage isotope ratio mass spectrometer with a Thermo Gasbench II connected via a Conflo IV interface (Department of Geology, University of Cincinnati). The $\delta^{13}C$ values of carbonates were normalized to the VPDB scale using LSVEC (-46.6‰) and NBS-19 (1.95‰). The $\delta^{18}O$ values were normalized to the VPDB scale with NBS-18 (-23.01‰) and NBS-19 (-2.2‰) following the recommendation of Kim et al. (2015). The O isotope acid fractionation factors that were used for calcite and rhodochrosite were 1.01030 (Kim et al., 2007) and 1.01012 (Friedman and O'Neil, 1977; amended from Sharma and Clayton, 1965), respectively. Precision and accuracy were determined by analyzing an independent calcite standard over the course of analyses (n=43). For $\delta^{13}C$, precision and accuracy were 0.11‰ (1σ) and 0.00‰, respectively. For $\delta^{18}O$, precision and accuracy were 0.09‰ (1σ) and 0.01‰.

Stable Fe isotopes were studied in 20 samples according to the analytical protocol reported in Rouxel et al. (2008) at Pôle de Spectrométrie Océan, IUEM/Ifremer. About 50 mg of each powdered sample and georeference materials [BHVO-2 (Hawaiian basalt), Nod-A-1 (Atlantic Mn-nodule), and Nod-P-1 (Pacific Mn-nodule)] were put in 15 mL PFA beakers. Powders were dissolved in 2 mL concentrated (14.4*M*) ultrapure HNO_3 (obtained using TFE sub-boiling distillation system, hereafter referred as SB grade) and between 1 to 2 mL of concentrated Trace Metal™ (Fisher Scientific) grade HF. Solutions were evaporated to dryness on a hot plate at 80°C. Then, we added 2 mL concentrated SB grade HNO_3 and 2 mL 6*M* SB grade HCl (thus forming *aqua regia*). Solutions were evaporated to dryness on a hot plate at 90°C. After that, we added 1 mL 5*M* HCl with 10 µL of 30% (v/v) H_2O_2 in each beaker, closed the beakers and put them on a warm (60°C) plate for 1 h. The beakers were cooled down (20°C) and the solutions were ready for column load.

For Fe isotope separation we used 2.0 mL (wet volume) of anion-exchange resin AG MP-1 placed in polypropylene columns. All diluted acids were prepared from SB-grade concentrated acids. Before the sample load, the resin was washed with 10 mL 3*M* HNO_3, 10 mL 18 MΩ cm^{-1} H_2O, 5 mL 1.2*M* HCl, and conditioned with 2 mL 5*M* HCl. 1 mL of each sample solution was loaded in the columns. The matrix fraction was eluted with 14.5 mL 5*M* HCl. Fe was eluted with 14 mL 1.2*M* HCl in PFA beakers. After evaporation of the Fe eluate at 90°C, we added 2 mL 0.28*M* HNO_3 in the beakers and transferred the solutions into 2 mL PFA vials.

Fe isotope compositions were determined with a Neptune (Thermo-Scientific) MC-ICP-MS using medium or high-resolution mode. It involves both "sample-standard bracketing" and "internal normalization" using Ni of known isotope composition (Weyer and Schwieters, 2003; Poitrasson and Freydier, 2005; Rouxel et al., 2005). All analyses are reported in delta notation relative to the IRMM-014 standard, expressed as $\delta^{56}Fe$. Based on >50 replicate dissolutions, purifications, and analyses of internal standard BHVO-2, we have obtained: $\delta^{56}Fe = 0.09 \pm 0.07‰$ (2 SD). Results for Mn-nodules Nod-A-1 and Nod-P-1 yielded $\delta^{56}Fe = -0.39 \pm 0.06‰$ (2 SD) and $-0.51 \pm 0.06‰$ (2 SD), respectively, which is indistinguishable, within analytical error, from previously published values (Asael et al., 2013; Marcus et al., 2015; Rolison et al., 2018).

4. Results

4.1. Petrography

Most samples collected from the Mn-ore layer at the mine were highly pisolitic (Fig. 2) comprising tan to brownish-red, concentrically-laminated pisoliths (Fig. 3A, B) set in a greenish-tan matrix. Pisoliths are 1 to 2 cm in diameter and show some tendency to increase up-layer in both size and abundance. Thin section microscope observations revealed that the grain size for both the carbonate and the aluminosilicate components was exceeding small and the ore matrix looked greyish-brown to light-brown (images not shown). Optical microscopy observations along with X-ray fluorescence mapping showed that the pisolith concentric layers were of two types: carbonate-rich and aluminosilicate-rich (Figs 3C, D; 4). Carbonate-rich layers were composed of Mn- and Mn-Ca-carbonates (Fig. 4A, B, C). They alternated with layers enriched in elements typical for detrital aluminosilicate component: Al, Si, Fe, Rb, and Zr (Fig. 4D, E, F, G, H). The SEM imaging showed that the carbonate-rich layers contained large crystals of Mn-carbonate (Fig. 5A), whereas the aluminosilicate-rich layers were composed of sub-micron spheres of silica and Mn-carbonate (Fig. 5B), and, possibly, clays.

An EDX survey of the composition of pisoliths and matrix showed (Table 2) the same distribution as in the X-ray mapping: the matrix was primarily Al- and Si-rich, whereas the pisoliths were composed predominantly of Mn and Ca.

4.2. Mineralogy

The strata below and above the Mn-ore layer are composed mainly of quartz, plagioclase, and clay minerals (illite/smectite and kaolinite). Where carbonates are present, they are calcite or dolomite rather than one of the Mn-carbonates (Table 1).

The Mn-ore layer and its low-grade equivalents also include the same detrital components. They differ from the host strata in having Mn-carbonates as well. The amount and type of Mn-carbonates varies laterally. In the area of the Obrochishte mine, the Mn-ore layer is mainly composed of rhodochrosite ($MnCO_3$) with some kutnahorite [Ca (Mn^{2+}, Mg^{2+}, Fe^{2+}) $(CO_3)_2$] at the base and lesser amounts of detrital components (Table 1). This assemblage is consistent with the results of Vassilev et al. (1958). However, northeast of the Obrochishte mine where the ore-equivalent horizon is crossed by drill holes, kutnahorite dominates over rhodochrosite and non-ore components roughly equal ore minerals. To the south and southwest of the Obrochishte mine where the ore interval crops out (Fig. 1), it is mostly composed of quartz, plagioclase, and clays with subordinate amounts of Mn-calcite [(Ca, Mn) CO_3] and kutnahorite (Table 1). Our samples are mostly free of Mn-oxides. Trace amounts of pyrolusite (MnO_2) and todorokite [$(Na, Ca, K)_2(Mn^{4+}, Mn^{3+})_6O_{12}$•3-4.5($H_2O$)] were found in some samples (OBR-7-3178, OBR-7-4130, OBR-8-A, OBR-9-3884) at amounts too low to be quantified by the Rietveld refinement (therefore, not in Table 1). Rare thin (0.1-0.5 mm) pyrite veins cross the ore matrix (Figs 3E, F, G; 6). They have thin rhodochrosite bands (Fig. 3E) and are altered along thin cracks at some places (Fig. 3H).

4.3. Geochemistry

Similar to the distribution of minerals, the host strata below and above the Mn-ore layer lack significant Mn content (MnO=0.04-0.46 wt.%; Table 3). Content of the most other elements in bulk rock samples are similar in the ore layer and in the host strata except for Ca, Fe, Pb, and Zn, which are higher in the host rocks, and Mn, Co, Mo, Ni, V, P and total rare earth elements (REE), which are substantially higher in the ore interval. The ore interval shows considerable lateral variation in geochemistry. In the Obrochishte mine area, the Mn-ore layer contains less SiO_2, Al_2O_3, Fe_2O_3, K_2O, and $S_{tot.}$, and more MnO, MgO, and $C_{tot.}$ than both the host rocks and the Mn-ore interval sampled at the outcrops and drill holes outside the mine area (Table 3). Across the Mn-ore layer CaO and Fe_2O_3 concentrations decrease upward (Table 3). Overall, the picture from mineralogy and bulk geochemistry is that the sedimentary rocks are a mixture of a detrital component of fixed composition and a (presumably) authigenic component that varies from Ca-rich to Mn-rich.

Within the authigenic component, there are important variations that likely relate to depositional conditions. The relationship between organic carbon (C_{org}) and total sulfur (S_{tot}) content is often used to characterize low-oxygen environments (e.g., Potter et al., 2005). Organic carbon concentrations in the studied samples are low, ranging from 0.1 to 1.3 wt.% with an average of 0.4 wt.% (Table 3). Total sulfur content ranges to higher values, with some exceeding 2 wt.% (Table 3). Many of the studied samples show the typical correlation between C_{org} and S_{tot} that is found in normal marine sediments (Fig. 7) (Berner, 1982; Raiswell and Berner, 1986; Morse and Berner, 1995). There is another group of samples, however, that has excess S, which is usually interpreted to indicate free H_2S in the water column (euxinic conditions). There is a tendency for the S_{tot} concentration in these rich in S samples to increase upwards across the Mn-ore layer, but there are exceptions.

Because the ore consists of a mixture of detrital components and authigenic material in two contrasting textural forms (matrix and pisoliths), it is useful to view the geochemistry of major and trace elements in terms of separate fractions. The concentrations of trace elements and some major elements in the bulk, pisolith, leachate and residue fractions of the samples are reported in Table 4.

The chemistry of the studied sample fractions (leachates and residues) shows some interesting features (Table 4). The major part (>50%) of the investigated elements (Mg, Fe, Mn, Na, K, Li, Sc, Ti, V, Cr, Co, Zn, Ga, Rb, Zr, Nb, Cs, Ba, Hf, Ta, and Th) in the host rock (sample OBR-8-A) are in the residual fraction (Table 4). Only P, Ni, Cu, Y, Pb, and U reside mostly (>50%) in the leachate fraction of the host rock. REE and Sr are equally distributed in both fractions.

The residues of the Mn-ore layer (sampled in the mine and in a drill hole) and pisoliths (Table 4) contain the major part of K, Sc, Ti, Cr, Ga, Rb, Zr, Nb, Cs, Hf, and Ta. The leachate fraction of this layer and of the pisoliths contains most (>50%) of Ca, Mg, Mn, Na, P, Li, V, Co, Ni, Zn, Sr, Y, Ba, REE, Pb, Th, and U. Cu is almost in equal proportions in both fractions.

The vertical distribution of some elements across the Mn-ore layer sampled at the mine show some correlation with the ore mineralogy. Major ore mineral in the lowermost two samples is kutnahorite whereas rhodochrosite is the only ore mineral in the rest of the samples upward (see sub-section *4.2* and Table 1). Li and V are mostly in the residue in the lowermost two kutnahorite-containing samples and in the leachate in the upper rhodochrosite samples. Fe and Pb are mostly in the leachate fraction of the pisoliths in the lower kutnahorite-containing samples and progressively decrease upward through the rhodochrosite samples. Na is mostly in the leachate of the pisoliths, but lower in the lowermost two kutnahorite-containing samples. Cu is mostly in the leachate of pisoliths in the lower two kutnahorite samples and mostly in the residue in the upper rhodochrosite samples.

In order to estimate the magnitude of elemental enrichment of the Mn-ore layer with respect to the host rocks we compared the averages of the leachate compositions of the bulk samples from the Obrochishte mine (samples OBR-11: Mn-ore layer), one drill hole (samples OBR-5: Mn-ore layer), and a host rock sample (OBR-8-A), and of the pisoliths from the Mn-ore layer at the Obrochishte mine (samples OBR-11-1.2P, -1.8P, -3.8P, -4.4P, -5.1P, -6.1P). This sample selection is based on the assumption that the residues of all studied samples represent detrital component delivered to the sedimentary basin from the same provenance and with similar composition.

Ca concentration in the leachates of the host rocks (~20%) is 3-5 times higher than that of the leachates of the Mn-ore layer and its pisoliths (Table 4). In contrast, Mn, Mg, and Fe concentrations in the leachates of both the Mn-ore layer and its pisoliths are higher than those of the host rocks. Mn and Mg contents are even 2-3 and 1-2 (respectively) orders of magnitude higher than those of the host rock. Only K, Ti, Cu, Nb, Hf, Ta, and Pb have similar concentrations in the leachates of both types of samples: Mn-ore layer (and its pisoliths) and host rock. Contents of all the other studied elements (V, Co, Ba, Na, Li, Ni, REE, Th, Zn, Ga, Cr, Rb, Sr, Y, Zr, Cs, and U) are higher in the leachates of the Mn-ore layer (and pisoliths) than in those of the host rock. The concentrations of Na, Li, Ni, REE, and Th are 1 and those of V, Co, and Ba are 1-2 orders of magnitude higher than those of the host rock. Pisoliths are richer in P, Y, heavy REE (Ho-Lu), and U than the Mn-ore layer (bulk) and host rock, but poorer in Th than the Mn-ore layer (Table 4). They are richer in Mn, Ca, and (particularly) P than the matrix among them (Table 3).

The total content of REE (ΣREE) in the studied Mn-ore samples (Table 4) is slightly lower than that of the average upper continental crust (UCC) (McLennan, 1989). ΣREE in the background samples (below and above the Mn-ore bed) are even less than the ΣREE of the Mn ores (Table 4, sample OBR-8-A). Over 60% of the content of each rare earth element in the studied Mn ore samples is within the leachable by 2*M* HCl fraction and only <40% of the REE content is in the residue supposed to be composed of detrital alumino-silicates (Table 4; Fig. 8A, B). Selected pisoliths show similar REE composition with over 70% of the REE content being within the leachable fraction (Table 4; Fig. 8C). The REE distribution patterns of the Mn ores and their components (Fig. 8A-D; Table 4) are broadly similar to those of the upper continental crust (Fig. 8F; McLennan, 1989) with light REE (LREE) enrichment, flat heavy REE (HREE) distributions and negative Eu anomaly (Eu/Eu*<1). The only difference between them and those of the upper continental crust is the negative Ce anomaly (Ce/Ce*<1) (Fig. 8A-D; Table 4). The negative Ce anomaly is well pronounced at the REE distribution patterns of both the bulk samples ($Ce/Ce^*_{average}$=0.69) and the 2*M* HCl leachates ($Ce/Ce^*_{average}$=0.79), whereas it is negligible at the REE distribution patterns of the residues ($Ce/Ce^*_{average}$=0.90) (Fig. 8A-D; Table 4). REE distribution patterns of the leachates of both the Mn ores and background rocks are similar with the only difference that the REE contents in the Mn ores are about five times more than those in the background rocks (Fig. 8A, B, F).

4.4. Isotope geochemistry

4.4.1. C and O isotopes

C and O stable isotope values of studied samples (Table 5), when plotted against one another, fall into two groups (Fig. 9A). One has $\delta^{18}O_{PDB}$ of 0‰ to -4‰, and $\delta^{18}O_{PDB}$ is independent of $\delta^{13}C_{PDB}$ (Fig. 9A). The other group has a strong correlation of $\delta^{18}O_{PDB}$ to $\delta^{13}C_{PDB}$, with lighter O isotope values, ranging from -12‰ to -3‰. This second group comes from sample sites (##6, 7, 8, and 9) located in the southern part of the Ruslar Formation with larger content of detrital component (clays and sandstones) (Fig. 1B). They plot along an array between typical fresh water and seawater. Although mineralized, this sample group has lower MnO content: ≤10%. These samples are strongly enriched in Cu, Pb, and Zn (3 to 8 times in bulk composition) compared to the fully marine group, which in turn is strongly enriched in Cl, S, and V with lesser enrichment in Co and Ni. The number of leachate samples for the first sample set was too small to make valid comparisons.

Another aspect of C-O isotope geochemistry is seen in a plot of $\delta^{13}C_{PDB}$ against Mn content of the studied samples (Fig. 9B). This pair of variables also shows two distinct trends, but involving a somewhat different grouping of samples from the $\delta^{18}O_{PDB}$ - $\delta^{13}C_{PDB}$ plot (Fig. 9A). One set of samples (Group I) clusters around the value for seawater bicarbonate ($\delta^{13}C_{PDB}$ = 0‰) and is independent of Mn concentration. This set of samples is substantially larger than the other set and comes from stratigraphically lower positions in the Mn-ore layer in the mine area. The other sample set (Group II) has lighter C isotope values, -5‰ to -25‰, and they correlate inversely to the MnO concentration (Fig. 9B). The first array has $\delta^{13}C_{PDB}$ values consistent with derivation from seawater HCO_3^-, whereas the second array has some to all of its C derived from decay of organic matter, perhaps including some oxidized methane for samples with $\delta^{13}C$ in the -25 to -32‰ range. The lightest $\delta^{13}C_{PDB}$ value, -25‰, corresponds to modern C isotope values for organic matter in sediments on the shelf off the mouth of the Danube River, -26‰ to -23‰ (Galimov et al., 2002), so the second array spans the complete range from 100% organic-sourced C to 100% seawater-sourced carbon. The bulk chemistry of the two populations identified on Figure 9B shows enrichments in Group I in Pb and Zn when compared to Group II, which in turn shows strong enrichments in Co, Ni, and S and smaller enrichments in V, Cr, and Cu. For the leachates, a smaller sample set, the Co and Ni enrichments seen in the bulk chemistry do not appear, but V and Cu remain higher in Group II samples compared to Group I. Pb continues to be enriched in Group I, but Zn does not show enrichment.

4.4.2. Sr, Nd and Pb isotopes

$^{87}Sr/^{86}Sr$ in the bulk samples shows a range from 0.70826 to 0.70937 (Table 5). The leachates show lower values compared to the bulk samples and cluster around the expected seawater Sr isotopic composition at 31 My (Fig. 10). A t-test shows that the means of the two sets of data are statistically different (P = 0.001). The residues show much more radiogenic $^{87}Sr/^{86}Sr$ when compared to leachates and bulk, with values ranging from 0.70967 to 0.72038 (Table 5). Sample size for the residues is too small for effective statistical evaluation.

Bulk samples show a relatively narrow range for εNd, between -6.7 and -8.1 (Table 5). Leachates also show a narrow range for εNd, between -6.0 and -7.4. Again, the means are significantly different (P = 0.009). A portion of the leachates overlap with the expected Nd isotopic composition for Atlantic and Tethys seawater at 31My, although some leachates and most of bulk samples extend to more negative εNd, towards the residues (Fig. 11). As can be seen from Figure 11, the residues show the most negative εNd as low as -12.1, from all of the analyzed samples (Table 5).

In contrast to Sr and Nd isotopes, Pb isotopes have very similar median values for bulk and leachate compositions and show the same modes on histograms. Statistically, the means for bulk and leachate sample sets are the same for $^{206}Pb/^{204}Pb$ (P = 0.33) and for $^{207}Pb/^{204}Pb$ (P = 0.83), whereas the means for $^{208}Pb/^{204}Pb$ are somewhat different (P = 0.02). The residence time of Pb in seawater (unlike that of Sr and Nd) is very short (30-400 years) and Pb reflects local weathering inputs (e.g., Basak and Martin, 2013). Thus, the dissolved and particulate Pb fractions should have similar isotope composition. Means for the three isotope ratios are: $^{206}Pb/^{204}Pb$ of bulk samples, 18.95 and leachate samples, 18.89; $^{207}Pb/^{204}Pb$ – 15.661 and 15.663, respectively; $^{208}Pb/^{204}Pb$ – 38.80 and 38.70, respectively. Sample OBR-8-A departs significantly from others in Pb isotope values, but it is mostly composed of $CaCO_3$ rather than of $MnCO_3$. Therefore, we have excluded it from the statistical analysis. We only have Pb isotopic data from 4 residues, so statistical comparisons are difficult. However, the similarity of the whole-rock and leachate values implies that the residues should also be similar. Also, the means for the residue isotopes are within 1% of the means for the leachates and whole rock.

4.4.3. Fe isotopes

Iron isotope composition ($\delta^{56/54}Fe$) of the whole-rock samples from the Mn-ore layer at the Obrochishte mine ranges from -0.16‰ to +0.16‰ (samples OBR-11-…; Table 5) and does not clearly correlate to other geochemical parameters such as concentrations of Al_2O_3 and MnO (Tables 3, 4). In the areas lateral to the mine, the whole-rock $\delta^{56/54}Fe$ range is greater: -0.33‰ to +0.24‰. The pisolith $\delta^{56/54}Fe$ (analyzed at the Obrochishte mine only) has a distinct trend to lighter values relative to the host whole-rock data and decreases upward within the Mn-ore layer (Table 5). The lower Mn-ore beds (samples OBR-11-1.2 to OBR-11-3.8) have average $\delta^{56/54}Fe_{pisolith}$ = -0.08‰ (Table 5), whereas the upper Mn-ore beds (samples OBR-11-4.4 to OBR-11-6.1) have average $\delta^{56/54}Fe_{pisolith}$ = -0.36‰.

5. Discussion

5.1. Mineralogy of Mn-ore layer

The absence of Mn-minerals in the host strata below and above the Mn-ore layer (Table 1) suggests that precipitation was caused by an abrupt change in geochemical conditions. Maynard et al. (1990) observed a similar abrupt appearance of Mn in the Molango deposit of Mexico and related it to a rise in sea-level that allowed penetration of new water into the depositional basin.

For Obrochishte deposit, the occurrence of Mn-oxides mostly in the outcrop samples is in accordance with the previous suggestion (Vassilev et al., 1958) that these are secondary minerals formed as a weathering product of the primary Mn-carbonates. The Mn-ore layer crossed at the Obrochishte mine is richer in Mn-minerals (rhodochrosite and kutnahorite) than at the other studied sites (Table 1). We interpret this lateral variability in the mineralogical composition of the Mn-ore layer as a result of different degree of dilution of the Mn-minerals with detrital component (quartz, plagioclase, and clays). The area of the Mn deposit is relatively small (Fig. 1) and it does not seem plausible to assume that the lateral variability in the mineralogy of the Mn-ore layer is due to spatial variations in the conditions of Mn-mineral precipitation.

5.2. REE constraints on redox conditions of Mn-carbonate precipitation

The close resemblance of the REE distribution patterns of the Mn-ore residues (after 2*M* HCl leaching) (Fig. 8A-D; Table 4) to those of the average UCC (Fig. 8F) suggests that the residues are detrital (terrigenous) component. The negative Ce anomaly in the REE distribution patterns of the 2*M* HCl leachable component of the Mn-ores is visible at the REE distribution patterns of the bulk Mn-ore (Fig. 8A, B) as the latter is the sum of both leachable and residual (without Ce anomaly) components. The 2*M* HCl leachable component is mostly composed of authigenic Mn-carbonates and therefore, it is essential to understand the source of this anomaly and its implications for the source of Mn in the ore layer.

The location of the Mn-ore layer within a sedimentary rock sequence (Oligocene Ruslar Formation) suggests that it is a sedimentary formation (e.g., Johnson et al., 2016). Therefore, any aspect of its deposition needs to consider the conditions in the depositional basin. The Ruslar

Formation in general, had formed at the western margin of the Western Black Sea basin, which was progressively opening during the Oligocene (Nikishin et al., 2015). According to the paleotectonic reconstructions (Nikishin et al., 2015) during this epoch, the uplift of the Pontides orogenic area limited the open oceanic connection of the basin with the Tethys. This reduced the ventilation of the Western Black Sea, which in turn led to suboxic to anoxic conditions in the water column (Sachsenhofer et al., 2009; Mayer et al., 2017). Therefore, when discussing the geochemistry of the Mn deposit formed at the western margin of the Oligocene Black Sea, it seems reasonable to use as a proxy the recent anoxic Black Sea (see also Schulz et al., 2005).

The modern Black Sea water body is vertically stratified in three layers (from surface to bottom): oxic, suboxic and anoxic (Lewis and Landing, 1991; German et al., 1991; Schijf et al., 1991). The suboxic layer is the zone where sharp gradients of dissolved as well as particulate elements (Mn, Fe, and REE) are found (German et al., 1991; Schijf et al., 1991). Its thickness varies from a few meters up to as much as 80 m with an average of ~26 m (Glazer at al., 2006a, b). Particulate Mn concentration is high throughout the suboxic layer, but its maximum occurs at the top of this layer coincident with a minimum in dissolved total REE and a minimum in Ce/Ce* (German et al., 1991). The maximum of particulate Fe content is shifted down, at the transition from the suboxic to the anoxic layer. Average Ce/Ce* (chondrite-normalized) of dissolved REE is 0.39 in the oxic layer, 0.08 at the oxic-suboxic transition, 0.34 in the suboxic layer proper and 0.86 in the anoxic layer (calculated from the data reported by German et al., 1991). We have not found any data for the REE composition of the corresponding particulate material. A rough estimate can be calculated by assuming the observed dissolved values are the residual after extraction of dissolved REE by adsorption to newly-formed Mn-oxide particles. The very low Ce/Ce* value at the oxic-suboxic boundary requires a positive particulate Ce anomaly of about 1.80, based on the difference between the dissolved values of La Ce, and Nd in the oxic and transition layers. Using the same approach, the suboxic layer itself would produce particles with Ce/Ce* of about 0.84 (see online data supplement for details). These numbers are sensitive to the exact choice of samples to be included in each category, but they do give an indication of what is to be expected for different levels in the water column.

The Ce/Ce* of the Mn-ore leachates (Fig. 8A-D) ranges from 0.61 to 1.03 with an average of 0.77 with no apparent trend across the Mn-ore layer. For comparison, two other circum-Black Sea deposits have reported REE data: Binkiliç, which averages 0.80 for Ce/Ce* and Nikopol, which has 1.05 in oxide ore and 0.91 in carbonate ore [calculated from data of Gültekin and Balci (2018) and Varentsov et al. (1997), respectively]. Thus, the REE in the Mn-ores around the Oligocene paleo-Black Sea could reasonably have been acquired by scavenging of the dissolved REE ions by particulate Mn-oxides, which then sank to the seafloor and were converted to $MnCO_3$ during diagenesis. The values seen suggest formation in the lower part of the suboxic zone. The Ce/Ce* values are also consistent with a portion of the REE being directly incorporated in $MnCO_3$ in the seawater column (see model of Konovalov et al., 2006). The carbonate phase would not have a preference for Ce^{4+} so its REE distribution pattern would be the same as that of the seawater parcel where precipitation occurred. The amount of this authigenic $MnCO_3$ is hard to estimate because of the uncertainty in the value for the Mn-oxides, but 20 to 30% could easily be accommodated (see calculations in online data supplement). In summary, Ce/Ce* for the Obrochishte Mn-ore layer is consistent with precipitation of Mn as Mn^{4+}-oxide in the suboxic layer of the seawater column in a euxinic basin similar to the modern Black Sea, with some Mn going directly into $MnCO_3$ as Mn^{2+} at the top of the anoxic zone.

5.3. Controls on the trace element content of the Mn-ore layer

5.3.1. Crystallography and mineralogy controls on the Sr and Ba concentrations in Mn-ore layer

The lowermost part of the Mn-ore layer crossed at the Obrochishte mine (OBR-11-1.2 and OBR-11-1.8) is richer in Sr and Ba than the middle-upper part of this layer sampled in the Obrochishte mine (Table 4). The mineralogy studies did not reveal any single mineral phases of Sr and Ba in any sample. Hence, Sr and Ba are either hosted in the crystal lattice of some minerals, or they are adsorbed on the mineral surfaces. Chemistry of the acid-leached fraction (presumably composed mainly of Mn-carbonates) and residual fraction (presumably composed mainly of aluminosilicates) showed that Sr and Ba were mostly (>70%) hold in the Mn-carbonates (excluding Ba in the lower part of the Mn-ore layer drilled at site #5) (Table 4). We have not performed detailed partitioning chemistry analysis that would allow us to precisely determine the carbonate-bound and adsorbed fractions of these two elements. Therefore, we may consider (at first approximation) that a major part of the elements leached according to our protocol (see *3.2*) are carbonate-bound. Thus, the vertical distribution of Sr and Ba across the Mn-ore layer in the mine (site #11) seems to be crystallographically controlled.

The lowermost Mn-ore layer contains kutnahorite as a major ore mineral along with rhodochrosite, whereas the middle-upper Mn-ore layer contains only rhodochrosite (Table 1). The only possible structural site for Sr^{2+} and Ba^{2+} substitution in rhodochrosite ($MnCO_3$) is that of Mn^{2+} in octahedral coordination, whereas the structural sites for Sr^{2+} and Ba^{2+} substitution in kutnahorite [$Ca(Mn, Mg, Fe)(CO_3)_2$] are those of Ca^{2+}, Mg^{2+} and Fe^{2+} in addition to that of Mn^{2+}. According to the Goldschmidt's rules of substitution of ions in crystals (Goldschmidt, 1954) from charge considerations Sr^{2+} and Ba^{2+} might substitute for Mn^{2+}, Ca^{2+}, Mg^{2+} and Fe^{2+} in the crystal lattices of both carbonates. Then, the governing control for such a substitution is the ionic radius of the replacing and replaced ions. For an extensive substitution, the radius of the replacing ion must not differ from the radius of the replaced ion by more than 15% (Goldschmidt, 1954). The ionic radius of Mn^{2+} in six-fold coordination (like that in rhodochrosite) is 0.75-0.91 Å (depending on the low or high spin, respectively), whereas the radii of Sr^{2+} and Ba^{2+} in the same coordination are 1.21 and 1.44 Å, respectively (Whittaker and Muntus, 1970). Hence, Sr^{2+} and Ba^{2+} substitution for Mn^{2+} in rhodochrosite crystal lattice is difficult: r_{Sr} and r_{Ba} must be ≤1.05 Å (i.e., 115% of the Mn^{2+}-site radius) for an extensive substitution. However, the theoretical possibilities of Sr^{2+} and Ba^{2+} incorporation in the kutnahorite crystal lattice are different. In addition to the structural site of Mn^{2+}, which obviously cannot easily accommodate these elements, there are also those of Ca^{2+}, Mg^{2+} and Fe^{2+}. The ionic radii of Mg^{2+} and Fe^{2+} in six-fold coordination are even smaller than that of Mn^{2+} (0.80 and 0.86 Å, respectively), which means that their structural sites cannot easily accommodate Sr^{2+} or Ba^{2+}. However, the structural site of Ca^{2+} (r_{Ca} = 1.08 Å; Whittaker and Muntus, 1970) can easily accept substitution of ions up to 1.24 Å (within the 15% substitution tolerance), which is perfect for Sr^{2+} accommodation (r_{Sr} = 1.21 Å), but more difficult for Ba^{2+} accommodation (r_{Ba} = 1.44 Å). This explains the higher concentrations of Sr in the lowermost Mn-ore layer containing kutnahorite than in the middle-upper Mn-ore layer having only rhodochrosite. Barium may instead reside in small amounts (<4%, the detection limits of XRD) of single Ba-mineral like barite that has not been detected during our XRD investigations. The lowermost Mn-ore layer contains on average 190 ppm Ba, whereas the middle-upper Mn-ore layer (samples OBR-11-4.4 to -6.1) has on average 160 ppm Ba (Table 4). Its enrichment in the lower Mn-ore layer may reflect a more oxidizing depositional environment, which is supported by the presence of excess S (i.e., S in excess of that predicted from the C_{org} content) in the middle-upper Mn-ore layer: $S_{excess\ lower}$ = 100 ppm, $S_{excess\ upper}$ = 1300 ppm (Table 3).

5.3.2. Euxinia control on Fe, Zn, Cu, Cr, Ni, Co, and Mo contents of Mn-ore layer

Principal minerals in the Mn-ore layer are rhodochrosite and kutnahorite (Table 1). Reasonably, major part of Mn, Ca, and Mg in this layer (and in the extracted pisoliths) is in the leachate fraction (Table 4), i.e., mostly in the Mn-carbonates. In addition to these major elements, a number of trace elements (Na, P, Li, V, Co, Ni, Zn, Sr, Y, Ba, REE, Pb, Th, and U) is also mostly contained in the leachate fraction of the Mn-ore layer (Table 4). The enrichment of the Mn-ore layer in these trace elements relative to the host rocks is likely a result of the processes that led to the deposition of this layer in the Western Black Sea during the Early Oligocene.

Major accumulations of sedimentary Mn are thought to require the presence of a large body of anoxic seawater to provide a sufficient reservoir of dissolved Mn (e.g., Maynard, 2014). The required anoxia can develop in two ways: a restricted marine basin, or an intense oxygen-minimum zone in the open ocean (Maynard, 2010). In the former case, the basin becomes euxinic: i.e., there is free H_2S dissolved in the bottom water. In both cases, the Mn deposit forms above the anoxic water where suboxic conditions impinge on the seafloor.

Consistent with this model, REE evidence from studied deposit suggests that the Mn-ore layer formed in suboxic seawater conditions (see *5.2*). Euxinic conditions offshore from the area of deposition are indicated by several studies of the petroleum potential of the Ruslar Formation (e.g., Sachsenhofer et al., 2009; Mayer et al., 2017). We also see some evidence for euxinic conditions at the area of Mn deposition, based on the excess S found in some of the samples (Fig. 7). It would appear that seawater in the deeper Early Oligocene Western Black Sea basin was anoxic, while on the shallow shelf it was generally suboxic (see Mayer et al., 2017, their Figures

11 and 12), but with occasional intervals when the chemocline rose to cover the shallow shelf. Deposition of several Mn-carbonate layers (up to 4; Gnoevaya et al., 1982) during Early Oligocene suggests for intermittent euxinic conditions, like those in the modern Baltic Sea deeps (Lenz et al., 2015).

This model is also supported by the Mo content of the Mn-ore layer (Table 3). Molybdenum concentrations of this layer are generally below 10 ppm (except for sample OBR-5-1262; Table 3). Studies on modern euxinic basins (Scott and Lyons, 2012) showed that Mo concentrations exceeding 100 ppm in sediments are a strong indicator for the presence of H_2S in the water column overlying the sediment. It has also been demonstrated that Mo/Al ratio of the sediments increases in euxinic conditions (Algeo and Lyons, 2006). Low Mo content of the Mn-ore layer yields Mo/Al ratios (not shown) below those typical for the euxinic Black Sea sediments (Eckert et al., 2013). All this is in line with the hypothesis that the Mn-ore layer formed above the deep euxinic waters.

To understand the distribution of trace elements in the Ruslar Formation, it is necessary to consider processes in the suboxic seawater layer and in the underlying anoxic (euxinic) layer. Again, using the modern Black Sea as an analog of the Early Oligocene Western Black Sea, particulates in the euxinic (sulfidic) deep seawater should be enriched in elements that form highly insoluble sulfide minerals, whereas the overlying suboxic seawater should be enriched in those elements that bind strongly to Mn-oxides. From the data reported by Lewis and Landing (1991; 1992), particulate Fe, Pb, and Zn are strongly enriched in deep Black Sea anoxic seawater. Particulate Mn, Cu, and Ni have highest concentrations in the suboxic layer. Yigitheran et al. (2011) also reported a correlation of Fe and Pb in the particulate fraction of the deep Black Sea anoxic seawater. Zn did not correlate well to Fe, possibly owing to anthropogenic contributions, but the authors attributed Zn removal to the formation of sulfides. Particulate Co was strongly associated with Mn, as were U and V. Particulate Cr, Mo, and Ni were strongly correlated to each other, but not to Mn or Fe, and they tended to have irregular vertical distributions. Cu had no associations (Yigitheran et al., 2011). In summary, the euxinic deep seawater has particulates rich in Fe, Pb, and Zn, whereas the suboxic shallow waters have high particulate Mn, Co, U, and V concentrations. The elements Cr, Cu, Mo, and Ni can be with either seawater layer.

For the Ruslar Formation, using leachate compositions as representative of the non-detrital component (Table 4), Mn-rich samples show a strong enrichment in Mg and V and moderate enrichments in Ba, Co, Ni, and P compared to low-Mn samples, but are depleted in Ca, Fe, Pb, and Zn. This pattern is consistent with deposition in the suboxic zone of an euxinic basin like the modern Black Sea.

Strata deposited under anoxic to euxinic conditions are reported from Lower Oligocene sections in various parts of Parathethys, for example the eastern Carpathians (Sachsenhofer et al., 2015), Georgia (Pupp et al., 2018), Azerbaijan (Bechtel et al., 2014). We can hypothesize that the euxinia in the deeper basin sequestered a substantial amount of the dissolved metals that bind to S, most importantly Fe. Manganese does not make easily an insoluble sulfide, which allowed the separation of Mn^{2+} dissolved in the water column from Fe^{2+}, which was incorporated in bottom sediments as Fe-sulfides. The Early Oligocene transgression over the Western Black Sea shelf promoted the deposition of Mn-oxides, which in turn absorbed Ba, Ce, Co, Cu, Ni, and V. During early diagenesis, these Mn-oxides were converted to the Mn-carbonate layers and would have retained most of this array of trace elements (e.g., Johnson et al., 2016). However, as shown by the C isotope patterns described in sub-section *4.4.1*, this scenario of diagenetic formation of carbonates only applies to a portion of the Mn-ore beds. Other portions formed authigenically by direct precipitation from the seawater of the basin as carbonates, and thus would have been less prone to incorporation of those elements that bind to Mn-oxides. In modern Mn-nodules, the most strongly enriched trace elements are Co> Ni> Mn > Cu (Li 2000). These elements, plus Cr and V, are enriched in the diagenetically formed Mn-carbonate layers compared to the authigenic ones, which provides support for our model of Mn-carbonate formation by dual pathways.

5.4. Sr, Nd, and Pb isotope constraints

McArthur and Howarth (2004) report the following Oligocene seawater $^{87}Sr/^{86}Sr$ values (error +/-0.00002): 0.707915 at 32 Ma, 0.70795 at 31 Ma, and 0.70798 at 30 Ma. The average $^{87}Sr/^{86}Sr$ observed in our samples leachates is 0.707966 (+/-0.00012), and excluding one outlier (leachate OBR-5-1264 with $^{87}Sr/^{86}Sr$=0.70837), the average $^{87}Sr/^{86}Sr$ is 0.707941 (+/-0.00006). Both average leachate values (with and without the outlier) are indistinguishable from the Oligocene seawater at 31 Ma, suggesting that all of Sr in the 2*M* HCl leachable fraction was most likely derived from seawater. The slightly elevated values observed in the OBR-5-1264 sample are likely due to minor incorporation of Sr from the residual, detrital fraction during the 2*M* HCl leaching. In contrast to the leachates, the highly radiogenic Sr observed in the residues (presumably representative of the terrigeneous input) indicates input from continental source.

Peucker-Ehrenbrink et al. (2010) reported εNd of about -7.9 for modern Aegean Sea, which is the source for the underflow entering through the Bosporus in Black Sea. Lericolais et al. (2012) reported slightly more negative εNd, from -8.0 to -9.0, for Danube River-derived sediments in the western Black Sea. Nd isotopes in the leachates and bulk samples overall show less negative values when compared to modern day input from Danube and/or Bosporus. However, the less negative values observed in our leachates and bulk samples overlap with the expected values for

Atlantic/Tethys seawater at 31 Ma. The leachates showing lower εNd compared to Atlantic/Tethys (Fig. 11) can be explained either with contribution of Nd from paleo-Danube River or Nd contribution from the residues. Either way, the more negative εNd values indicate contribution from continental source. As can be seen on Figure 11 the leachates and bulk samples extend towards the more negative values represented by the residues. This suggests that Nd (and presumably the REE) is controlled by boundary exchange processes (mixing between seawater and regionally derived detrital input), given the proximity of the sediment deposition area to nearby landmasses.

Based on the regional geological setting, the most likely regional sources for the detrital materials to the Oligocene Western Black Sea was the eastern part of the Moesian Platform (to the west and north-west), the Eastern Balkanides (including eastern Stara Planina and eastern Srednogorie to the west), Strandzha Mountains and Eastern Rhodope Mountains to the south-west. Erosion of Cretaceous-age volcanic cover rocks from the Srednogorie Arc would have supplied detrital material with low $^{87}Sr/^{86}Sr$ (~0.7045; Georgiev et al., 2009). The pre-Mesozoic basement of the Srednogorie Arc, however, would have yielded more radiogenic values, ~0.7076-0.7081 (Georgiev et al., 2009). Detrital material from the Eastern Rhodope Mountains would likely have been blocked from reaching the studied part of the Oligocene Western Black Sea by the Srednogorie Arc, but explosive volcanism could have supplied the tephra component. There are several contemporaneous volcanic centers, but most show either less-radiogenic Sr (0.7073-0.7078), or much higher εNd (-2.8 to -3.8) (Ivanova et al., 2002; Kirchenbau et al., 2012) to explain the trend observed in Sr-Nd isotopes of our samples. Only Mesta volcanics, which contain acidic extrusives with a large component of assimilated crust, can be a possible source as Marchev et al. (2014) reported initial $^{87}Sr/^{86}Sr$ in the range of 0.71080-0.71521 and initial εNd of -6.1 to -8.1.

However, even the Sr-Nd isotopic composition of the Mesta volcanics does not extend to the observed high $^{87}Sr/^{86}Sr$ ratio (as high as 0.72038) and low εNd (as low as -12.1) in the residues, representing the detrital input to the studied area. Therefore, based on the observed data for the sample residues we can rule out volcanoclastic input from the Srednogorie and/or Eastern Rhodope Mountains as a major contributor of the detrital component in the studied area. The high $^{87}Sr/^{86}Sr$ and low εNd observed in the sample residues point to an older, non-arc related source for detrital component, possibly lithologic units in Stara Planina and/or Moesian Platform.

Pb isotopes of the studied samples show a wide range of compositions with no particular relationships observed between leachates and residues (Fig. 12). Overall, the Pb isotope data plot above the mantle evolution line, indicating that Pb was sourced from rocks with continental crust affinity. The overall linear spread in the Pb isotope data can be interpreted as Pb derivation from two sources. The most plausible sediment sources in the region are the Mesozoic Srednogorie Arc and the orogenic belt of Stara Planina, located between the arc terranes and the Moesian Platform. As can be seen on Figure 12, the available data from Srednogorie Arc can explain some of the less radiogenic Pb isotope values in the Obrochishte samples. In particular, 3 out of the 4 residues plot in Srednogorie field close to Vitosha Mountain, a volcano-magmatic complex related to the Mesozoic subduction. In contrast, Stara Planina detritus shows more radiogenic Pb isotopes, close to the bulk and a number of leachates (Fig. 12). It is highly unlikely that the 3 samples available in the literature from Stara Planina represent the full spread of Pb isotope values in the orogenic belt. In addition, it is possible that some of the radiogenic Pb isotopes observed in Obrochishte were derived from suspended sediments carried by proto-Danube River. Overall, the Pb isotopes in the Obrochishte samples indicate continental source for the sediments, consistent with the observed Sr-Nd isotopes in the residues.

5.5. Source of Fe to the Mn-ore layer: Fe isotope constraints

Our data argue for Mn-ore deposition at suboxic conditions in a redox-stratified marine basin representative of the Oligocene Western Black Sea. Studies on the Fe cycle in a modern redox-stratified marine basin (e.g., Black Sea) showed that Fe_{solid} from the oxic shelf is eventually exported to the deep anoxic basin via a benthic shuttle mechanism (Severmann et al., 2008, 2010). It was demonstrated that reduction of the sedimentary Fe deposited at the oxic shelf fractionates Fe isotopes and produces an isotopically light Fe flux to the deep basin (Severmann et al., 2010; Chever et al., 2015). Whereas $\delta^{56/54}Fe$ of the oxic shelf sediments (0.07‰) is close to that of the weathering input (0‰; Dauphas et al., 2017), $\delta^{56/54}Fe$ of the anoxic-euxinic sediments is typically negative, reflecting the value of the Fe shuttle ($\delta^{56/54}Fe$ = -1.2 to -0.7 ‰; Severmann et al., 2008; Rolison et al., 2018) and Fe isotope fractionation during diagenetic pyrite formation (Guilbaud et al., 2011).

Iron isotope composition of the investigated Mn-ore layer is slightly negative: $\delta^{56/54}Fe_{bulk}$ = -0.05‰ (average of 14 measurements; Table 5). Pisoliths from the Mn-ore layer have more negative Fe isotope composition, which is comparable to that of the modern Black Sea anoxic-euxinic sediments: $\delta^{56/54}Fe_{pisolith}$ = -0.22‰ (average of 6 measurements; Table 5), $\delta^{56/54}Fe_{Black\ Sea\ euxinic\ sediments}$ = -0.22‰ (Severmann et al., 2008). These Fe isotope values imply: (i) significant Fe isotope fractionation during diagenesis, such as dissimilatory Fe reduction leading to isotopically lighter Fe in the sediment porewaters, which is then recorded in the pisoliths; (ii) a significant portion of total Fe in the Mn-ore layer has been supplied through a benthic shuttle mechanism (Severmann et al., 2008, 2010) from the shallow oxic shelf sediments.

Compared to the oxic shelf sediments of the modern Black Sea (taken as a prototype of the background oxic sediments of the Oligocene Western Black Sea) that have Fe/Al ratio ranging from 0.5 to 0.6 (Severmann et al., 2008), the studied Mn-ore layers display a large range of Fe/Al: from 0.14 (OBR-11-6.1P) to 2.49 (OBR-11-1.2). This suggests that Fe is depleted in some Mn-ore layers while being enriched in others. The large variation in the excess of Fe content is consistent with a variable efficiency of the Fe shuttle. The lack of relationships between $\delta^{56/54}Fe_{bulk}$ and Fe/Al further suggests that Fe enrichment/depletion processes produced only a limited Fe isotope fractionation.

Because Mn oxidizes more slowly than Fe in seawater, and does not easily form insoluble sulfides in euxinic conditions, a geographic separation of Mn and Fe deposits is often observed in sedimentary Mn deposits. The lack of relationship between Fe/Mn ratio and $\delta^{56/54}$Fe is consistent with a strong decoupling between Fe and Mn enrichment processes, leading to important constraints on the depositional setting of Mn-ore layers. We propose that the limited enrichment of Fe in the Mn deposits result from the combined effect of (i) the efficient trapping of Fe in the deeper part of the basin under euxinic conditions, which is also consistent with limited enrichment in Mo in the deposits (see section 5.3.2.) and (ii) a deepening of the chemocline (suboxic/euxinic interface) below the shelf edge, leading to a decreased efficiency of the Fe shuttle (e.g., Eckert et al., 2013). Considering that Fe requires lower redox potential than Mn to be solubilized, the expansion of suboxic conditions on the shelf would further promote the input of Mn in the water column, which can then be incorporated in Mn deposits either through direct precipitation in the water column, or through co-precipitation of Mn oxides and organic matter and further diagenetic reactions [see below and Maynard (2014)].

5.6. Mechanisms of Mn-carbonate deposition: C and O stable isotope constraints

The studied bulk samples from the Mn-ore bed are mostly composed of Mn-carbonates (Table 1). Hence, the C and O isotope composition of these samples (Table 5) reflects the C and O isotope composition of the Mn-carbonates, the major ore component.

C-O-isotope data distribution along two distinct trends (Fig. 9A), suggests two different mechanisms of Mn-carbonate precipitation at the studied region. All samples from the southern part (south of Obrochishte mine, sites ##6, 7, 8, 9, 10; Fig. 1B) as well as some samples from the north-eastern part of the Ruslar Formation (sites ##1, 2, 3; pisoliths from the lower part of the Mn-ore bed at site #11; Fig. 1B) lie along the mixing line between the modern Danube River water and Oligocene seawater (Fig. 9A). This suggests that C and O in the Mn-carbonates of the ore bed derived from two distinct sources: fresh water and seawater. Oligocene seawater is a reasonable source of C and O in carbonates deposited in the Oligocene marine basin. Questionable remains the fresh water source of C and O in Mn-carbonate deposits, which are interpreted to be submarine based on lithostratigraphic evidence (Aleksiev, 1960a; Stoyanov, 1963). The only possible submarine source of fresh water at continental margins is the submarine groundwater discharge (SGD) (Moore, 2010; Santos et al., 2012). SGD comprises terrestrial fresh groundwater mixed with seawater that has infiltrated coastal aquifers, and flows from the seafloor to the coastal ocean (Moore, 2010). It has recently been recognized as a global phenomenon (and also widespread in the Black Sea; Schubert et al., 2017), which is an important source of fresh water and dissolved elements to the ocean, comparable to the riverine input (Moore, 2010). This water flux contains high concentrations of dissolved inorganic carbon (DIC), Fe, and Mn (Windom et al., 2006; Szymczycha and Pempkowiak, 2016). Thus, the precipitation of Mn-carbonates, which plot along the mixing line between the fresh water and Oligocene seawater C-O-isotope composition (Fig. 9A), is explained by SGD at the Oligocene Western Black Sea shelf. According to the paleogeographical reconstructions (e.g., Nikishin et al., 2015), the area of deposition of the Ruslar Formation was a wide shelf (Western Black Sea basin) bounded by the Balkan High to the south and Moesian High to the north-west during the Oligocene. The elevated landmasses could have provided a sufficient hydraulic head difference to overcome the pressure from seawater and allow groundwater to discharge onto the seafloor.

The proportions of two end-members of the SGD, fresh water and seawater, vary spatially and temporally due to a number of factors (Moore, 2010; Santos et al., 2012). Thus, the spread of the data points between both end-members (Fig. 9A) reflects the different contribution of fresh water and seawater to the C and O isotope composition of the Mn-carbonates. Mn-carbonates in the southern part of the Ruslar Formation (associated with ~400 m thick clays and sandstones; Fig. 1B) formed at higher proportion of fresh SGD than the Mn-carbonates from the north-eastern part of the Ruslar Formation (associated with ~100-250 m thick clays, sandstones, and marls; Fig. 1B) (Fig. 9A).

Mn-carbonates that show precipitation at submarine groundwater discharge with varying contribution of its two components (fresh water and seawater, Fig. 9A) cluster along a trend at the $\delta^{13}C$ – MnO space (Fig. 9B) suggesting precipitation by direct reaction with HCO_3^-. The second group of Mn-carbonate samples comprising those from the upper part of Mn-ore bed at site #11 and lower part of Mn-ore bed at site #5 form distinct arrays at both C-O-isotope diagrams (Fig. 9A, B), suggests they formed by oxidation of organic matter within the sediment. Thus, the Mn-carbonates from the studied Mn-ore bed likely formed via two different mechanisms: (1) precipitation through reaction of dissolved inorganic species (e.g., Mn^{2+} and HCO_3^-), and (2) diagenetic precipitation mediated by oxidation of organic matter. Whereas the second mechanism operated within the sediment, the first may had worked either in the water column or in the near-seafloor sediment pore space.

The average range for C isotopic compositions in sediment-hosted Mn-carbonate ores is -1 to -16‰ (based on a survey of 17 deposits with isotopic data compiled at http://www.sedimentaryores.net/Index_Mn.html). Some samples from the Obrochishte deposit have $\delta^{13}C$ values outside this range, both positive and negative (Table 5). $\delta^{13}C$ values in the range 0 to +5‰ are reported for 6 of the 17 deposits listed in the database cited above, so this is a common situation. Almost all are associated with high Ca/Mn ratio, as are most of the positive values for Obrochishte samples. Such values could result from slight evaporation of seawater, or be from residual CO_2 left from CH_4 fermentation during early diagenesis, with the CH_4 escaping. Two samples from the Obrochishte deposit have very light $\delta^{13}C$ values (Table 5). Similar values have been reported for 3 of the 17 deposits in the database, so this situation is not common, but also not unusual. These values could result from CO_2 totally sourced from oxidation of marine organic matter or, more likely, from oxidation of CH_4.

The long-standing debate on the source of Mn to the Oligocene Western Black Sea and, eventually, to the deposited Mn-carbonates was recently summarized by Vangelova et al. (2005). We will just underline the earlier observations of Aleksiev (1959) on the lithology and stratigraphy of the Oligocene Series in NE Bulgaria and his interpretations about the Mn source to the Oligocene Black Sea basin. He described three (in some sections four) sets of rhyolite tuff layers across the Oligocene Series in NE Bulgaria and noticed that the Mn ore layers either immediately overlie the tuff layers, or are intercalated in them (Aleksiev, 1959; Huff et al., 2014). Based on lithology, mineralogy, and geochemistry studies, Aleksiev (1959) assumed that the tuff layers were a result of submarine volcanic activity within the Oligocene Western Black Sea. He suggested that post-volcanic submarine hydrothermal activity was the source of Mn to the Mn-ore deposits around the modern Black Sea. Later work has not added anything meaningful to this problem except for far-going "exotic" hypotheses about the Mn source and origin of the Mn-ore bed [summarized in Vangelova et al. (2005)].

Based on the interpretation of our C and O isotope data we suggest that in addition to or instead of the inferred submarine hydrothermal source of Mn (Aleksiev, 1959), the submarine groundwater discharge may be another possible Mn source in the Oligocene Western Black Sea. Studies on the redox conditions in the SGD show that they vary from oxic to anoxic depending on the proportions of fresh water and recirculated seawater, and local conditions at the seafloor (Moore, 2010; Santos et al., 2012). Transportation of Mn in dissolved state within the SGD and its input into the marine basin generally requires suboxic to anoxic conditions. Further, the precipitation of Mn in solid phase and deposition at the seafloor requires either high Eh (Eh>530 mV at pH=7 and T=25°C, and preliminary precipitation as Mn-oxyhydroxides), or high alkalinity, or very high dissolved Mn concentrations (direct precipitation as Mn-carbonates).

We may speculate about the mechanisms of Mn-carbonate precipitation at the Oligocene Western Black Sea floor. The REE evidence shows that the eventual Mn-carbonates had formed at suboxic seawater conditions (see *5.2*). Suboxic conditions can exist throughout large volumes of seawater column: suboxic and anoxic marine basins, and oxygen-minimum zone at continental margins. Although we are not aware of existence of highly alkaline conditions in large seawater masses in the modern ocean, we cannot completely rule out the temporary establishment of alkaline conditions in isolated and semi-isolated marine basins. Hence, direct precipitation of Mn-carbonates in the seawater column seems likely when a high flux of dissolved Mn into a suboxic seawater layer is combined with increased alkalinity. In modern times this process has been reported only in lakes (Havig et al., 2018; Herndon et al., 2018).

Could this high Mn flux have been caused by purely sedimentary processes? It is tempting to view the diagenetic Mn as forming from Mn-oxide particles settled in the suboxic water layer, where the highest particulate Mn occurs (e.g., Lewis and Landing, 1991), whereas the authigenic Mn is formed in the underlying anoxic euxinic layer, where the highest dissolved Mn is found (Lewis and Landing, 1991). If this was the case, we would expect to see higher S in the authigenic Mn (deeper water, below the H_2S interface). Furthermore, there should be a weak Ce anomaly in the authigenic Mn precipitates, but a large one in the diagenetic Mn phases. Our results show that the reverse is true for both parameters: S_{tot} averages 0.21% in the authigenic beds compared with 0.54% in the diagenetic beds. Ce/Ce* of the leachate is 0.75 in the authigenic beds, 0.81 in the diagenetic. (We excluded the fresh water-influenced samples from these calculations). Thus, the authigenic beds that dominate the ore body have geochemical properties inconsistent with a deposition in anoxic euxinic deep waters. The only reasonable possibility that remains is precipitation of authigenic Mn-carbonates in the suboxic water column. To have this process working and producing ore-grade Mn deposit there should be high dissolved Mn flux and alkalinity in the suboxic zone.

The group of samples that were strongly affected by SGD (with the highest fresh water contribution), based on C-O-isotopes, have sub-economic concentrations of Mn in all cases (Fig. 9). Hence, it would appear that, at least for the Obrochishte case, an inferred Mn flux from SGD alone was not sufficient to produce a major Mn deposit. Considering the high-Mn samples, all have O-isotopes consistent with precipitation from seawater with a minor fresh water component (presumably SGD) (Fig. 9A). Those, whose C-isotopes indicate diagenetic conversion of Mn-oxide to Mn-carbonate, have trace element signatures suggestive of primary deposition as Mn-oxide. By contrast, the samples whose C-isotopes indicate direct precipitation in seawater column are enriched in Ba, Pb, and Zn, elements that are mobilized and released from the sediment during organic matter-driven diagenesis (Gobeil and Silverberg, 1989; Kerner and Wallmann, 1992; McManus et al., 1994; Hendy, 2010).

5.7. Model of formation of the Obrochishte Mn deposit

There is virtually no direct evidence for hydrothermal Mn input in the Oligocene Western Black Sea other than the tuff layers associated with the deposit. Bulk chemistry of the Obrochishte Mn-ores is the same as background sediment, except for Mn and C. Oxygen isotopes do not suggest a hydrothermal component. Nd, Pb, and Sr isotopes reflect seawater, or local clastics. Textures and sequence stratigraphy seem more or less like any other Phanerozoic deposit. But the mass of Mn contained in this narrow time interval is at least 600×10^6 tons (Maynard, 2010), more than all of the rest of the Phanerozoic deposits combined, and precipitated in only about 500,000 years. This truly remarkable geochemical event suggests some special circumstances at this time interval. The Earth climate was coming off an exceptionally high temperature and high P_{CO2} at the Early Eocene Climatic Optimum (EECO) (50-52 Ma, Zachos et al., 2001). This event was followed by the initiation of glaciation in Antarctica at the end of Eocene and beginning of Oligocene, accompanied by one of the sharpest drops in temperature and sea level in the Phanerozoic. It is likely that the intense chemical weathering during the Eocene produced a thick residuum enriched in kaolinite and Fe- and Mn-oxyhydroxides on the continents and these processes peaked ~35 Ma, during the Late Eocene (see for example Retallack, 2010) (Fig. 13 A). The Early Oligocene sea level fall caused rapid erosion of these lateritic deposits, while at the same time producing restricted basins and anoxic euxinic conditions (Fig. 13 B). The hypothesis of erosion of the Eocene laterites is supported by a recent study (Dekoninck et al., 2019) of the weathering of primary Mn-rich sedimentary rocks (Ordovician) and formation of supergene Mn-deposits (Late Oligocene – Late Neogene) in the Central and Western Europe. It concluded that the old weathering series/systems (e.g., Eocene) must have been removed (at least partly) from the geological record. The erosion products that found their way to the open ocean remained as stable detrital sediments. Fe- and Mn-oxyhydroxides deposited into anoxic euxinic basins (like the Western Black Sea) were dissolved and released Fe and Mn in the seawater. The Fe was reprecipitated as Fe-sulfides while the Mn accumulated as dissolved Mn^{2+} in the anoxic euxinic water column (Fig. 13 B). Suboxic water layer formed as a transition zone between the deep anoxic and surface oxic waters. Steep concentration gradient of dissolved Mn across the suboxic-anoxic interface caused Mn diffusion towards the suboxic layer where it oxidized and sank back into the anoxic waters (Fig. 13 C). The amount of oxidized Mn^{2+} in the suboxic layer was controlled by the available dissolved O_2. Due to the general depletion of O_2 in this layer part of the dissolved Mn supplied from below remained as Mn^{2+}. The weathering-related Mn flux to the Western Black Sea was supplemented by SGD Mn flux. Volcaniclastic layers below and among the Mn-ore layers (Aleksiev, 1959) imply that ash fall dissolution in seawater (e.g., Frogner et al., 2001; Randazzo et al., 2009; Censi et al., 2010) may have additionally supplied Mn in the basin before and during Mn-ore deposition (Fig. 13 C). Alteration of this ash would also have increased alkalinity and raised the dissolved silica level in sediment pore waters (e.g., Lyons et al., 2000).

Was the dissolved Mn stored in the Oligocene Black Sea enough to produce the Mn ores deposited there? The dissolved Mn inventory of the modern Black Sea is about 220×10^6 metric tons (5.03×10^5 km^3 seawater below chemocline with 8 μM dissolved Mn). This amount compares to 550×10^6 tons of Mn in high-grade ores in all Oligocene deposits combined (Maynard, 2014). Assuming an equal mass for low-grade ore, the total resource is about 1000×10^6 tons of Mn. Even if all of the dissolved Mn in the modern Black Sea could be precipitated at once, it would still fall short by a factor of five. How often is this mass of Mn renewed? In the fluxes of Mn to the Black Sea, particulate-borne Mn in river suspended solids dominates substantially over dissolved transport, and the Danube dominates all other river sources. Annual suspended load for the Danube before dam construction was about 47×10^6 tons/year (Oaie et al., 2005) with 1380 mg/kg Mn (Yigiterhan and Murray, 2008). Deep-water sediments contain approximately 620 mg/kg of Mn (Brumsack, 1989) so the net contribution of Mn from the Danube flux is 760 mg/kg or 3.6×10^4 tons/year of Mn. Using the same concentration values for other rivers entering the Black Sea would add another 0.6×10^4 tons, based on suspended loads from Mikhailova (2009). Total river sources would then be 4.2×10^4 tons/year. Some of this river flux is lost to the Mediterranean Sea via the net outflow through the Bosporus Strait, but the amount is very small compared to the river flux. At 4.2×10^4 tons/year it would take only 24000 years to supply all of the Mn in the Oligocene economic deposits. Even if the efficiency were only 10%, there would be adequate supply to account for the existing deposits. But there are no large accumulations of Mn forming in the Black Sea today, suggesting that there must be additional factors beyond the existence of a large euxinic basin responsible for the formation of the ore bodies.

Eocene-Oligocene glaciation had led to an increased ocean alkalinity on a global scale (Coxall et al., 2005). Ephemeral glacial ice (Greenland) and sea ice (Arctic) formed in the Northern Hemisphere (Tripati and Darby, 2018). We can assume that there may have been at least permafrost in northern Europe (the drainage area of the big rivers emptying in Oligocene Black

Sea). This would mean that the groundwater table had lowered in the northern Europe during the cooling event at Eocene-Oligocene boundary.

Early Oligocene warming and sea level rise must have led to a marine transgression over the Western Black Sea shelf. The suboxic layer of vertically stratified seawater would have impinged on the shelf. From what we know from the modern Black Sea, this layer contained both suspended MnO_2 and dissolved Mn^{2+}. Settled MnO_2 particles had diagenetically transformed into $MnCO_3$: MnO_2 dissolution, Mn^{4+} reduction to Mn^{2+}, and Mn^{2+} re-precipitation as $MnCO_3$ (Fig. 13 C).

Early Oligocene warming had caused permafrost/glacier melting in northern Europe, which would have increased the groundwater volume and led to groundwater table rise (e.g., Liljedahl et al., 2017). As a result, the SGD flux should have increased and this would bring HCO_3^- and alkalinity directly in the Western Black Sea shelf. Eocene rocks (potential groundwater aquifer during Early Oligocene) that underlie Obrochishte Mn-layer are mostly carbonates. Hence, high HCO_3^- and alkalinity supply (through SGD and as a result of previous glaciation) to the shelf seems possible.

Thus, dissolved Mn^{2+} precipitation as Mn-carbonates in suboxic water layer overlaps with diagenetic Mn-carbonate precipitation from MnO_2 precursor in the sediment (Fig. 13 C). Dissolved Mn precipitation will draw down its content in the suboxic layer and this will cause pumping of dissolved Mn from the deeper anoxic Mn store due to sharp concentration gradient and molecular diffusion, eddy diffusion and turbulent mixing (e.g., Podymov et al., 2017). This pumping mechanism will supply high dissolved Mn flux to the shelf where it will meet high alkalinity flux and this will result in authigenic precipitation of Mn-carbonates in the seawater column.

5.8. Comparison of Obrochishte Mn-deposit to other Oligocene Mn-deposits around the Black Sea

Although the Oligocene Mn-deposits around the Black Sea have been studied for many years, data is still spotty and incomplete, except for major elements (Table 6). Isotopic data for radiogenic isotopes are not available that we know of, but some information on stable isotopes of C and O has been published [see Kuleshov (2017) for a summary]. However, there is a lack of systematic data where major, trace element, and isotopic data were acquired on the same samples. There is only enough systematic data for us to make comparisons for C and O isotopes for three deposits: Binkiliç (Turkey), Chiatura (Georgia), and Mangyshlak (Kazahkstan). The detailed datasets for each of these deposits are available at http://www.sedimentaryores.net/Manganese/Black%20Sea%20index.html.

Binkiliç Mn-deposit shows a pattern of stable isotopes with a cluster tightly grouped around -6.6 ‰ $\delta^{13}C_{VPDB}$ and -7 ‰ $\delta^{18}O_{VPDB}$ (Fig. 14 A). The C isotopes do not show a correlation with the amount of Mn (Fig. 14 B), which is not consistent with the formation of $MnCO_3$ by reaction of MnO or MnO_2 with organic matter during early diagenesis. Instead, direct precipitation in the water column is more likely. Ozturk and Frakes (1995) interpreted the uniformly light oxygen isotope values as indicating an important role of meteoric water in ore genesis. We speculate that Binkiliç Mn-deposit could have formed in a large freshwater lake.

The Mn-deposits at Chiatura have isotopic values that are strongly overprinted by a late diagenetic event, one that added considerable Ca and some Mn from a fluid with $\delta^{13}C$ and $\delta^{18}O$ close to 0 ‰ (Fig. 14 C,D) [see Kuleshov (2017) for a discussion].

Of the three deposits for which we have sufficient data, Mangyshlak is closest in isotope behavior to Obrochishte. A plot of MnO content vs $\delta^{13}C$ (Fig. 14 E) shows the same two populations as at Obrochishte: (1) has constant $\delta^{13}C$ at all MnO contents, indicating direct precipitation of $MnCO_3$ in the water column (This data population has low R^2 (0.30) and high **p** (0.17), which suggests there has to be some significant additional factor at work for these samples: likely an irregular component of diagenetic addition of lighter $\delta^{13}C$.), and (2) has a negative covariance of MnO content and $\delta^{13}C$, indicating production of $MnCO_3$ via reaction of MnO_2 with organic matter during early diagenesis (This data population has R^2 of 0.82 and a **p** value of 0.01 for the regression, which suggests that this group of samples is well-explained by our model.). A plot of $\delta^{18}O$ vs $\delta^{13}C$ (Fig. 14 F) shows a linear trend to sharply lighter $\delta^{18}O$ at nearly constant $\delta^{13}C$, suggestive of groundwater-seawater mixing, as at Obrochishte, but this time, only calcite is involved.

6. Conclusions

Isotope geochemistry of the Obrochishte Mn-deposit revealed surprising complexity in the details of Mn precipitation. The data indicate involvement of normal seawater and meteoric water (presumably from submarine groundwater discharges onto the seafloor). There was authigenic as well as diagenetic precipitation of the main ore minerals, Mn-carbonates. We present a general model of the formation of the Obrochishte Mn-deposit (Fig. 13) that we believe is applicable to the series of deposits of this age that encircle the present-day Black Sea and explains the peculiar concentration of Mn ores at this time and place. Intense weathering during the Eocene weathering phase produced thick lateritic soils enriched in Fe and Mn. The dramatic sea level fall at the Eocene-Oligocene boundary caused flushing of the lateritic residue into marginal basins while at the same time led to isolation of these basins from the global ocean which fostered anoxic conditions. The sea level fall also produced a much greater head difference between groundwater recharge areas and the continental shelf, which intensified submarine discharge of Mn-bearing groundwater. Continent-derived Fe and Mn were transferred to a redox-stratified Western Black Sea basin, similar to the modern Black Sea. Most of the Fe was sequestered in deep anoxic-euxinic water as sulfides, while Mn accumulated in the suboxic water layer. Transgression of this Mn-rich seawater onto the shallow shelf, and some Mn contribution from submarine ground water discharge, led to the formation of the Oligocene Mn deposits. This unique sequence of events and the configuration of the continental masses around the depositional basin produced the exceptional accumulations of Mn around the Black Sea.

Acknowledgements

V.M. Dekov appreciates the support from the LabexMER (IUEM, UBO, Brest, France) Axis 3 initiative "Geobiological interactions in extreme environments" through grant NODESIS. Many thanks go to Mr. Plamen Neychev (former geologist at Obrochishte mine) who provided the samples from the Obrochishte mine. The numerous suggestions and constructive comments by Andrey Bekker and an anonymous reviewer improved the paper significantly and are highly appreciated.

References

Aleksiev, B., 1959. Oligocene pyroclastic sedimentary rocks from Varna district. Reports of Geological Institute, Bulgarian Academy of Sciences 7, 101-117 (in Bulgarian).

Aleksiev, B., 1960a. Neotocite from the Oligocene Mn-ore bed in Varna district. Mineralogy Collection of the Lvov Geological Society 14, 208-214.

Aleksiev, B., 1960b. Sedimentare Manganerse des Oligozans bei Varna-Bulgarien. Freiberger Forschungshefte C 79.

Aleksiev, B., Nacheva, L., 1966. Characteristic of manganese ore from Obrochishte deposit, Tolbuhin area. Annual of Sofia University, Geology 61, 237-260 (in Bulgarian).

Aleksiev, B., Nacheva, L., 1969. Substantial composition of manganese ore from Obrochishte deposit. Ore Product. Metallurgy 7, 18-20 (in Bulgarian).

Algeo, T.J., Lyons, T.W., 2006. Mo-total organic carbon covariation in modern anoxic marine environments: Implications for analysis of paleoredox and paleohydrographic conditions. Paleoceanography 21, PA1016.

Armstrong-McKay, D.I., Tyrrell, T., Wilson, P.A., 2016. Global carbon cycle perturbation across the Eocene-Oligocene climate transition. Paleoceanography 31, 311-329.

Asael, D., Tissot, F.L.H., Reinhard, C.T., Rouxel, O., Dauphas, N., Lyons, T.W., Ponzevera, E., Liorzou, C., Cheron, S., 2013. Coupled molybdenum, iron and uranium stable isotopes as oceanic paleoredox proxies during the Paleoproterozoic Shunga Event. Chem. Geol. 362, 193-210.

Atanasova, S., Petrov, P., Yanakieva, D., Stanchev, H., 2009. Greigite from the manganese ore bed of Obrochishte deposit, Dobrich district, NE Bulgaria – first data. V International Symposium "Mineral Diversity, Research and Preservation", 12-15 October 2009, Sofia, pp. 255-265.

Basak, C., Martin, E.E., 2013. Antarctic weathering and carbonate compensation at the Eocene-Oligocene transition. Nature Geoscience 6, 121-124.

Bechtel, A., Muvsumova, U., Pross, J., Gratzer, R., Coric, S., Sachsenhofer, R., 2014. The Oligocene Maikop series of Lahich (eastern Azerbaijan): Paleoenvironment and oil-source rock correlation. Org. Geochem. 71, 43-59.

Berger, A., 1968. Geochimie und Lagerstattenkunde des Mangans. Clausthaler Hefte zur Lagerstatt und Geochemie des Mineral Rohstoffe **7**, 216 p.

Berner, R.A., 1982. Burial of organic carbon and pyrite sulfur in the modern ocean: its geochemical and environmental significance. Am. J. Sci. 282, 451-473.

Beukes, N.J., Swindell, E.P.W., Wabo, H., 2016. Manganese deposits of Africa. Episodes 39, 285-317.

Bogdanova, K., 1968. Structure of manganese ore bed in Obrochishte deposit. Rev. Bulg. Geol. Soc. 29, 13-26 (in Bulgarian).

Bonev, N., Dilek, Y., Hanchar, J.M., Bogdanov, K., Klain, L., 2012. Nd–Sr–Pb isotopic composition and mantle sources of Triassic rift units in the Serbo-Macedonian and the western Rhodope massifs (Bulgaria–Greece). Geol. Mag. 149, 146-152.

Brumsack, H.J., 1989. Geochemistry of recent TOC-rich sediments from the Gulf of California and the Black Sea. Geol. Rundsch. 78, 851-882.

Censi, P., Randazzo, L.A., Zuddas, P., Saiano, F., Aricò, P., Andò, S., 2010. Trace element behaviour in seawater during Etna's pyroclastic activity in 2001: Concurrent effects of nutrients and formation of alteration minerals. J. Volcanol. Geoth. Res. 193, 106-116.

Chever, F., Rouxel, O., Croot, P.L., Ponzevera, E., Wuttig, K., Auro, M., 2015. Total dissolvable and dissolved iron isotopes in the water column of the Peru upwelling regime. Geochim. Cosmochim. Acta 162, 66-82.

Coxall, H.K., Wilson, P.A., Pälike, H., Lear, C.H., Backman, J., 2005. Rapid stepwise onset of Antarctic glaciation and deeper calcite compensation in the Pacific Ocean. Nature 433, 53-57.

Dauphas, N., John, S., Rouxel, O., 2017. Iron isotope systematics. Rev. Mineral. Geochem. 82, 415-510.

Dekoninck, A., Monié, P., Blockmans, S., Hatert, F., Rochez, G., Yans, J., 2019. Genesis and $^{40}Ar/^{39}Ar$ dating of K-Mn oxides from the Stavelot Massif (Ardenne, Belgium): Insights into Oligocene to Pliocene weathering periods in Western Europe. Ore Geol. Rev. 115, 103191.

Eckert, S., Brumsack, H.J., Severmann, S., Schnetger, B., Marz, C., Frollje, H., 2013. Establishment of euxinic conditions in the Holocene Black Sea. Geology 41, 431-434.

Friedman, I., O'Neil, J.R., 1977. Compilation of stable isotope fractionation factors of geochemical interest. In: Fleischer, M. (Ed.), Data of Geochemistry, Sixth Edition. U.S. Geological Survey Professional Paper 440-KK. U.S. Government Printing Office, Washington, p. 12.

Frogner, P., Gíslason, S.R., Óskarsson, N., 2001. Fertilizing potential of volcanic ash in ocean surface water. Geology 29, 487-490.

Galimov, E.M., Kodina, L.A., Zhiltsova, L.I., Tokarev, V.G., Vlasova, L.N., Bogacheva, M.P., Korobeinik, G.S., Vaisman, T.I., 2002. Organic carbon geochemistry in the north-western Black Sea–Danube River System. Estuar. Coast. Shelf. Sci. 54, 631-641.

Georgiev, N., Pleuger, J., Froitzheim, N., Sarov, S., Jahn-Awe, S., Nagel, T.J., 2010. Separate Eocene–Early Oligocene and Miocene stages of extension and core complex formation in the Western Rhodopes, Mesta Basin, and Pirin Mountains (Bulgaria). Tectonophysics 487, 59-84.

Georgiev, S., Marchev, P., Heinrich, C.A., von Quadt, A., Peytcheva, I., Manetti, P., 2009. Origin of nepheline-normative high-K ankaramites and the evolution of Eastern Srednogorie arc in SE Europe. J. Petrol. 50, 1899-1933.

Georgiev, S., von Quadt, A., Heinrich, C.A., Peytcheva, I., Marchev, P., 2012. Time evolution of a rifted continental arc: Integrated ID-TIMS and LA-ICPMS study of magmatic zircons from the Eastern Srednogorie, Bulgaria. Lithos 154, 53-67.

German, C.R., Holliday, B.P., Elderfield, H., 1991. Redox cycling of rare earth elements in the suboxic zone of the Black Sea. Geochim. Cosmochim. Acta 55, 3553-3558.

Glazer, B.T., Luther III, G.W., Konovalov, S.K., Friederich, G.E., Trouwborst, R.E., Romanov, A.S., 2006a. Spatial and temporal variability of the Black Sea suboxic zone. Deep-Sea Res. Pt II 53, 1756-1768.

Glazer, B.T., Luther III, G.W., Konovalov, S.K., Friederich, G.E., Nuzzio, D.B., Trouwborst, R.E., Tebo, B.M., Clement, B., Murray, K., Romanov, A.S., 2006b. Documenting the suboxic zone of the Black Sea via high-resolution real-time redox profiling. Deep-Sea Res. Pt II 53, 1740-1755.

Gnoevaya, N., Gribneva, D., Bogdanova, K., 1982. Mineralogical and petrographic description of the Oligocene in Tyulenovo deposit, Tolbuhin district. Rev. Bulg. Geol. Soc. 43, 1, 41-49 (in Bulgarian).

Gobeil, C., Silverberg, N., 1989. Early diagenesis of lead in Laurentian Trough sediments. Geochim. Cosmochim. Acta 53, 1889-1895.

Goldschmidt, V.M., 1954. Geochemistry. University Press, Oxford, 730 p.

Guilbaud, R., Butler, I.B., Ellam, R.M., 2011. Abiotic pyrite formation produces a large Fe isotope fractionation. Science 332, 1548-1551.

Gültekin, A.H., 1998. Geochemistry and origin of the Oligocene Binkiliç manganese deposit; Thrace Basin, Turkey. Turk. J. Earth Sci. 7, 11-23.

Gültekin, A.H., Balcı, N., 2018. Geochemical characteristics of sedimentary manganese deposit of Binkılıç, Trache Basin, Turkey. J. Geol. Geophys. 7, 1000336.

Havig, J.R., Hamilton, T.L., McCormick, M., McClure, B., Sowers, T., Wegter, B., Kump, L.R., 2018. Water column and sediment stable carbon isotope biogeochemistry of permanently redox-stratified Fayetteville Green Lake, New York, USA. Limnol. Oceanogr. 63, 570-587.

Heiser, U., Neumann, T., Scholten, J., Stüben, D., 2001. Recycling of manganese from anoxic sediments in stagnant basins by seawater inflow: a study of surface sediments from the Gotland Basin, Baltic Sea. Mar. Geol. 177, 151-166.

Hendy, I.L., 2010. Diagenetic behavior of barite in a coastal upwelling setting. Paleoceanography 25, PA4103.

Herndon, E.M., Havig, J.R., Singer, D.M., McCormick, M.L., Kump, L.R., 2018. Manganese and iron geochemistry in sediments underlying the redox-stratified Fayetteville Green Lake. Geochim. Cosmochim. Acta. 231, 50-63.

Huff, W.D., Cesta, J., Aucoin, C.D., Harrell, M., Malgieri, T.J., Maynard, J.B., Schwalbaach, C.E., Ugurlu, I., Winrod, A., 2014. Evidence for a Volcanogenic Component to the Obrochishte Mn Ore Deposit, Bulgaria: 2014 Annual Meeting Geological Society of America, Vancouver, British Columbia.

Ivanov, Z., 1988. Aperçu géneral sur l'évolution géologique et structural du massif des Rhodopes dans le cadre des Balkanides. Bulletin de la Société Géologique de France 8, IV, 2, 227-240.

Ivanova, R., Kamenov, G.D., Yanev, Y., 2002. Sr, Nd, and Pb isotopic geochemistry of rhyolites from the Eastern Rhodopes, Bulgaria. Eos Trans. AGU 83 (47), Fall Meet. Suppl., V62B-1413.

Johnson, J.E., Webb, S.M., Ma, C., Fischer, W.W., 2016. Manganese mineralogy and diagenesis in the sedimentary rock record. Geochim. Cosmochim. Acta. 173, 210-231.

Kalinenko, V.V., Shumikhina, I.V., Gusareva, A.I., 1965. Manganiferous sediments and the distribution of V, Cr, Ni, Co and Cu in the Laba Deposit. In: Sapozhnikov, D.G., (Ed.), Manganese Deposits of the Soviet Union. Moscow, Academy of Sciences of the USSR. English translation, 1970, Jerusalem, Israel Program for Scientific Translations, pp. 301-322.

Kamenov, G.D., 2008. High-precision Pb isotopic measurements of teeth and environmental samples from Sofia (Bulgaria): insights for regional lead sources and possible pathways to the human body. Environ. Geol. 55, 669-680.

Kamenov, G.D., Perfit, M.R., Mueller, P.A., Jonasson, I.R., 2008. Controls on magmatism in an island arc environment: study of lavas and sub-arc xenoliths from the Tabar-Lihir-Tanga-Feni island chain, Papua New Guinea. Contrib. Mineral. Petrol. 155, 635-656.

Kerner, M., Wallmann, K., 1992. Remobilization events involving Cd and Zn from intertidal flat sediments in the Elbe estuary during the tidal cycle. Estuar. Coast. Shelf Sci. 35, 371-393.

Kim, S.-T., Mucci, A., Taylor, B.E., 2007. Phosphoric acid fractionation factors for calcite and aragonite between 25 and 75 C: Revisited. Chem. Geol. 246, 135-146.

Kim, S.-T., Coplen, T.B., Horita, J., 2015. Normalization of stable isotope data for carbonate minerals: Implementation of IUPAC guidelines. Geochim. Cosmochim. Acta 158, 276-289.

Kirchenbaur, M., Münker, C., Schuth, S., Garbe-Schönberg, D., Marchev, P., 2012. Tectonomagmatic constraints on the sources of Eastern Mediterranean K-rich lavas. J. Petrol. 53, 27-65.

Konovalov, S.K., Murray, J.W., Luther, G.W., Tebo, B.M., 2006. Processes controlling the redox budget for the oxic/anoxic water column of the Black Sea. Deep-Sea Res Pt II 53, 1817-1841.

Kuleshov, V.N., 2003. Isotopic composition ($\delta^{13}C$, $\delta^{18}O$) and origin of manganese carbonate ores from the Early Oligocene deposits, the Eastern Paratethys. Chem. Erde-Geochem. 63, 329-363.

Kuleshov, V., 2017. Isotope Geochemistry: The Origin and Formation of Manganese Rocks and Ores. Elsevier, Amsterdam, 440 p.

Kuleshov, V.N., Dombrovskaya, Zh.V., 1997. Manganese deposits of Georgia: Communication 1. Geological features and isotopic composition of carbonate manganese ore from the Chiatura and Kvirila deposits. Lithology and Mineral Resources 32, 249-267.

Lenz, C., Jilbert, T., Conley, D.J., Wolthers, M., Slomp, C.P., 2015. Are recent changes in sediment manganese sequestration in the euxinic basins of the Baltic Sea linked to the expansion of hypoxia? Biogeosciences 12, 4875-4894.

Lericolais, G., Bourget, J., Popescu, I., Jorry, S., Popescu, I., Abreu, V., Jouannic, G., Bayon, G., 2012. The "Sink" of the Danube River Basin: The Distal Danube Deep-Sea Fan. In: 32nd Annual Gulf Coast SSEPM Foundation Bob F. Perkins Research Conference: New Understanding of the Petroleum Systems of Continental Margins of the World.

Lericolais, G., Bourget, J., Popescu, I., Jermannaud, P., Mulder, T., Jorry, S., Panin, N., 2013. Late Quaternary deep-sea sedimentation in the western Black Sea: New insights from recent coring and seismic data in the deep basin. Global Planet. Change 103, 232-247.

Lewis, B.L., Landing, W., 1991. The biogeochemistry of manganese and iron in the Black Sea. Deep-Sea Res. 38, S773-S803.

Lewis, B.L., Landing, W.M., 1992. The investigation of dissolved and suspended-particulate trace metal fractionation in the Black Sea. Mar. Chem. 40, 105-141.

Li, Y.-H., 2000. A Compendium of Geochemistry: from Solar Nebula to the Human Brain. Princeton University Press, Princeton, 475 p.

Liljedahl, A.K., Gädeke, A., O'Neel, S., Gatesman, T.A., Douglas, T.A., 2017. Glacierized headwater streams as aquifer recharge corridors, subarctic Alaska. Geophys. Res. Lett. 44, 6876-6885.

Luther, G.W. III, Rozan, T.F., Witter, A., Lewis, B., 2001. Metal-organic complexation in the marine environment. Geochem. Trans. 2, 65.

Lyons, T.W., Murray, R.W., Pearson, D.G., 1995. A comparative study of diagenetic pathways in sediments of the Caribbean Sea: Highlights from pore-water results. Proceedings of the Ocean Drilling Program: Scientific results 165, 287-298.

Mandev, P., 1954. On the Paleogene in the Stalin district. Annual of Sofia University, Geology 49, 73-154 (in Bulgarian).

Marchev, P., Raicheva, R., Downes, H., Vaselli, O., Chiaradia, M., Moritz, R., 2004. Compositional diversity of Eocene-Oligocene basaltic magmatism in the Eastern Rhodopes, SE Bulgaria: implications for genesis and tectonic setting. Tectonophysics 393, 301-328.

Marchev, P., Filipov, P., Peytcheva, I., Münker, C., Kirchenbaur, M., 2014. Coeval felsic igneous magmatism of Mesta Volcanic Complex and Central Pirin Batholith, SW Bulgaria: evidence for extreme crustal assimilation. Abstracts, International Symposium on Eastern Mediterranean Geology. Mugla, Turkey, 13-17 October.2014.

Marcus, M.A., Edwards, K.J., Gueguen, B., Fakra, S.C., Horn, G., Jelinski, N.A., Rouxel, O., Sorensen, J., Toner, B.M., 2015. Iron mineral structure, reactivity, and isotopic composition in a South Pacific Gyre ferromanganese nodule over 4 Ma. Geochim. Cosmochim. Acta 171, 61-79.

Mayer, J., Rupprecht, B.J., Sachsenhofer, R.F., Tari, G., Bechtel, A., Coric, S., Siedl, W., Kosi, W., Floodpage, J., 2017. Source potential and depositional environment of Oligocene and Miocene rocks offshore Bulgaria. Geological Society, London, Special Publications 464, 307-328.

Maynard, J.B., 2010. The chemistry of manganese ores through time: a signal of increasing diversity of earth-surface environments. Econ. Geol. 105, 535-552.

Maynard, J.B., 2014. Manganiferous sediments, rocks, and ores. In: MacKenzie, F.T. (Ed.), *Treatise of Geochemistry 2nd edition. Volume 9, Sediments, Diagenesis, and Sedimentary Rocks*, Elsevier, Amsterdam, pp. 327-349.

Maynard, J.B., Okita, P.M., May, E.D., Martinez-Vera, A., 1990. Paleogeographic setting of manganese mineralization in the Molango district, Mexico. In: Parnell, J. (Ed.), *Mechanisms of Metal Concentration in Sedimentary Basins*, London, International Association of Sedimentologists Special Publication 11, pp. 17-30.

McArthur, J.M., Howarth, R.J., 2004. Strontium isotope stratigraphy. In: Gradstein, F.M., Ogg, J.G., Smith, A.G. (Eds), A Geologic Time Scale 2004, Cambridge University Press, Cambridge, pp. 96-105.

McLennan, S.M., 1989. Rare earth elements in sedimentary rocks: Influence of provenance and sedimentary processes. In: Lipin, B.R., McKay, G.A. (Eds), Geochemistry and Mineralogy of Rare Earth Elements. Rev. Mineral. 21, 169-200.

McManus, J., Berelson, W.M., Klinkhammer, G.P., Kilgore, T.E., Hammond, D.E., 1994. Remobilization of barium in continental margin sediments. Geochim. Cosmochim. Acta 58, 4899-4907.

Mikhailova, D., 2009. Water and sediment runoff at the mouths of rivers flowing into the Black Sea. Environ. Res. Eng. Manag. 48, 5-10.

Milakovska, Z., Djourova, E., Landjeva, E., 2006. Septarian concretions in lower Oligocene sediments of the manganese ore deposit Obrochishte (NE Bulgaria). CR Acad. Bulg. Sci. 59, 1031-1038.

Moore, W.S., 2010. The effect of submarine groundwater discharge on the ocean. Annu. Rev. Mar. Sci. 2, 59-88.

Morel, F.M.M., Price, I.G., 2003. The biogeochemical cycles of trace metals in the oceans. Science 300, 944-947.

Morse, J.W., Berner, R.A., 1995. What determines sedimentary CS ratios? Geochim. Cosmochim. Acta 59, 1073-1077.

Nachev, I.K., 1995. On the Geochemistry of manganese ores in Obrochishte Deposit. CR Acad. Bulg. Sci. 48, 55-58.

Nikishin, A.M., Okay, A., Tüysüz, O., Demirer, A., Wannier, M., Amelin, N., Petrov, E., 2015. The Black Sea basins structure and history: New model based on new deep penetration regional seismic data. Part 2: Tectonic history and paleogeography. Mar. Petrol. Geol. 59, 656-670.

Oaie, G., Secrieru, D., Bondar, C., Ka, S.S., Dutu, L.R., Stanescu, I., Opreanu, G., Dutu, I., Manta, T.V., 2015. Lower Danube River: Characterization of sediments and pollutants. Geo-Eco-Marina 21, 19-34.

Okita, P.M., Maynard, J.B., Spiker, E.C., Force, E.R., 1988. Isotopic evidence for organic matter oxidation by manganese reduction in the formation of stratiform manganese carbonate ore. Geochim. Cosmochim. Acta 52, 2679-2685.

Öztürk, H., Frakes, L.A., 1995. Sedimentation and diagenesis of an Oligocene manganese deposit in a shallow subbasin of the Paratethys: Thrace Basin, Turkey. Ore Geol. Rev. 10, 117-132.

Peucker-Ehrenbrink, B., Miller, M.W., Arsouze, T., Jeandel, C., 2010. Continental bedrock and riverine fluxes of strontium and neodymium isotopes to the oceans. Geochem. Geophys. Geosyst. 11, Q03016.

Podymov, O.I., Zatsepin, A.G., Ostrovsky, A.G., 2017. Vertical turbulent exchange in the Black Sea pycnocline and its relation to water dynamics. Oceanology 57, 492-504.

Poitrasson, F., Freydier, R., 2005. Heavy iron isotope composition of granites determined by high resolution MC-ICP-MS. Chem. Geol. 222, 132-147.

Potter, P.E., Maynard, J.B., DePetris, P., 2005. Mud and Mudstones. Springer-Verlag, Heidelberg, 297 p.

Povinec, P., Ženišová, Z., Šivo, A., Ogrinc, N., Richtáriková, M., Breier, R., 2013. Radiocarbon and stable isotopes as groundwater tracers in the Danube River Basin of SW Slovakia. Radiocarbon 55, 1017-1028.

Puliev, C., Alexiev, B., 1972. On manganese hydrosilicates of Oligocene ore from Northeastern Bulgaria. Annual of Sofia University, Geology 65, 85-96 (in Bulgarian).

Pupp, M., Bechtel, A., Ćorić, S., Gratzer, R., Rustamov, J., Sachsenhofer, R.F., 2018. Eocene and Oligo-Miocene source rocks in the Rioni and Kura basins of Georgia: depositional environment and petroleum potential. J. Petrol. Geol. 41, 367-392.

Raiswell, R., Berner, R.A., 1986. Pyrite and organic matter in Phanerozoic normal marine shales. Geochim. Cosmochim. Acta 50, 1967-1976.

Randazzo, L.A., Censi, P., Saiano, F., Zuddas, P., Aricò, P., Mazzola, S., 2009. Trace elements release from volcanic ash to seawater. Natural concentrations in Central Mediterranean sea. Geophys. Res. Abstr. 11, 2131.

Rank, D., Wyhlidal, S., Schott, K., Jung, M., Heiss, G., Tudor, M., 2014. A 50 years' isotope record of the Danube River water and its relevance for hydrological, climatological and environmental research. Acta Zool. Bulgar. (Supplementum 7), 109-115.

Retallack, G.J., 2010. Lateritization and bauxitization events. Econ. Geol. 105, 655-667.

Rolison, J.M., Stirling, C.H., Middag, R., Gault-Ringold, M., George, E., Rijkenberg, M.J.A., 2018. Iron isotope fractionation during pyrite formation in a sulfidic Precambrian ocean analogue. Earth Planet. Sci. Lett. 488, 1-13.

Rouxel, O.J., Bekker, A., Edwards, K.J., 2005. Iron isotope constraints on the Archean and Paleoproterozoic ocean redox state. Science 307, 1088-1091.

Rouxel, O., Sholkovitz, E., Charrette, M., Edwards, K.J., 2008. Iron isotope fractionation in subterranean estuaries. Geochim. Cosmochim. Acta 72, 3413-3430.

Sachsenhofer, R.F., Stummer, B., Georgiev, G., Dellmour, R., Bechtel, A., Gratzer, R., Ćorić, S., 2009. Depositional environment and hydrocarbon source potential of the Oligocene Ruslar Formation (Kamchia Depression; western Black Sea). Mar. Petrol. Geol. 26, 57-84.

Sachsenhofer, R.F., Hentschke, J., Bechtel, A., Coric, S., Gratzer, R., Gross, D., Horsfield, B., Rachetti, A., Soliman, A., 2015. Hydrocarbon potential and depositional environments of Oligo-Miocene rocks in the Eastern Carpathians (Vrancea Nappe, Romania). Mar. Petrol. Geol. 68, 269-290.

Sachsenhofer, R.F., Popov, S.V., Akhmetiev, M.A., Bechtel, A., Gratzer, R., Groß, D., Horsfield, B., Rachetti, A., Rupprecht, B., Schaffar, W.B., Zaporozhets, N.I., 2017. The type section of the Maikop Group (Oligocene–lower Miocene) at the Belaya River (North Caucasus): Depositional environment and hydrocarbon potential. AAPG Bull. 101, 289-319.

Santos, I.R., Cook, P.L.M., Rogers, L., de Weys, J., Eyre, B.D., 2012. The "salt wedge pump": Convection-driven pore-water exchange as a source of dissolved organic and inorganic carbon and nitrogen to an estuary. Limnol. Oceanogr. 57, 1415-1426.

Schijf, J., de Baar, H.J.W., Wijbrans, J.R., Landing, W.M., 1991. Dissolved rare earth elements in the Black Sea. Deep-Sea Res. 38, S805-S823.

Schubert, M., Knöller, K., Stollberg, R., Mallast, U., Ruzsa, G., Melikadze, G., 2017. Evidence for submarine groundwater discharge into the Black Sea - investigation of two dissimilar geographical settings. Water 9, 468.

Schulz, H.-M., Bechtel, A., Sachsenhofer, R.F., 2005. The birth of the Paratethys during the early Oligocene: from Tethys to an ancient Black Sea analogue? Global Planet. Change 49, 163-176.

Scott, C., Lyons, T.W., 2012. Contrasting molybdenum cycling and isotopic properties in euxinic versus non-euxinic sediments and sedimentary rocks: Refining the paleoproxies. Chem. Geol. 324, 19-27.

Severmann, S., Lyons, T.W., Anbar, A., McManus, J., Gordon, G., 2008. Modern iron isotope perspective on the benthic iron shuttle and the redox evolution of ancient oceans. Geology 36, 487-490.

Severmann, S., McManus, J., Berelson, W.M., Hammond, D.E., 2010. The continental shelf benthic iron flux and its isotope composition. Geochim. Cosmochim. Acta 74, 3984-4004.

Sharma, T., Clayton, R.N., 1965. Measurement of $^{18}O/^{16}O$ ratios of total oxygen of carbonates. Geochim. Cosmochim. Acta 29, 1347-1353.

Stacey, J.S., Kramers, J.D., 1975. Approximation of terrestrial lead isotope evolution by a two-stage model. Earth Planet. Sci. Lett. 26, 207-221.

Stille, P., Steinmann, M., Riggs, S.R., 1996. Nd isotope evidence for the evolution of the paleocurrents in the Atlantic and Tethys Oceans during the past 180 Ma. Earth Planet. Sci. Lett. 144, 9-19.

Stoyanov, E., 1961. On the stratigraphic division of Oligocene in Varna district. Annuaire de la Direction Generale des Recherches Geologiques 12, 123-140 (in Bulgarian).

Stoyanov, E., 1963. Physico-geographical conditions of the Oligocene basin in the Varna district and southeast Dobrodja. Rev. Bulg. Geol. Soc. 24, 29-38 (in Bulgarian).

Sun, S.-S., McDonough, W.F., 1989. Chemical and isotopic systematics of oceanic basalts: implications for mantle composition and processes. In: Saunders, A.D., Norry, M.J., (Eds), Magmatism in the Ocean Basins. Geol. Soc. Spec. Publ. 42, 313-345.

Szymczycha, B., Pempkowiak, J., 2016. State of art and theory of submarine groundwater discharge (SGD). In: Szymczycha, B., Pempkowiak, J., (Eds), The Role of Submarine Groundwater Discharge as Material Source to the Baltic Sea. Springer International Publishing, Switzerland, pp. 3-32.

Tenchov, Y., (Ed.) 1993. Glossary of the Formal Lithostratigraphic units in Bulgaria (1882-1982). Bulgarian Academy of Sciences Publisher, Sofia, 397 p. (in Bulgarian).

Tripati, A., Darby, D., 2018. Evidence for ephemeral middle Eocene to early Oligocene Greenland glacial ice and pan-Arctic sea ice. Nat. Commun. 9, 1038.

Vangelova, V., Vangelov, D., Cvetkov, P., 2005. Genesis of Oligocene manganese ore in Northeast Bulgaria. Annual of Sofia University, Geology 98, 213-230 (in Bulgarian).

Varentsov, I.M., 2002. Genesis of the Eastern Paratethys manganese ore giants: impact of events at the Eocene/Oligocene boundary. Ore Geol. Rev. 20, 65-82.

Varentsov, I.M., Rakhmanov, V.P., 1980. Manganese deposits of the USSR (a review). In: Varentsov, I.M., Grasselly, Gy., (Eds), Geology and Geochemistry of Manganese. Stuttgart, E. Schweizerbart'sche Verlagsbuchhandlung, 2, pp. 319-392.

Varentsov, I.M., Sokolova, A.L., Gor'kova, N.V., Stolyarov, A.S., Ivleva, E.I., Potkonen, N.I., Gorshkov, A.I., 1997. On a geochemical model of the formation of Early Oligocene manganese ores in the Eastern Paratethys: the Nikopol' and other deposits of the southern Ukrainian Basin. Geology of Ore Deposits 39, 40-57.

Vassilev, L., 1967. Mineralogical features of Obrochishte manganese deposit and some implications for its exploration and grade evaluation. Rudodobiv 3, 9-13 (in Bulgarian).

Vassilev, L., Zapryanova, N., Nikiforov, N., 1958. Studies on manganese ores and their host rocks in Varna district. Annuaire de la Direction Generale des Recherches Geologiques 8, 139-210 (in Bulgarian).

Weyer, S., Schwieters, J.B., 2003. High precision Fe isotope measurements with high mass resolution MC-ICPMS. Int. J. Mass Spectrom. 226, 355-368.

Whittaker, E.J.W., Muntus, R., 1970. Ionic radii for use in geochemistry. Geochim. Cosmochim. Acta 34, 945-956.

Windom, H.L., Moore, W.S., Niencheski, L.F.H., Jahnke, R.A., 2006. Submarine groundwater discharge: A large, previously unrecognized source of dissolved iron to the South Atlantic Ocean. Mar. Chem. 102, 252-266.

Yiğiterhan, O., Murray, J.W., 2008. Trace metal composition of particulate matter of the Danube River and Turkish rivers draining into the Black Sea. Mar. Chem. 111, 63-76.

Yiğiterhan, O., Murray, J.W., Tuğrul, S., 2011. Trace metal composition of suspended particulate matter in the water column of the Black Sea. Mar. Chem. 126, 207-228.

Zachos, J., Pagani, M., Sloan, L., Thomas, E., Billups, K., 2001. Trends, rhythms, and aberrations in global climate 65 Ma to Present. Science 292, 686-693.

Figure captions

Fig. 1. (A) Simplified geological map of the tectonic framework of Bulgaria (after Ivanov, 1988) with the location of the studied north-eastern region (B). Each tectonic unit includes several geomorphology structures. Some of them (not all) are mentioned in the paper: e.g., the Balkan Zone includes Stara Planina Mountains, Sredna gora Zone includes Sredna gora (Srednogorie) and Vitosha Mountains, Sakar-Strandzha Zone includes Strandzha Mountains, and Rhodope Massif includes Rhodope Mountains and Mesta Basin. (B) Map of the distribution of the Ruslar Formation in the NE Bulgaria and adjacent Black Sea shelf (based on unpublished data of Juranov and Valchev from 338 drill holes) with the sample sites: white circles = drill holes, black circles = outcrops, black star = mine. Legend: I = Ruslar Formation, in general; II = under-marl unit with the Mn-ore bed at the base; III = marl unit; IV = over-marl unit; V = boundaries of extension of the lithostratigraphic units (LSU), a – proven, b – extrapolated; VI = edge of the continental shelf; VII = fault. Sample site numbers: 1 = C-258a Dobruja drill hole (sample OBR-1-3270), 2 = C-140a Dobruja drill hole (sample OBR-2-1601), 3 = C-170a Dobruja drill hole (sample OBR-3-1622), 4 = C-3a Makedonka drill hole (sample OBR-4-1413), 5 = C-138a Dobruja drill hole (samples OBR-5-1261, -1262, -1263, -1264, -1265, -1266, -1267; -1302), 6 = NE of Pripek village (sample OBR-6-3186), 7 = Kalimanski dol (samples OBR-7-3178, -3205, -4130, -4131), 8 = E of Pripek village (samples OBR-8-4136, -3193, -A, -B), 9 = Ichme kulak (samples OBR-9-3884, -3885), 10 = Kondulak cheshme (sample OBR-10-164), 11 = Obrochishte mine (samples OBR-11-1.2, -1.8, -2.8, -3.8, -4.4, -5.1, -5.7, -6.1). Summary lithostratigraphic core logs representative for different areas (arrows) are shown at the right-hand side.

Fig. 2. Chunk of Mn-ore with concentrically-laminated pisoliths of Mn-carbonates within matrix of Mn-carbonates and clays (sample OBR-11-5.7).

Fig. 3. Photomicrographs (optical polarizing microscope; sample OBR-11-1.2) of: (A) pisolith layers (transmitted light, ‖N); (B) the same as at (A) at ×N, note the carbonate-rich layers (high interference colors) alternating with carbonate-poor layers (light to dark brown); (C) rhodochrosite (rh) layers in pisolith (transmitted light, ‖N); (D) the same as at (C) at ×N; (E) veins of pyrite (black; py) in matrix of Mn-carbonate and clays, note the thin rims of rhodochrosite (white; rh) along the pyrite veins (transmitted light, ‖N); (F) the same as at (E) in reflected light at ‖N; (G) pyrite vein (white; py) (close up) with rhodochrosite rhombic crystals (greyish-black; rh) (reflected light, ‖N); (H) pyrite vein (white; py) (close up) with secondary alterations along cracks and rhodochrosite rhombic crystals (greyish-black; rh) (reflected light, ‖N).

Fig. 4. X-ray fluorescence maps of the distribution of elements across a pisolith within the ore matrix (sample OBR-11-6.1): (A) microphotograph (thin polished section) of the pisolith, general view; (B) X-ray fluorescence scan in Mn K_{α}; (C) X-ray fluorescence scan in Ca K_{α}; (D) X-ray fluorescence scan in Al K_{α}; (E) X-ray fluorescence scan in Si K_{α}; (F) X-ray fluorescence scan in Fe K_{β}; (G) X-ray fluorescence scan in Rb K_{α}; (H) X-ray fluorescence scan in Zr K_{α}. Brighter colors correspond to higher concentrations.

Fig. 5. SEM photomicrographs (SEI; sample OBR-11-6.1) of: (A) laminae of carbonate (composition is consistent with Ca-rhodochrosite: $Mn_{80}Ca_{11}Mg_{7}Fe_{2}$ (mole %)) in pisolith; (B) sub-micron spheres (Si/Mn = 3/1) likely composed of silica and rhodochrosite.

Fig. 6. X-ray fluorescence maps of the distribution of elements across a pyrite vein within the ore matrix (sample OBR-11-1.2): (A) microphotograph (thin polished section) of the pyrite (py) vein (black), general view; (B) X-ray fluorescence scan in Fe K_β; (C) X-ray fluorescence scan in S K_α. Brighter colors correspond to higher concentrations.

Fig. 7. Correlation between S_{tot} and C_{org} concentrations in the studied samples.

Fig. 8. C1 chondrite-normalized (Sun and McDonough, 1989) REE distribution patterns of samples: (A) OBR-11-1.8 (Mn-ore bed); (B) OBR-11 (Mn-ore bed): bulks, 2N HCl leachates, residues; (C) OBR-11 (Mn-ore bed): 2N HCl pisolith leachates, pisolith residues; (D) OBR-5 (Mn-ore bed): 2N HCl leachates, residues; (E) oxic (50 m water depth), suboxic (100 m water depth) and anoxic (2185 m water depth) seawater from Black Sea (German et al., 1991); (F) OBR-8-A (above Mn-ore bed) and average UCC (McLennan, 1989).

Fig. 9. C and O stable isotope correlation diagrams of studied carbonates from Ruslar Formation: (A) $\delta^{18}O$ – $\delta^{13}C$ correlation diagram. Note, the two arrays of the data point distribution: one at constant $\delta^{18}O$, the other with linear $\delta^{18}O$ - $\delta^{13}C$ correlation. Oligocene seawater data from Armstrong-McKay et al. (2016); modern Danube River water data from Povinec et al. (2013) and Rank et al. (2014). (B) $\delta^{13}C$ – MnO correlation diagram. Note, the two trends in data point distribution suggesting two sources of C in Mn carbonates. Squares = samples from the southern part of Ruslar Formation (sites ##6, 7, 8, 9, 10; Fig. 1B); circles (open, blue and green) = samples

from the northern part of Ruslar Formation (sites ##1, 2, 3, 5, 11); blue circles = upper part of Mn-ore bed at site #11; green circles = lower part of Mn-ore bed at site #5.

Fig. 10. Comparison of Sr isotopic compositions of bulk, leachate and residue samples with seawater Sr isotope curve. Note, the residue for sample OBR-5-1264 ($^{87}Sr/^{86}Sr$=0.72038) plots beyond the scale of the plot. Seawater Sr curve from McArthur and Howarth (2004).

Fig. 11. Comparison of Nd isotopic compositions of bulk, leachate and residue samples with Atlantic and Tethys seawater. Seawater field after Stille et al. (1996).

Fig. 12. Pb isotopic compositions of bulk, leachate and residue samples compared to Srednogorie Arc (including Vitosha volcano-magmatic complex) and Stara Planina detritus. Note that there is no particular trend between leachates and residues. Overall, Obrochishte Pb isotopes do not show any significant mantle input and indicate derivation from crustal sources. Sredongorie Arc data from Georgiev et al. (2009), Vitosha and Stara Planina from Kamenov (2008), Continental crust and Mantle evolution lines from Stacey and Kramers (1975).

Fig. 13. Schematic representation of our hypothesis for the sources of Mn, accumulation of dissolved Mn in the Oligocene Western Black Sea water, modes of Mn deposition at the shelf, and formation of Obrochishte Mn deposit (Ruslar Formation, Oligocene Series). (A) Enhanced chemical weathering during the Eocene weathering phase (EECO, 50-52 Ma) resulted in thick laterite crusts rich in Fe- and Mn-oxyhydroxides in the drainage basin of the Western Black Sea. World Ocean (including Western Black Sea) was characterized by a high sea-level stand during

this warm epoch. Groundwater table in the drainage basin was high. (B) Late Eocene cooling that peaked at the Eocene-Oligocene transition (33-35 Ma) led to glaciations (continental ice sheets and sea ice) in both hemispheres. This resulted in low (global) sea-level stand, isolation of the small marine basins (e.g., Black Sea) which in turn provoked onset of anoxia conditions. Sea-level fall drew down the erosional basis of the rivers that led to increased erosion of the laterite crusts. Residually accumulated Fe- and Mn-oxyhydroxides in the laterites were swept away into the ocean. In vertically stratified anoxic marine basins (with oxic, suboxic and anoxic water layers) they remained in suspended state in the oxic and suboxic water layers, but were dissolved in the anoxic deep waters when they sank down. In anoxic-euxinic waters (with free HS^-) dissolved Fe and other chalcophile elements (e.g., Cu, Zn, Pb) were immobilized as sulfides, which settled on the seafloor while dissolved Mn was accumulated in seawater. (C) Early Oligocene warming (25-32 Ma) caused glacier and sea ice melting, and rise of both sea-level and groundwater table. In the anoxic Western Black Sea the suboxic layer migrated upward (synchronously with sea-level rise) and impinged on the shelf. Steep gradient of the dissolved Mn^{2+} concentration across the suboxic-anoxic interface and turbulent mixing caused dissolved Mn flux (molecular diffusion and eddies) from the deep Mn storage to the suboxic water layer. Part of dissolved Mn^{2+} precipitated as MnO_2 and the amount of immobilized Mn^{2+} was controlled by the available O_2 in this layer. Sinking MnO_2 particles could either fall back in the anoxic water where they re-dissolved (Mn^{2+}), or settle on the seafloor in the suboxic layer. The last could be reduced in the presence of organic matter in the sediment and liberated Mn^{2+} may react with CO_2 and precipitate as $MnCO_3$ (diagenetic precipitation). High groundwater table would produce high SGD flux through the seafloor which will supply HCO_3^- and alkalinity to the suboxic water layer. Excess dissolved Mn^{2+} in the suboxic layer would react with HCO_3^- in the alkaline environment and precipitate as $MnCO_3$ in the water column (authigenic precipitation). Volcanic ash fall contemporary of $MnCO_3$ precipitation had supplied additional amount of Mn (through partial dissolution of ash particles) to the basin. Manganese diffusion-turbulent pump from the deep anoxic Mn storage to the suboxic water layer would supply Mn enough for formation of large Mn deposits around the Oligocene Black Sea.

Fig. 14. $\delta^{18}O$ – $\delta^{13}C$ and $\delta^{13}C$ – MnO correlation diagrams of Mn-ore samples from Binkiliç (A, B) [data from Öztürk and Frakes (1995)], Chiatura (C, D) [data from Kuleshov and Dombrovskaya (1997)], and Mangyshlak (E, F) [data from Kuleshov (2003, 2017)] deposits.

- Mn-carbonate ore at the Obrochishte has dual origin: diagenetic and authigenic
- Mn deposition was a result of the climatic events at the Late Eocene-Early Oligocene
- Mn ore was deposited in a redox-stratified basin, similar to the modern Black Sea

Editorial Board
Ore Geology Reviews

Prof. Vesselin Dekov
Department of Marine Resources and Energy
Tokyo University of Marine Science and Technology
4-5-7 Konan, Minato-ku
Tokyo 108-8477
Japan
E-mail: vdekov0@kaiyodai.ac.jp

November 14, 2019

Dear Sirs,

I, on behalf of my co-authors, declare that there is no conflict of interests in our work submitted to your Journal as manuscript entitled “Origin of the Oligocene manganese deposit at Obrochishte (Bulgaria): Insights from C, O, Fe, Sr, Nd, and Pb isotopes” by V.M. Dekov, J.B. Maynard, G.D. Kamenov, O. Rouxel, S. Lalonde and S. Juranov. The manuscript is an original work, not published elsewhere or under consideration for publication elsewhere.

Sincerely Yours

Vesselin Dekov

Table 1
Investigated samples from the Oligocene Mn-ore layer in NE Bulgaria.

Sample ID	Sample type	Sample site	Stratigraphic position	Position, m above base	Mineralogy[a]								
					Rhodochrosite	Kutnahorite	Mn-calcite	Dolomite	Apatite	Quartz	Plagioclase	Illite-smectite	Kaolinite
OBR-1-3270[b]	drill core	C-258a Dobruja	lower part of Ruslar Fmn	below Mn-rich layer	-	2	49	-	-	18	-	31	-
OBR-2-1601	drill core	C-140a Dobruja	lower part of Ruslar Fmn	Mn-rich layer	32	16	-	31	-	14	7	-	-
OBR-3-1622	drill core	C-170a Dobruja	Ruslar Fmn	-	-	-	-	-	-	-	-	-	-
OBR-4-1413	drill core	C-3a Makedonka	lower part of Ruslar Fmn	4.4	-	-	-	-	-	-	-	-	-
OBR-5-1261	drill core	C-138a Dobruja	lower part of Ruslar Fmn	above Mn-rich layer; 13.8	-	-	-	-	-	8	14	77	-
OBR-5-1262	drill core	C-138a Dobruja	lower part of Ruslar Fmn	uppermost Mn-rich layer; 12.4	-	1	-	-	-	17	28	52	3
OBR-5-1263	drill core	C-138a Dobruja	lower part of Ruslar Fmn	Mn-rich layer; 11.3	32	32	36	-	-	-	-	-	-
OBR-5-1264	drill core	C-138a Dobruja	lower part of Ruslar Fmn	Mn-rich layer; 9.3	-	7	-	-	-	18	-	75	-
OBR-5-1265	drill core	C-138a Dobruja	lower part of Ruslar Fmn	Mn-rich layer; 6.3	15	46	-	-	-	25	14	-	-
OBR-5-1266	drill core	C-138a Dobruja	lower part of Ruslar Fmn	Mn-rich layer; 0.9	22	56	-	-	-	22	-	-	-
OBR-5-1267	drill core	C-138a Dobruja	lower part of Ruslar Fmn	base Mn-rich layer; 0.1	13	24	-	-	-	41	22	-	-
OBR-5-1302	drill core	C-138a Dobruja	lower part of Ruslar Fmn	Mn-rich layer	-	26	-	-	-	74	-	-	-
OBR-6-3186	outcrop	NE of Pripek village	lower part of Ruslar Fmn	-	-	-	-	-	-	-	-	-	-
OBR-7-3178	outcrop	Kalimanski dol	lower part of Ruslar Fmn	-	-	23	-	-	-	60	-	17	-
OBR-7-3205	outcrop	Kalimanski dol	lower part of Ruslar Fmn	-	-	-	-	-	-	-	-	-	-

OBR-7-4130	outcrop	Kalimanski dol	lower part of Ruslar Fmn	-	1	-	16	-	-	34	31	17	1
OBR-7-4131	outcrop	Kalimanski dol	lower part of Ruslar Fmn	below Mn-rich layer	-	-	-	-	-	42	31	22	5
OBR-8-3193	outcrop	E of Pripek village	lower part of Ruslar Fmn	below Mn-rich layer	-	-	-	-	-	36	-	64	-
OBR-8-4136	outcrop	E of Pripek village	Avren Fmn	-	-	-	35	-	-	60	-	5	-
OBR-8-A	outcrop	E of Pripek village	lower part of Ruslar Fmn	above Mn-rich layer	-	-	73	-	-	24	3	-	-
OBR-8-B	outcrop	E of Pripek village	lower part of Ruslar Fmn	Mn-rich layer	-	-	-	-	-	-	-	-	-
OBR-9-3884	outcrop	Ichme kulak	lower part of Ruslar Fmn	Mn-rich layer	-	-	27	-	-	14	28	31	-
OBR-9-3885	outcrop	Ichme kulak	lower part of Ruslar Fmn	above Mn-rich layer	-	-	-	-	-	-	-	-	-
OBR-10-164	outcrop	Kondulak cheshme	Ruslar Fmn	7.4	-	-	-	-	-	-	-	-	-
OBR-11-1.2[c]	mine	Obrochishte	Ruslar Fmn	Mn-rich layer; 1.2	29	39	-	32	-	-	-	-	-
OBR-11-1.8	mine	Obrochishte	Ruslar Fmn	Mn-rich layer; 1.8	73	24	-	-	-	1	-	2	-
OBR-11-2.8	mine	Obrochishte	Ruslar Fmn	Mn-rich layer; 2.8	95	-	-	-	-	-	-	5	-
OBR-11-3.8	mine	Obrochishte	Ruslar Fmn	Mn-rich layer; 3.8	95	-	-	-	-	5	-	-	-
OBR-11-4.4	mine	Obrochishte	Ruslar Fmn	Mn-rich layer; 4.4	97	-	-	-	-	2	-	1	-
OBR-11-5.1	mine	Obrochishte	Ruslar Fmn	Mn-rich layer; 5.1	100	-	-	-	-	-	-	-	-
OBR-11-5.1P[d]	mine	Obrochishte	Ruslar Fmn	Mn-rich layer; 5.1	100	-	-	-	-	-	-	-	-
OBR-11-5.7	mine	Obrochishte	Ruslar Fmn	Mn-rich layer; 5.7	-	-	-	-	-	-	-	-	-
OBR-11-6.1	mine	Obrochishte	Ruslar Fmn	Mn-rich layer; 6.1	61	11	-	-	-	-	-	28	-
OBR-11-6.1M[e]	mine	Obrochishte	Ruslar Fmn	Mn-rich layer; 6.1	49	-	-	-	-	2	-	49	-
OBR-	mine	Obrochishte	Ruslar Fmn	Mn-	90	-	-	-	9	-	-	-	-

11-6.1P	te	rich layer; 6.1

[a] %, X-ray diffraction with Rietveld refinement quantification.
[b] The last four digits of the drill core sample IDs denote the depth (m) below surface.
[c] The last two digits of the mine sample IDs denote the distance (m) from the lower boundary of the Mn-ore layer.
[d] Pisolith.
[e] Matrix.

Table 2
EDX data for sample OBR-11-4.4.

	Matrix	Pisolith
SiO_2, wt.%	19.2	6.40
Al_2O_3	3.57	0.19
CaO	2.80	4.09
MgO	5.44	2.24
Fe_2O_3	1.80	0.79
MnO	35.6	52.9
CO_2[a]	31.5	33.7
Total	100.0	100.4

[a] Measured C_{tot} (C_{inorg}+C_{org}) recalculated as CO_2 considering that 88% of C_{tot} is as C_{inorg} in carbonates (bulk sample analyses; Table 3).

Table 3
Chemical composition (XRF) of bulk samples and separated pisoliths.

Sample ID[a]	SiO_2 wt.%	Al_2O_3	CaO	MgO	Fe_2O_3	MnO	K_2O	Na_2O	TiO_2	P_2O_5	LOI	H_2O^-	H_2O^+	C_{tot}[b]	C_{org}[b]	C_{inorg}[b]	S_{tot}[b] ppm	Total wt.%	Mo ppm
Detection limits	0.4	0.5	0.02	0.1	0.02	0.02	0.01	0.2	0.01	0.1	0.2	0.2	0.2	0.02	0.02	0.02	20		3
OBR-1-3270	***30.1***	***13.0***	***16.8***	***2.97***	***8.18***	***0.04***	***1.82***	***0.24***	***0.62***	***b.d.l.***[c]	***26.4***	***3.55***	***22.8***	***4.38***	***0.51***	***3.86***	***4791***	***100.2***	***b.d.l.***
OBR-2-1601	24.0	12.4	14.1	1.13	1.39	18.1	1.52	0.61	0.12	0.20	25.6	1.16	24.5	5.88	0.23	5.64	4303	99.2	b.d.l.
OBR-3-1622	53.9	8.84	1.65	1.16	3.21	8.89	2.42	1.37	0.16	0.24	16.8	2.41	14.4	3.69	0.18	3.51	6859	98.6	b.d.l.
OBR-5-1261	***55.8***	***15.8***	***0.44***	***1.89***	***8.06***	***0.08***	***2.47***	***1.65***	***0.79***	***0.12***	***12.3***	***2.95***	***9.33***	***1.16***	***1.11***	***0.05***	***4229***	***99.3***	***3.35***
OBR-5-1262	54.9	14.5	0.44	1.77	8.62	-	2.47	1.60	0.83	0.12	13.0	3.17	9.85	1.22	1.34	b.d.	5735	98.3	81.2
OBR-5-1263	20.7	12.7	2.78	2.55	1.56	21.8	1.27	1.17	0.20	0.58	33.8	1.20	32.6	8.13	0.48	7.65	1326	99.0	11.0
OBR-5-1264	51.5	16.4	0.41	1.87	8.15	0.27	2.62	1.10	0.95	0.11	15.7	3.88	11.8	0.85	0.70	0.14	3884	99.1	b.d.l.
OBR-5-1265	47.4	15.5	0.41	1.71	8.08	0.25	2.46	1.01	0.95	0.11	21.3	0.35	20.9	6.30	0.21	6.10	3758	99.2	b.d.l.
OBR-5-1266	23.0	12.6	13.6	3.23	4.62	15.6	1.30	0.82	0.20	0.30	24.1	1.18	22.9	6.12	0.36	5.76	2561	99.3	b.d.l.
OBR-5-1267	48.7	11.0	15.5	4.16	4.54	5.13	2.23	1.58	0.57	0.26	4.97	0.41	4.56	3.08	0.36	2.71	3410	98.6	b.d.l.
OBR-5-1302	67.1	4.08	3.66	1.73	2.68	4.80	1.47	0.75	0.04	0.09	12.2	2.09	10.1	2.23	0.27	1.95	21812	100.8	27.0
OBR-6-3186	40.7	12.7	10.8	2.12	3.77	7.17	2.18	0.64	0.53	0.21	18.2	2.09	16.1	2.22	0.12	2.10	459	99.1	17.7
OBR-7-3178	34.9	14.1	2.98	1.58	2.94	15.7	2.05	0.53	0.24	0.32	24.3	5.58	18.7	0.56	0.15	0.40	416	99.6	b.d.l.
OBR-7-3205	40.6	13.7	8.69	2.03	6.27	1.58	2.42	b.d.l.	0.58	0.19	23.0	4.94	18.1	2.81	0.34	2.47	503	99.2	19.7

OBR-7-4130	41.4	13.5	7.22	2.23	3.20	8.01	2.43	0.63	0.53	0.23	20.2	3.85	16.3	1.55	0.16	1.39	1018	99.7	4.35
OBR-7-4131	***60.3***	***15.2***	***3.25***	***0.50***	***3.98***	***0.24***	***2.23***	***0.88***	***0.61***	***0.10***	***11.8***	***2.58***	***9.17***	***1.47***	***0.53***	***0.94***	***1209***	***99.0***	***4.69***
OBR-8-3193	***53.7***	***18.7***	***0.29***	***2.48***	***4.33***	***-***	***0.76***	***b.d.l.***	***0.16***	***b.d.l.***	***19.3***	***2.00***	***17.3***	***0.18***	***0.19***	***b.d.l.***	***640***	***99.9***	***b.d.l.***
OBR-8-4136	39.7	13.3	9.67	1.95	3.80	8.11	1.84	0.49	0.59	0.22	20.2	3.43	16.8	1.87	0.17	1.71	620	99.8	3.24
OBR-8-A	***21.4***	***4.97***	***41.7***	***0.43***	***2.14***	***0.46***	***0.36***	***0.24***	***0.50***	***0.14***	***27.0***	***0.48***	***26.5***	***6.33***	***0.11***	***6.22***	***890***	***99.3***	***b.d.l.***
OBR-8-B	63.4	10.5	0.84	0.15	1.60	9.76	1.32	0.97	0.12	0.21	8.26	1.80	6.46	0.11	0.10	b.d.l.	267	97.1	11.7
OBR-9-3884	26.1	11.0	15.9	1.54	2.82	7.94	1.56	0.38	0.40	0.23	30.7	2.80	27.9	5.47	0.61	4.86	2246	98.5	5.76
OBR-10-164	20.4	14.1	6.57	1.44	5.10	17.0	1.97	b.d.l.	0.35	1.28	31.3	7.48	23.9	2.33	0.15	2.18	885	99.6	b.d.l.
OBR-11-1.2	6.97	1.57	22.2	1.53	2.96	29.6	0.19	0.22	0.09	0.14	34.2	-	-	9.72	0.24	9.48	935	99.6	3.94
OBR-11-1.2P[d]	-	-	-	-	-	-	-	-	-	-	-	-	-	-	0.17	-	681	-	-
OBR-11-1.8	8.00	4.04	11.1	4.26	2.21	36.5	0.58	0.68	0.19	0.28	33.0	-	-	7.72	0.29	7.43	922	100.8	11.9
OBR-11-1.8P	-	-	-	-	-	-	-	-	-	-	-	-	-	-	0.24	-	877	-	-
OBR-11-2.8	3.85	3.80	3.99	6.78	1.71	45.8	0.60	0.85	0.19	0.22	32.0	-	-	7.59	0.26	7.33	815	99.8	8.07
OBR-11-3.8	23.0	7.52	3.07	11.3	1.60	17.8	0.91	1.53	0.35	0.25	32.4	-	-	6.19	0.35	5.84	907	99.7	12.0
OBR-11-3.8P	-	-	-	-	-	-	-	-	-	-	-	-	-	-	0.27	-	819	-	-
OBR-11-4.4	2.15	4.12	2.83	7.53	1.56	43.3	0.44	1.04	0.18	0.47	37.2	-	-	7.72	0.33	7.39	870	100.8	b.d.l.
OBR-11-4.4P	-	-	-	-	-	-	-	-	-	-	-	-	-	-	0.16	-	1242	-	-
OBR-11-5.1	15.7	5.50	2.97	8.11	1.30	32.4	0.79	1.27	0.26	0.18	32.4	-	-	6.97	0.30	6.67	2115	100.9	b.d.l.
OBR-11-5.1P	-	-	-	-	-	-	-	-	-	-	-	-	-	-	0.18	-	1500	-	-
OBR-11-5.7	16.8	4.70	1.60	9.52	0.43	24.9	0.35	1.25	0.24	0.08	40.7	-	-	2.37	-	-	-	100.6	b.d.l.
OBR-11-6.1	-	-	-	-	-	-	-	-	-	-	-	-	-	-	0.43	-	1028	-	-
OBR-11-6.1M[e]	18.9	4.67	1.97	9.14	0.78	21.5	0.41	1.44	0.29	0.30	40.3	-	-	3.88	-	-	-	99.7	b.d.l.
OBR-11-6.1P	-	5.74	9.58	6.82	0.59	32.5	0.31	0.77	0.11	3.52	-	-	-	-	0.23	-	20000	99.5	b.d.l.

[a] In bold italic, samples from the host strata; in regular, samples from the Mn-ore layer.
[b] Elemental analyser data.
[c] Below detection limit.
[d] Pisolith.
[e] Matrix.

Table 4
Chemical composition (ICP-MS) of the investigated samples.

Sample ID[a]	OBR-11-1.2							OBR-11-1.8							OBR-11-2.8			
Element	bulk	leachate	residue	% in the leachate	pisolith leachate	pisolith residue	% in the leachate	bulk	leachate	residue	% in the leachate	pisolith leachate	pisolith residue	% in the leachate	bulk	leachate	residue	% in the leachate
Al, wt.%		0.77	1.38	35.8	0.60	0.75	44.2		1.20	2.05	36.9	0.94	1.27	42.4		1.26	1.38	47.7
Ca		8.32	1.91	81.3	19.5	1.93	91.0		8.04	1.14	87.6	9.52	1.27	88.2		3.11	0.29	91.5
Mg		0.43	0.26	61.8	0.40	0.09	81.2		1.23	0.61	66.7	0.72	0.27	73.1		1.88	0.34	84.5
Fe		1.09	0.93	54.0	0.97	0.36	73.2		1.12	0.91	55.0	0.69	0.51	57.7		0.76	0.57	56.9
Mn		21.6	4.95	81.4	16.0	1.13	93.4		17.9	2.34	88.4	22.6	1.95	92.1		25.5	1.86	93.2
Na		0.20	0.12	61.8	0.13	0.09	59.4		0.42	0.15	73.7	0.25	0.12	67.2		0.43	0.13	76.3
K		0.03	0.14	17.4	0.02	0.05	30.0		0.09	0.30	22.6	0.05	0.12	29.8		0.07	0.21	24.7
P		0.07	0.02	78.3	0.04	0.004	90.5		0.09	0.02	85.0	0.08	0.01	90.9		0.08	0.01	91.0
Li, ppm	13.	5.73	8.70	39.7	3.07	2.13	59.1	88.	40.8	55.2	42.5	20.6	19.8	51.0	34.	20.7	14.4	58.9

	6							3							0			
Sc	1.79	0.23	1.04	17.9	0.11	0.24	30.8	3.68	1.10	2.15	33.8	0.37	0.78	32.4	2.68	0.80	1.28	38.5
Ti	693	105	437	19.4	81.3	164	33.1	1125	176	768	18.6	132	359	26.8	894	201	513	28.1
V	70.7	22.1	56	28.4	13.0	1.76	88.1	200	88.3	95.3	48.1	42.6	13.9	75.4	49.8	42.2	9.31	81.9
Cr	13.3	4.33	10.9	28.4	3.02	3.31	47.7	26.8	9.46	17.0	35.7	5.62	6.44	46.6	18.4	9.06	10.6	46.0
Co	13.3	7.94	3.54	69.2	4.73	1.77	72.8	36.1	26.6	7.98	76.9	20.5	4.78	81.1	26.8	20.1	4.81	80.7
Ni	29.1	20.9	11.2	65.2	15.7	6.37	71.1	118	84.2	37.5	69.2	63.0	21.3	74.8	60.8	46.6	16.6	73.7
Cu	12.6	8.20	8.04	50.5	7.11	2.88	71.2	23.1	15.3	12.2	55.6	13.0	7.41	63.7	13.3	10.2	7.63	57.2
Zn		10.0	8.27	54.8	10.2	4.34	70.2	30.8	28.8	13.0	68.9	19.0	7.76	71.0	16.7	22.7	9.36	70.9
Ga	2.49	0.62	2.16	22.4	0.47	0.79	37.2	4.95	1.38	3.66	27.4	0.84	1.75	32.4	3.74	1.46	2.42	37.6
Rb	13.4	2.12	10.4	16.9	0.92	2.99	23.5	27.1	4.64	20.1	18.7	2.72	8.38	24.5	20.4	3.93	14.5	21.4
Sr	196	147	42.4	77.6	296	34.3	89.6	213	174	32.3	84.3	194	32.0	85.9	102	86.8	15.3	85.0
Y	12.6	8.97	2.66	77.1	5.34	0.49	91.7	15.2	11.3	2.85	79.8	8.72	1.57	84.7	14.4	10.8	1.68	86.5
Zr	11.4	1.06	10.4	9.3	0.84	3.77	18.2	26.4	2.85	20.8	12.1	1.43	9.14	13.5	20.7	2.22	15.3	12.6
Nb	1.34	0.06	1.27	4.7	0.04	0.37	10.0	2.64	0.07	2.64	2.5	0.05	1.00	4.7	1.97	0.04	1.90	2.3
Cs	0.86	0.13	0.68	15.7	0.06	0.19	23.8	1.70	0.22	1.34	14.0	0.13	0.56	19.3	1.25	0.20	0.92	17.6
Ba	222	146	53.7	73.1	183	23.1	88.8	237	156	54.9	74.0	177	37.0	82.7	172	111	33.9	76.7
La	10.5	7.42	2.92	71.8	3.30	0.77	81.0	15.3	11.3	3.92	74.3	7.14	1.86	79.3	11.5	8.08	2.31	77.8
Ce	14.2	11.1	4.77	69.9	4.67	1.18	79.9	20.5	15.3	6.47	70.3	10.1	2.33	81.3	15.5	11.6	3.59	76.4
Pr	2.08	1.26	0.55	69.7	0.56	0.16	77.4	3.08	2.05	0.82	71.6	1.33	0.38	77.7	2.50	1.54	0.48	76.3
Nd	8.45	5.14	2.09	71.1	2.42	0.63	79.3	12.3	8.48	3.16	72.9	5.42	1.45	78.9	10.1	6.47	1.81	78.2
Sm	1.87	1.04	0.38	73.0	0.48	0.11	81.0	2.62	1.69	0.56	75.0	1.13	0.26	81.1	2.21	1.30	0.33	79.9
Eu	0.48	0.26	0.09	74.7	0.15	0.02	86.0	0.63	0.40	0.12	77.4	0.29	0.06	82.3	0.53	0.32	0.07	82.1
Gd	1.98	1.19	0.37	76.2	0.61	0.11	85.3	2.73	1.83	0.51	78.3	1.20	0.25	82.6	2.31	1.44	0.27	84.1
Tb	0.31	0.19	0.06	75.7	0.10	0.02	86.3	0.42	0.28	0.08	78.5	0.20	0.04	82.9	0.36	0.23	0.05	83.0
Dy	1.89	1.14	0.38	75.0	0.64	0.11	85.9	2.41	1.57	0.46	77.5	1.18	0.26	82.0	2.14	1.36	0.26	83.9
Ho	0.41	0.25	0.08	75.6	0.14	0.02	86.5	0.50	0.33	0.10	76.7	0.24	0.05	81.8	0.45	0.30	0.06	83.3
Er	1.21	0.75	0.26	74.0	0.42	0.07	85.4	1.43	0.92	0.30	75.4	0.71	0.18	80.2	1.33	0.85	0.20	81.0
Tm	0.18	0.11	0.04	73.2	0.06	0.01	84.3	0.21	0.13	0.05	73.7	0.10	0.03	78.6	0.20	0.13	0.03	80.4
Yb	1.07	0.61	0.24	71.6	0.34	0.07	83.9	1.28	0.73	0.29	71.6	0.61	0.18	77.5	1.22	0.72	0.21	77.3
Lu	0.17	0.09	0.04	70.0	0.05	0.01	86.1	0.19	0.10	0.04	69.8	0.09	0.02	78.0	0.19	0.11	0.03	76.9
ΣREE	44.8	30.5	12.3		14.0	3.29		63.7	45.1	16.9		29.7	7.36		50.6	34.5	9.69	
(Ce/Ce*)[b]	0.70	0.81	0.86		0.77	0.77		0.69	0.72	0.84		0.75	0.64		0.67	0.76	0.80	
(Eu/Eu*)[c]	0.76	0.73	0.71		0.85	0.68		0.71	0.69	0.65		0.75	0.72		0.71	0.70	0.69	
La_{CN}/Lu_{CN}	6.63	8.84	8.13		6.79	9.87		8.66	11.9	9.52		8.72	8.05		6.59	7.89	7.48	
Hf	0.22	0.04	0.28	12.0	0.03	0.10	20.2	0.60	0.07	0.55	11.4	0.05	0.24	16.5	0.44	0.05	0.40	10.8
Ta	0.07	0.00	0.08	2.0	0.001	0.02	6.4	0.17	0.001	0.16	0.4	0.001	0.04	2.5	0.10	0.001	0.09	0.6
Pb	2.37	2.30	0.69	76.9	9.42	0.29	97.0	6.14	5.95	0.40	93.7	5.30	0.29	94.8	3.33	5.29	0.30	94.6
Th	0.95	0.58	0.52	52.4	0.20	0.17	54.5	2.55	1.54	0.98	60.9	0.79	0.42	65.1	1.96	1.09	0.66	62.3
U	3.25	2.58	0.84	75.5	2.31	0.30	88.4	3.74	3.13	0.84	78.9	1.66	0.37	81.9	1.93	1.51	0.43	77.7

1529

[a] All samples, but OBR-8-A are from the Mn-ore layer. Sample OBR-8-A is from the host strata.

[b] Ce/Ce*=$2Ce_{CN}/(La_{CN}+Pr_{CN})$
[c] Eu/Eu*=$2Eu_{CN}/(Sm_{CN}+Gd_{CN})$

Table 4 *(continued)*

Sample ID	OBR-11-3.8							OBR-11-4.4						
Element	bulk	leachate	residue	% in the leachate	pisolith leachate	pisolith residue	% in the leachate	bulk	leachate	residue	% in the leachate	pisolith leachate	pisolith residue	% in the leachate
Al, wt.%		1.48	1.61	47.9	1.45	1.58	47.9		1.18	1.25	48.5	0.85	0.80	51.5
Ca		2.80	0.32	89.9	3.32	0.22	93.8		2.40	0.12	95.1	2.81	0.18	93.9
Mg		2.31	0.50	82.2	2.36	0.42	84.9		1.40	0.26	84.3	0.88	0.23	79.5
Fe		0.82	0.68	54.4	0.82	0.67	54.8		0.53	0.51	50.7	0.33	0.33	50.4
Mn		20.7	1.89	91.6	23.1	1.20	95.1		28.8	1.28	95.8	32.8	1.45	95.8
Na		0.57	0.16	78.2	0.58	0.14	80.7		0.43	0.12	77.7	0.24	0.10	70.1
K		0.10	0.30	25.3	0.09	0.29	22.7		0.06	0.17	26.1	0.03	0.04	39.6
P		0.09	0.01	88.5	0.09	0.01	91.1		0.06	0.01	89.9	0.09	0.005	94.6
Li, ppm	40.9	23.9	18.1	56.9	23.3	19.0	55.2	22.3	13.8	9.28	59.7	7.10	2.50	74.0
Sc	3.58	1.06	1.76	37.6	0.94	1.97	32.2	2.12	0.51	0.99	34.1	0.10	0.11	48.0
Ti	1143	226	656	25.7	228	705	24.5	741	188	397	32.1	125	147	46.1
V	214	133	35.1	79.1	118	31.5	79.0	118	152	34.3	81.5	75.2	2.11	97.3
Cr	26.9	11.7	13.3	47.0	11.3	14.7	43.4	15.0	8.11	9.72	45.5	2.91	2.52	53.5
Co	41.3	27.5	9.15	75.1	25.7	10.4	71.1	33.3	21.1	9.26	69.5	8.45	8.13	51.0
Ni	118	82.9	32.2	72.0	85.3	35.5	70.6	70.2	46.2	21.2	68.6	24.4	27.4	47.1
Cu	27.2	13.9	15.0	48.1	13.4	15.8	45.8	18.3	11.0	10.9	50.1	4.97	6.66	42.7
Zn	30.9	26.9	12.3	68.5	27.2	12.3	68.8	9.48	18.6	8.77	67.9	10.4	5.07	67.3
Ga	4.90	1.47	3.27	31.0	1.50	3.50	30.0	2.98	1.13	2.10	35.1	0.67	0.78	46.3
Rb	29.5	5.00	21.2	19.1	4.28	23.1	15.7	17.3	3.09	12.4	19.9	1.17	2.95	28.4
Sr	112	87.2	18.9	82.2	92.1	16.3	85.0	87.4	74.8	11.5	86.7	67.9	9.48	87.8
Y	20.9	14.6	2.99	83.0	15.7	2.79	85.0	12.7	9.65	1.03	90.3	10.5	0.57	94.8
Zr	33.4	2.62	20.7	11.2	2.15	23.2	8.5	15.0	1.88	11.2	14.3	1.81	4.31	29.5
Nb	2.78	0.05	2.52	2.0	0.03	2.76	0.9	1.47	0.04	1.42	2.9	0.03	0.33	9.1
Cs	1.85	0.23	1.39	14.5	0.18	1.48	10.8	1.11	0.17	0.79	17.6	0.07	0.19	26.9
Ba	201	117	47.9	71.0	120	46.8	71.9	143	89.3	26.0	77.4	78.9	9.01	89.7
La	16.0	10.8	3.66	74.6	10.9	3.51	75.6	9.41	6.77	1.77	79.3	6.80	0.82	89.3
Ce	21.7	14.6	5.51	72.6	15.6	5.80	73.0	11.0	8.71	2.98	74.5	8.92	1.19	88.2
Pr	3.31	2.02	0.77	72.3	2.12	0.73	74.4	1.99	1.19	0.38	76.1	1.00	0.15	87.3
Nd	13.4	8.55	2.97	74.2	8.83	2.76	76.2	8.21	5.02	1.38	78.5	4.13	0.57	87.9
Sm	2.80	1.72	0.53	76.4	1.83	0.48	79.2	1.83	1.03	0.21	82.8	0.85	0.10	89.2
Eu	0.68	0.42	0.10	80.3	0.44	0.10	81.8	0.44	0.26	0.05	84.6	0.21	0.02	90.9
Gd	3.08	1.97	0.46	81.0	2.07	0.43	82.6	1.93	1.21	0.20	85.7	1.06	0.10	91.7
Tb	0.47	0.31	0.07	80.9	0.33	0.07	82.1	0.31	0.19	0.03	85.2	0.18	0.02	91.0
Dy	2.82	1.87	0.45	80.6	2.00	0.44	81.9	1.88	1.17	0.21	85.0	1.24	0.11	91.5
Ho	0.61	0.40	0.10	80.8	0.43	0.10	81.5	0.40	0.26	0.05	84.7	0.28	0.03	91.2
Er	1.79	1.17	0.31	78.8	1.26	0.30	80.6	1.16	0.75	0.14	84.0	0.84	0.09	90.6
Tm	0.27	0.18	0.05	77.7	0.19	0.05	78.5	0.18	0.10	0.02	81.0	0.14	0.01	90.6
Yb	1.65	1.02	0.33	75.5	1.13	0.33	77.5	1.07	0.64	0.15	80.7	0.80	0.08	90.7
Lu	0.25	0.15	0.05	75.4	0.17	0.05	77.2	0.17	0.09	0.03	78.9	0.12	0.01	90.4
ΣREE	68.8	45.2	15.4		47.3	15.2		40.0	27.4	7.60		26.6	3.30	
Ce/Ce*	0.69	0.72	0.76		0.75	0.84		0.60	0.69	0.85		0.74	0.78	
Eu/Eu*	0.71	0.69	0.62		0.68	0.63		0.72	0.70	0.68		0.66	0.62	
La_{CN}/Lu_{CN}	6.96	7.61	7.91		6.93	7.57		6.02	7.70	7.53		6.00	6.77	
Hf	0.77	0.06	0.54	9.8	0.05	0.63	7.4	0.30	0.04	0.31	12.5	0.04	0.12	24.4
Ta	0.19	0.001	0.13	0.9	0.001	0.15	0.8	0.06	0.001	0.07	0.8	0.001	0.01	4.9
Pb	7.45	5.69	0.35	94.3	11.3	0.72	94.0	1.96	3.21	0.47	87.2	2.65	0.33	88.9
Th	2.71	1.40	1.03	57.6	1.44	1.09	57.0	1.48	0.86	0.48	64.5	0.28	0.16	64.2
U	4.08	3.25	0.78	80.6	2.95	0.69	81.0	3.88	3.44	0.49	87.5	1.78	0.19	90.3

Table 4 *(continued)*

Sample ID	OBR-11-5.1							OBR-11-5.7				OBR-11-6.1				
Element	bulk	leachate	residue	% in the leachate	pisolith leachate	pisolith residue	% in the leachate	bulk	leachate	residue	% in the leachate	bulk	pisolith bulk	pisolith leachate	pisolith residue	% in the leachate
Al, wt.%		1.14	1.29	47.0	1.13	1.04	52.1		2.08	1.43	59.3			1.26	1.05	54.4
Ca		2.08	0.43	82.9	2.35	0.19	92.7		0.93	0.14	86.8			4.46	0.52	89.5
Mg		1.47	0.50	74.7	1.11	0.26	81.1		2.85	1.19	70.6			1.92	0.49	79.7
Fe		0.77	0.93	45.4	0.51	0.61	45.6		0.62	0.81	43.3			0.49	0.64	43.6
Mn		27.8	3.80	88.0	30.4	1.94	94.0		17.3	0.99	94.6			23.8	2.68	89.9
Na		0.42	0.16	72.1	0.38	0.13	75.3		0.82	0.16	83.6			0.47	0.14	76.9

K		0.06	0.20	24.6	0.05	0.09	33.6		0.10	0.23	29.7			0.06	0.11	35.4
P		0.05	0.01	87.0	0.05	0.01	89.2		0.06	0.01	89.2			1.08	0.12	89.8
Li, ppm	22.0	13.9	11.8	54.2	8.19	5.94	57.9	28.2	19.8	12.8	60.6	33.7	23.2	18.4	7.37	71.4
Sc	2.14	0.58	1.23	32.2	0.28	0.49	35.9	2.83	0.53	2.00	21.0	3.13	1.62	0.58	0.56	50.6
Ti	799	171	480	26.2	162	245	39.8	1120	231	790	22.6	1052	635	189	323	36.9
V	111	104	16.6	86.2	86.0	6.98	92.5	227	232	26.8	89.7	553	329	306	51.1	85.7
Cr	16.0	7.78	7.93	49.5	4.33	4.93	46.7	17.6	7.89	11.0	41.8	30.9	11.9	8.04	7.48	51.8
Co	31.7	19.1	11.8	61.8	12.9	7.42	63.4	22.1	17.9	3.86	82.3	65.5	44.5	32.2	10.3	75.7
Ni	129	79.4	68.7	53.6	53.6	47.1	53.2	107	98.6	24.7	80.0	151	127	79.5	48.8	61.9
Cu	20.6	7.82	15.8	33.1	6.68	8.82	43.1	15.3	8.60	9.82	46.7	36.1	27.7	11.2	19.7	36.3
Zn	5.17	16.4	10.0	62.0	12.8	7.82	62.0	17.4	21.8	12.7	63.3	42.7	12.7	23.3	7.49	75.7
Ga	3.05	1.07	2.38	31.0	0.82	1.36	37.7	4.79	2.82	2.47	53.4	4.97	2.52	1.75	1.49	54.1
Rb	17.6	3.04	14.5	17.3	1.83	6.95	20.8	20.2	3.36	16.2	17.2	23.7	11.7	2.89	8.00	26.6
Sr	77.3	66.7	20.4	76.6	63.1	11.4	84.7	84.3	81.4	13.6	85.7	113	399	326	44.6	88.0
Y	14.1	11.0	3.15	77.8	9.87	1.05	90.4	13.4	10.2	2.75	78.8	22.2	64.9	54.9	6.73	89.1
Zr	18.6	1.70	14.3	10.6	1.91	7.58	20.1	24.1	2.21	20.5	9.8	31.7	14.4	4.17	8.64	32.5
Nb	1.64	0.03	1.75	1.8	0.03	0.81	3.8	2.93	0.04	3.26	1.2	2.78	1.13	0.11	1.30	7.8
Cs	1.11	0.16	0.84	15.8	0.09	0.45	16.5	0.92	0.12	0.75	14.2	1.56	0.76	0.18	0.52	25.7
Ba	143	85.9	42.3	67.0	77.2	16.9	82.0	191	95.2	84.3	53.0	159	261	192	37.7	83.6
La	9.24	6.46	3.32	66.1	5.33	1.70	75.8	11.5	8.78	2.94	74.9	18.1	52.5	48.3	6.62	88.0
Ce	11.6	8.80	4.26	67.4	7.25	2.81	72.1	18.5	14.2	5.80	71.0	25.3	62.0	58.2	8.73	87.0
Pr	2.07	1.24	0.70	63.9	0.94	0.36	72.3	2.81	1.86	0.78	70.5	3.42	7.17	6.23	0.96	86.6
Nd	8.63	5.22	2.68	66.1	3.95	1.37	74.2	11.2	7.33	3.13	70.0	13.9	28.9	25.8	3.89	86.9
Sm	1.96	1.11	0.49	69.5	0.82	0.25	76.8	2.43	1.48	0.67	68.7	2.88	5.69	5.03	0.72	87.5
Eu	0.49	0.27	0.11	71.9	0.21	0.04	85.2	0.55	0.32	0.12	73.1	0.68	1.41	1.19	0.16	87.9
Gd	2.08	1.33	0.47	74.0	1.00	0.21	82.7	2.46	1.49	0.55	73.1	3.26	7.28	6.28	0.84	88.1
Tb	0.35	0.22	0.07	75.8	0.18	0.03	84.9	0.38	0.24	0.09	73.4	0.49	1.12	0.97	0.13	88.5
Dy	2.13	1.39	0.45	75.3	1.20	0.20	85.5	2.17	1.37	0.51	72.9	2.93	6.98	6.13	0.83	88.0
Ho	0.46	0.31	0.10	76.0	0.28	0.04	86.7	0.46	0.29	0.10	74.0	0.62	1.54	1.37	0.18	88.3
Er	1.40	0.95	0.32	74.7	0.89	0.14	86.7	1.34	0.85	0.31	73.5	1.81	4.48	4.02	0.55	88.0
Tm	0.21	0.14	0.05	74.3	0.14	0.02	86.5	0.21	0.13	0.05	73.4	0.26	0.62	0.58	0.08	88.1
Yb	1.30	0.83	0.33	71.8	0.83	0.14	86.0	1.24	0.77	0.29	72.9	1.56	3.83	3.31	0.48	87.4
Lu	0.20	0.12	0.05	71.1	0.12	0.02	86.1	0.20	0.12	0.04	73.2	0.23	0.54	0.47	0.07	86.9
ΣREE	42.1	28.4	13.4		23.1	7.32		55.5	39.2	15.4		75.5	184	168	24.2	
Ce/Ce*	0.62	0.71	0.65		0.73	0.84		0.77	0.82	0.92		0.74	0.68	0.71	0.75	
Eu/Eu*	0.74	0.68	0.67		0.70	0.47		0.68	0.65	0.58		0.68	0.67	0.65	0.64	
La_{CN}/Lu_{CN}	4.94	5.74	7.27		4.59	9.05		6.33	8.02	7.33		8.25	10.4	10.9	9.89	
Hf	0.41	0.04	0.39	8.9	0.04	0.20	16.2	0.62	0.05	0.62	7.8	0.68	0.30	0.09	0.25	26.5
Ta	0.10	0.001	0.08	1.3	0.001	0.05	2.1	0.19	0.001	0.20	0.6	0.31	0.06	0.005	0.09	4.8
Pb	2.75	2.85	0.30	90.6	3.14	0.45	87.4	10.7	12.0	0.39	96.8	9.31	6.06	5.22	1.66	75.9
Th	1.51	0.88	0.74	54.2	0.47	0.52	47.4	4.66	3.83	1.00	79.3	2.44	1.43	0.85	0.46	64.6
U	3.92	3.24	1.12	74.3	2.17	0.37	85.5	2.85	2.96	0.42	87.7	10.9	10.5	9.88	1.31	88.3

Table 4 *(continued)*

Sample ID	OBR-5-1263			OBR-5-1264			OBR-5-1265			OBR-5-1266			OBR-5-1267			OBR-5-1302			OBR-8-A		
Element	leachate	residue	% in the leachate	leachate	residue	% in the leachate	leachate	residue	% in the leachate	leachate	residue	% in the leachate	leachate	residue	% in the leachate	leachate	residue	% in the leachate	leachate	residue	% in the leachate
Al, wt.%	0.92	1.49	38.3	0.97	7.15	11.9	0.83	1.95	29.8	0.96	2.22	30.2	0.92	3.10	22.8	0.82	2.10	28.1	0.70	1.69	29.4
Ca	8.78	0.95	90.2	0.20	0.05	78.5	11.9	0.91	92.9	5.94	0.54	91.6	5.98	0.73	89.2	2.45	0.15	94.3	20.3	3.61	84.9
Mg	0.83	0.31	72.6	0.22	0.68	24.1	0.53	0.19	73.7	1.23	0.41	75.0	0.66	0.59	53.0	0.51	0.20	71.4	0.07	0.09	42.9
Fe	1.37	0.87	61.1	1.48	3.35	30.6	0.62	1.06	37.0	0.99	1.11	47.1	0.74	1.76	29.6	0.69	2.40	22.4	0.26	0.51	34.1
Mn	25.8	2.72	90.5	0.28	0.05	85.0	7.34	0.57	92.8	14.1	1.19	92.2	3.94	0.47	89.3	4.51	0.13	97.1	0.02	0.02	43.6
Na	0.48	0.14	77.2	0.45	0.42	52.2	0.23	0.38	37.9	0.42	0.36	54.1	0.43	0.48	47.4	0.32	0.41	44.1	0.09	0.35	21.0
K	0.07	0.26	20.8	0.12	1.56	7.4	0.07	0.75	8.3	0.06	0.70	8.3	0.10	1.67	5.6	0.11	0.74	13.3	0.03	0.50	5.3
P	0.33	0.04	89.7	0.03	0.02	61.9	0.07	0.01	86.2	0.11	0.01	88.3	0.10	0.02	83.7	0.09	0.01	91.7	0.05	0.01	75.3
Li, ppm	17.0	22.1	43.5	8.08	65.1	11.0	6.10	7.87	43.7	36.0	26.3	57.8	32.4	44.6	42.0	14.3	9.13	61.0	1.40	6.33	18.2
Sc	0.54	1.43	27.3	3.62	11.9	23.3	0.25	0.82	23.1	0.49	1.68	22.5	0.59	2.59	18.4	0.83	1.13	42.3	bdl	0.79	0.0
Ti	106	598	15.1	102	4525	2.2	103	448	18.7	112	737	13.2	118	980	10.7	113	615	15.5	83.1	602	12.1
V	51.4	98.6	34.3	10.5	152	6.5	15.2	29.9	33.7	66.5	129	33.9	31.8	126	20.2	22.6	28.1	44.6	2.67	19.7	11.9
Cr	5.32	15.6	25.4	7.36	102	6.7	4.96	16.7	22.9	8.78	20.0	30.5	7.79	34.3	18.5	14.5	24.2	37.4	2.13	8.30	20.4
Co	14.5	6.35	69.6	10.7	12.7	45.7	4.76	2.83	62.7	11.5	5.92	66.0	14.5	7.75	65.1	15.6	7.27	68.1	0.26	0.67	28.3
Ni	87.8	34.6	71.7	26.9	37.9	41.5	29.7	29.4	50.3	34.8	24.1	59.1	56.9	44.7	56.0	68.2	47.0	59.2	5.71	5.01	53.3
Cu	45.6	20.4	69.1	21.8	16.4	57.1	7.61	10.4	42.1	17.0	18.8	47.6	49.2	20.3	70.7	16.3	21.6	43.1	10.2	4.43	69.6
Zn	34.4	10.9	75.9	46.7	56.5	45.3	18.7	10.5	64.1	32.7	14.4	69.5	45.1	21.3	67.9	23.6	10.3	69.6	7.80	9.06	46.3
Ga	1.00	2.76	26.6	1.31	19.9	6.2	0.68	3.11	17.9	1.22	3.97	23.5	0.88	6.02	12.7	1.17	3.57	24.6	0.44	2.36	15.6
Rb	3.44	16.7	17.1	7.50	24.9	23.2	2.43	32.4	7.0	3.76	30.3	11.0	4.58	62.7	6.8	3.84	33.1	10.4	0.91	20.6	4.2
Sr	360	47.6	88.3	62.1	40.6	60.5	234	65.3	78.2	158	45.7	77.6	136	66.0	67.3	127	61.5	67.3	44.4	42.5	51.1
Y	14.6	2.62	84.8	15.4	1.74	89.8	10.9	1.32	89.2	14.7	2.37	86.1	15.8	3.62	81.4	19.2	1.42	93.1	2.04	1.12	64.6
Zr	2.00	19.6	9.2	3.21	109	2.9	1.54	11.4	11.9	2.23	23.1	8.8	2.90	28.4	9.3	1.09	22.2	4.7	0.55	13.3	4.0
Nb	0.05	2.58	1.7	0.04	13.0	0.3	0.05	1.53	3.1	0.05	2.80	1.9	0.05	4.12	1.2	0.05	2.24	2.1	0.02	1.83	1.3
Cs	0.14	1.02	11.8	0.36	2.58	12.2	0.09	0.79	10.6	0.17	1.16	12.9	0.14	1.80	7.3	0.12	0.97	11.2	0.07	0.54	10.8
Ba	632	100	86.3	61.4	177	25.8	81.3	196	29.3	87.1	155	36.0	43.2	311	12.2	91.0	204	30.9	3.79	139	2.7
La	12.4	4.19	74.7	15.7	1.67	90.4	10.2	2.11	82.9	10.5	3.61	74.5	12.6	4.46	73.9	11.6	3.02	79.4	2.28	1.95	53.9
Ce	17.6	7.07	71.4	35.5	5.65	86.3	15.8	3.70	81.0	17.5	6.53	72.8	21.1	8.12	72.2	20.8	5.67	78.6	2.77	3.51	44.1
Pr	2.14	0.87	71.2	4.41	0.50	89.8	1.90	0.43	81.7	2.20	0.76	74.4	2.83	0.99	74.1	2.71	0.65	80.7	0.49	0.42	53.6
Nd	8.98	3.29	73.2	18.2	2.09	89.7	7.87	1.68	82.4	9.21	2.79	76.7	11.9	3.79	75.8	11.3	2.35	82.8	1.94	1.60	54.8
Sm	1.81	0.60	75.0	3.92	0.45	89.7	1.58	0.31	83.7	1.90	0.53	78.3	2.50	0.74	77.2	2.45	0.41	85.6	0.40	0.30	57.6
Eu	0.51	0.11	81.8	0.84	0.12	87.3	0.36	0.11	75.9	0.43	0.13	76.1	0.54	0.23	70.1	0.55	0.13	80.6	0.08	0.10	44.3
Gd	2.06	0.53	79.5	3.60	0.39	90.2	1.66	0.27	86.1	2.03	0.43	82.5	2.60	0.63	80.4	2.71	0.33	89.1	0.37	0.24	60.4

Tb	0.31	0.08	79.7	0.55	0.08	87.9	0.26	0.04	86.4	0.32	0.07	83.1	0.39	0.10	79.9	0.43	0.05	89.8	0.06	0.04	60.2
Dy	1.87	0.43	81.2	3.00	0.49	86.0	1.45	0.24	85.8	1.81	0.39	82.4	2.19	0.59	78.9	2.46	0.28	89.8	0.32	0.23	57.9
Ho	0.39	0.09	81.5	0.54	0.11	83.1	0.30	0.05	85.2	0.38	0.08	82.3	0.44	0.12	79.0	0.51	0.05	90.4	0.07	0.05	58.7
Er	1.14	0.28	80.3	1.46	0.37	79.7	0.85	0.15	84.7	1.08	0.25	81.3	1.19	0.36	76.9	1.47	0.18	89.3	0.17	0.14	53.8
Tm	0.16	0.04	79.7	0.20	0.07	74.9	0.12	0.02	83.8	0.15	0.04	79.2	0.16	0.06	74.2	0.21	0.03	88.9	0.02	0.02	49.0
Yb	0.93	0.27	77.5	1.18	0.47	71.4	0.70	0.14	83.3	0.83	0.25	76.9	0.91	0.35	72.0	1.20	0.17	87.5	0.14	0.16	46.1
Lu	0.13	0.04	75.7	0.17	0.07	69.2	0.10	0.03	79.9	0.12	0.04	77.1	0.13	0.06	70.5	0.17	0.03	86.4	0.02	0.02	44.7
ΣREE	50.4	17.9		89.2	12.5		43.1	9.27		48.5	15.9		59.4	20.6		58.6	13.4		9.12	8.78	
Ce/Ce*	0.77	0.86		1.03	1.50		0.82	0.90		0.85	0.92		0.83	0.91		0.88	0.95		0.61	0.91	
Eu/Eu*	0.81	0.60		0.67	0.87		0.67	1.19		0.66	0.84		0.65	1.02		0.65	1.06		0.59	1.06	
La_{CN}/Lu_{CN}	10.2	10.8		9.98	2.39		11.0	9.02		9.47	10.9		10.3	8.67		7.41	12.2		12.1	8.37	
Hf	0.05	0.51	9.1	0.13	3.02	4.2	0.05	0.34	12.9	0.07	0.66	9.8	0.08	0.85	8.4	0.04	0.62	6.3	0.02	0.40	4.7
Ta	0.001	0.17	0.7	0.001	0.85	0.1	0.001	0.11	0.9	0.001	0.18	0.4	0.001	0.31	0.3	0.002	0.16	1.1	0.001	0.14	0.4
Pb	9.75	1.49	86.7	19.0	8.30	69.5	4.98	5.35	48.2	6.50	4.48	59.2	6.37	7.72	45.2	3.91	4.41	47.0	4.70	3.75	55.7
Th	1.03	0.87	54.2	5.67	1.95	74.5	0.90	0.42	68.0	1.36	0.79	63.2	2.01	1.06	65.4	1.64	0.74	68.9	0.15	1.24	10.6
U	1.98	0.50	79.7	1.00	1.42	41.2	1.06	0.34	75.7	1.70	0.52	76.7	2.57	0.82	75.9	1.68	0.45	78.7	0.87	0.40	68.6

Table 5
Isotope composition of the investigated samples.

Sample ID[a]	Sample type	$\delta^{13}C_{PDB}$ (‰)	$\delta^{18}O_{PDB}$ (‰)	$\delta^{56/54}Fe_{IRMM14}$ (‰)	$^{87}Sr/^{86}Sr$	$^{143}Nd/^{144}Nd$	εNd	$^{206}Pb/^{204}Pb$	$^{207}Pb/^{204}Pb$	$^{208}Pb/^{204}Pb$
OBR-1-3270	***bulk***	***2.04***	***-1.50***	-	-	-	-	-	-	-
OBR-2-1601	bulk	0.12	-0.53	-	-	-	-	-	-	-
OBR-3-1622	bulk	-2.76	-1.50	-	-	-	-	-	-	-
OBR-5-1261	***bulk***	-	-	-	-	-	-	-	-	-
OBR-5-1262	bulk	-	-	0.24	-	-	-	-	-	-
OBR-5-1263	bulk	-0.13	-1.13	-0.25	-	-	-	-	-	-
OBR-5-1263	leachate	-	-	-	0.70791	0.512296	-6.7	18.553	15.632	38.415
OBR-5-1264	bulk	-	-	0.16	-	-	-	-	-	-
OBR-5-1264	leachate	-	-	-	0.70837	0.512289	-6.8	18.337	15.596	38.318
OBR-5-1264	residue	-	-	-	0.72038	0.512193	-8.7	18.668	15.614	38.680
OBR-5-1265	bulk	-9.02	-1.57	-0.19	-	-	-	-	-	-
OBR-5-1265	leachate	-	-	-	0.70788	0.512277	-7.0	18.868	15.660	38.669
OBR-5-1266	bulk	-8.42	-1.02	-0.06	-	-	-	-	-	-
OBR-5-1266	leachate	-	-	-	0.70794	0.512291	-6.8	19.253	15.706	38.896
OBR-5-1267	bulk	-5.81	-3.23	0.04	-	-	-	-	-	-
OBR-5-1267	leachate	-	-	-	0.70795	0.512285	-6.9	19.339	15.709	38.940
OBR-5-	bulk	-9.01	0.02	-0.33	-	-	-	-	-	-

1302										
OBR-5-1302	leachate	-	-	-	0.70796	0.512260	-7.4	18.823	15.654	38.659
OBR-5-1302	residue	-	-	-	0.71336	0.512018	-12.1	18.697	15.648	38.762
OBR-6-3186	bulk	-1.86	-6.13	-	-	-	-	-	-	-
OBR-7-3205	bulk	-1.28	-3.69	-	-	-	-	-	-	-
OBR-7-4130	bulk	-0.24	-7.31	-	-	-	-	-	-	-
OBR-7-4131	***bulk***	***0.45***	***-4.62***	-	-	-	-	-	-	-
OBR-8-3193	***bulk***	***-0.96***	***-3.19***	-	-	-	-	-	-	-
OBR-8-4136	bulk	-2.39	-6.08	-	-	-	-	-	-	-
OBR-8-A	***bulk***	***-4.26***	***-9.19***	***-***	***-***	***-***	***-***	***-***	***-***	***-***
OBR-8-A	***leachate***	***-***	***-***	***-***	***-***	***0.512281***	***-7.0***	***18.262***	***15.597***	***38.039***
OBR-8-B	bulk	-10.5	-12.2	-	-	-	-	-	-	-
OBR-9-3884	bulk	-1.79	-2.32	-	-	-	-	-	-	-
OBR-10-164	bulk	-0.60	-2.17	-	-	-	-	-	-	-
OBR-11-1.2	bulk	-0.60	-2.17	-0.12	0.70826	0.512297	-6.7	-	-	-
OBR-11-1.2	leachate	-	-	-	0.70791	0.512319	-6.2	-	-	-
OBR-11-1.2	residue	-	-	-	0.70967	0.512265	-7.3	18.534	15.622	38.405
OBR-11-1.2p	pisolith separate, bulk	3.60	-2.77	-0.35	-	-	-	-	-	-
OBR-11-1.2p	pisolith separate, leachate	-	-	-	0.70788	0.512324	-6.1	18.420	15.605	38.258
OBR-11-1.8	bulk	2.10	-2.31	0.16	0.70861	0.512233	-7.9	18.862	15.649	38.956
OBR-11-1.8	leachate	-	-	-	0.70789	0.512297	-6.7	18.794	15.654	38.703
OBR-11-1.8p	pisolith separate, bulk	-1.54	-2.12	0.13	-	-	-	-	-	-
OBR-11-1.8p	pisolith separate, leachate	-	-	-	0.70787	0.512288	-6.8	18.721	15.641	38.609
OBR-11-2.8	bulk	-0.80	-0.81	-0.15	0.70901	0.512279	-7.0	18.833	15.646	38.756
OBR-11-2.8	leachate	-	-	-	0.70812	0.512329	-6.0	18.785	15.653	38.690
OBR-11-3.8	bulk	0.82	-1.07	0.00	0.70937	0.512279	-7.0	-	-	-
OBR-11-3.8	leachate	-	-	-	0.70798	0.512306	-6.5	-	-	-
OBR-11-3.8p	pisolith separate, bulk	1.20	-1.01	-0.02	-	-	-	-	-	-
OBR-11-3.8p	pisolith separate, leachate	-	-	-	0.70798	0.512304	-6.5	18.459	15.614	38.329
OBR-11-4.4	bulk	-1.02	-1.05	-0.07	0.70902	0.512271	-7.2	18.922	15.662	38.776
OBR-11-4.4	leachate	-	-	-	0.70793	0.512282	-6.9	18.885	15.668	38.723
OBR-11-4.4p	pisolith separate, bulk	-0.66	-1.18	-0.42	-	-	-	-	-	-

OBR-11-4.4p	pisolith separate, leachate	-	-	-	0.70793	0.512317	-6.3	18.889	15.658	38.669
OBR-11-5.1	bulk	-4.91	-2.09	-0.16	0.70917	0.512293	-6.7	18.938	15.662	38.750
OBR-11-5.1	leachate	-	-	-	0.70796	0.512327	-6.1	18.915	15.672	38.728
OBR-11-5.1p	pisolith separate, bulk	-7.43	-2.03	-0.44	-	-	-	-	-	-
OBR-11-5.1p	pisolith separate, leachate	-	-	-	0.70793	0.512314	-6.3	18.846	15.655	38.651
OBR-11-6.1	bulk	-20.3	-3.34	0.08	0.70921	0.512224	-8.1	18.974	15.671	38.788
OBR-11-6.1	leachate	-	-	-	0.70796	0.512282	-6.9	19.017	15.687	38.755
OBR-11-6.1p	pisolith separate, bulk	-24.8	-2.09	-0.24	0.70808	0.512263	-7.3	19.050	15.679	38.777
OBR-11-6.1p	pisolith separate, residue	-	-	-	-	0.512205	-8.4	19.153	15.685	38.873

[a] In bold italic, samples from the host strata; in regular, samples from the Mn-ore layer.

Table 6

Geochemistry of Oligocene Mn-deposits around the Black Sea.

deposit	Binkiliç		Chiatura-Kvirila		Laba (Labinsk)	Mangyshlak	
facies	oxide	carbonate	oxide	carbonate	carbonate	oxide	carbonate
age (Ma)	28	28	28	28	28	28	28
country	Turkey	Turkey	Georgia	Georgia	Russia	Kazakhstan	Kazakhstan
host rock	limestone	limestone	sandstone	sandstone	sand	calcareous sandstone	calcareous sandstone
predominant ore mineral	cryptomelane	rhodochrosite	manganite	rhodochrosite	rhodochrosite	pyrolusite	rhodochrosite
# of analyses	19	11	11	30	24	15	24
MnO (wt.%)	53.5	35.3	48.4	30.6	32.9	39.8	29.2
$Fe_2O_{3\ tot}$ (wt.%)	2.92	5.92	1.63	3.33	3.88	3.48	2.61
SiO_2 (wt.%)	7.47	8.26	14.7	18.6	-	-	35.5
Al_2O_3 (wt.%)	2.47	2.27	3.52	3.59	-	-	5.72
CaO (wt.%)	15.1	18.4	5.25	9.56	9.85	-	11.6
MgO (wt.%)	0.94	1.05	1.86	3.07	1.39	-	1.22
K_2O (wt.%)	0.33	0.49	0.50	0.55	-	-	1.70
Na_2O (wt.%)	0.43	0.27	0.49	0.55	-	-	1.91
P_2O_5 (wt.%)	0.74	0.32	0.22	1.14	0.04	0.09	0.48
TiO_2 (wt.%)	0.56	0.38	0.17	0.24	-	-	0.17
LOI (wt.%)	13.4	25.3	16.6	26.8	39.6	-	13.8
Ba (ppm)	4249	5505	9578	785	-	-	-
Co (ppm)	85	72	21	49	13	68	8
Cr (ppm)	15	7	-	-	19	20	21
Cu (ppm)	93	64	24	69	22	60	18
Ni (ppm)	195	203	527	401	151	175	36
Pb (ppm)	46	43	26	22	-	-	-
Sr (ppm)	2232	2719	-	-	-	-	-
V (ppm)	44	91	-	-	37	86	-
Y (ppm)	14	17	-	-	-	-	-
Zn (ppm)	60	57	102	142	53	-	-
Zr (ppm)	53	35	-	-	-	-	-
Ce/Ce*	0.77	0.74	-	-	-	-	-

Eu/Eu*	2.78	1.62	-	-	-	-	-
Ce/Ce* (at Al=0)	0.80	0.81	-	-	-	-	-
Eu/Eu* (at Al=0)	3.33	1.78	-	-	-	-	-
C_{carb} (wt.%)	-	-	8.03	18.5	-	-	5.79
C_{org} (wt.%)	-	-	-	-	-	-	0.29
$\delta^{13}C_{cct}{}^{a}$ (‰ PDB)	-	-5.10	-7.10	-12.5	-	-	-5.98
$\delta^{13}C_{rhod}{}^{b}$ (‰ PDB)	-	-6.61	-10.1	-10.5	-	-	-10.3
$\delta^{18}O_{cct}$ (‰ PDB)	-	-8.05	-7.11	-4.32	-	-	-2.51
$\delta^{18}O_{rhod}$ (‰ PDB)	-	-6.39	-5.32	-4.40	-	-	-0.99
References	Öztürk and Frakes, 1995; Gültekin, 1998; Gültekin and Balcı, 2018		Varentsov and Rakhmanov, 1980; Kuleshov and Dombrovskaya, 1997		Kalinenko et al., 1965	Kuleshov, 2003; 2017	

[a] $\delta^{13}C_{cct} = \delta^{13}C_{calcite}$ (similarly, $\delta^{18}O_{cct} = \delta^{18}O_{calcite}$)
[b] $\delta^{13}C_{rhod} = \delta^{13}C_{rhodochrosite}$ (similarly, $\delta^{18}O_{rhod} = \delta^{18}O_{rhodochrosite}$)

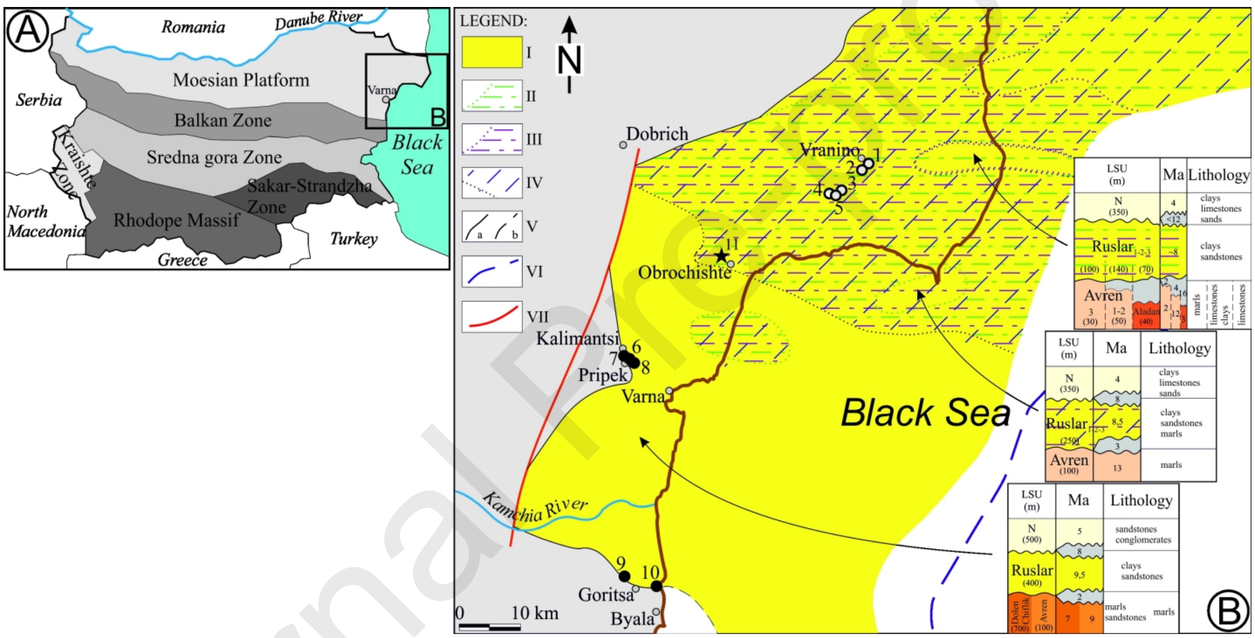

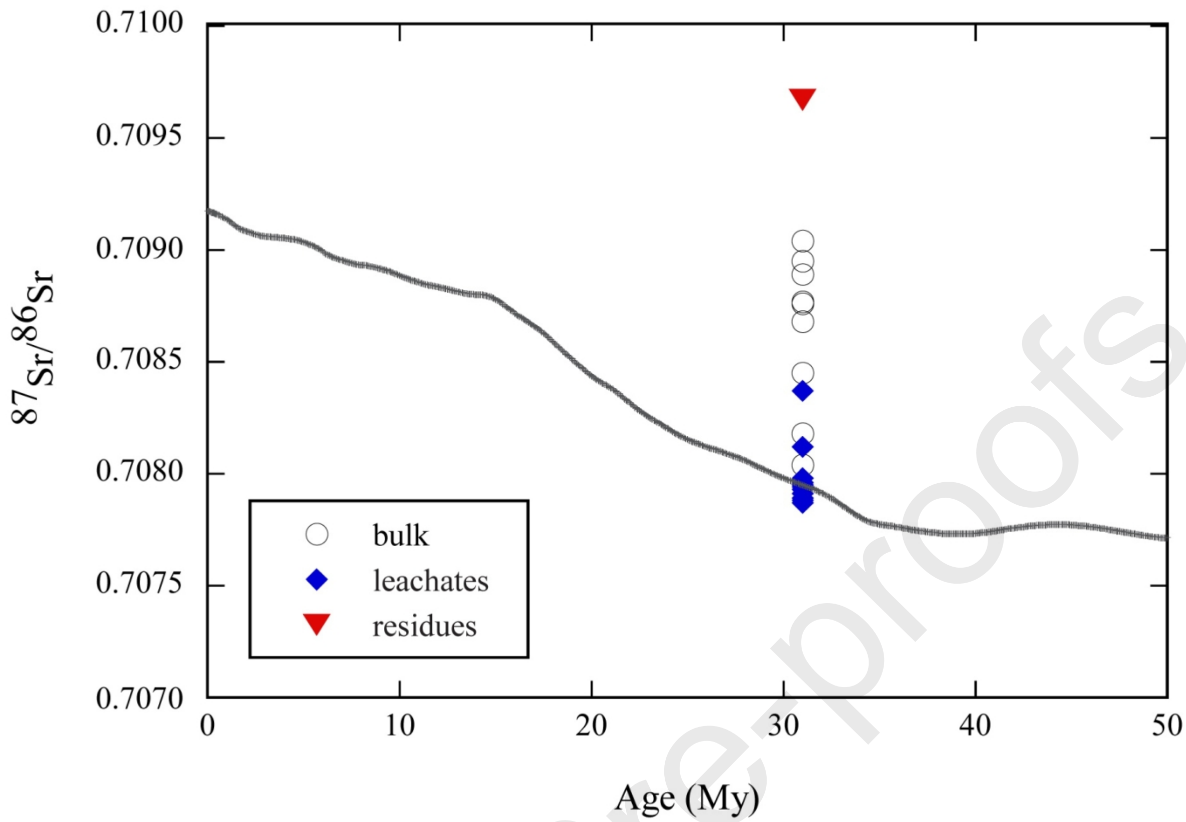
0.7100
0.7095
0.7090
0.7085
0.7080
0.7075
0.7070
$^{87}Sr/^{86}Sr$
bulk
leachates
residues
0
10
20
30
40
50
Age (My)

1573

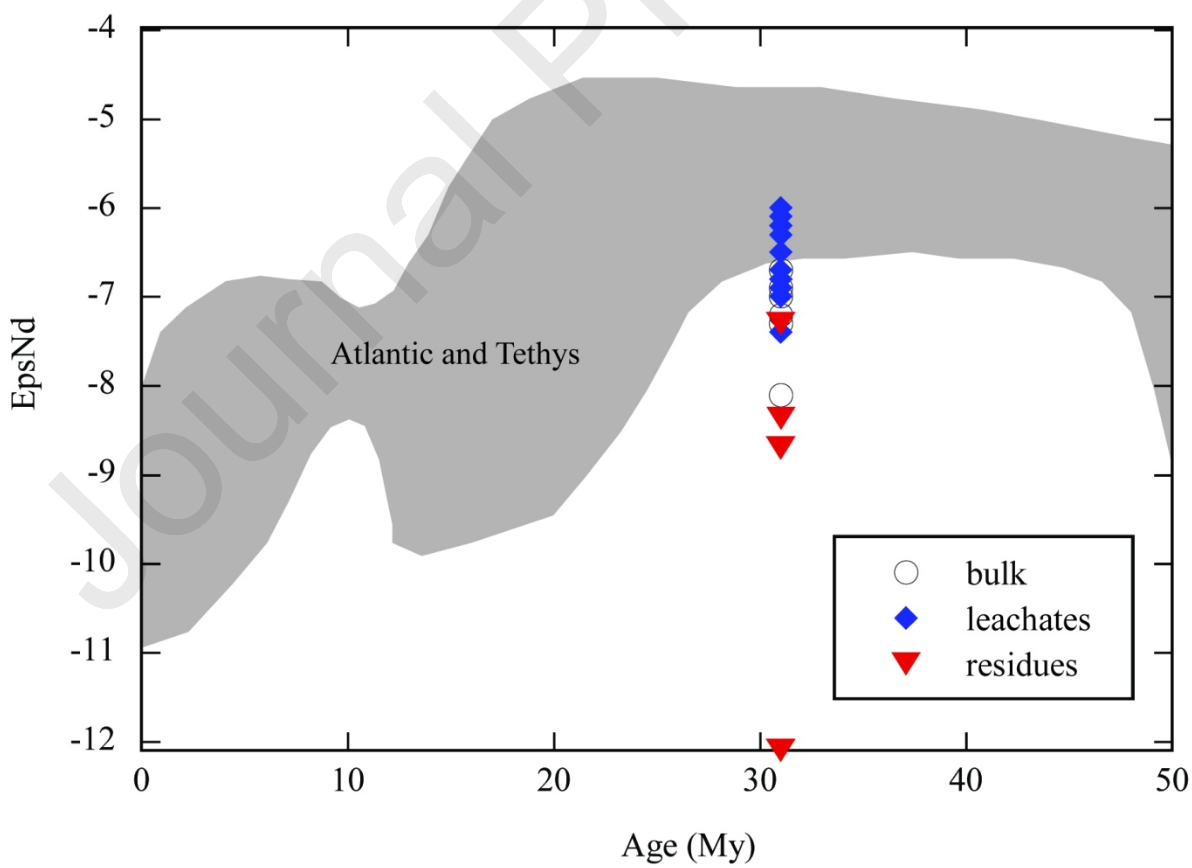
-4
-5
-6
-7
-8
-9
-10
-11
-12
EpsNd
Atlantic and Tethys
bulk
leachates
residues
0
10
20
30
40
50
Age (My)

1574

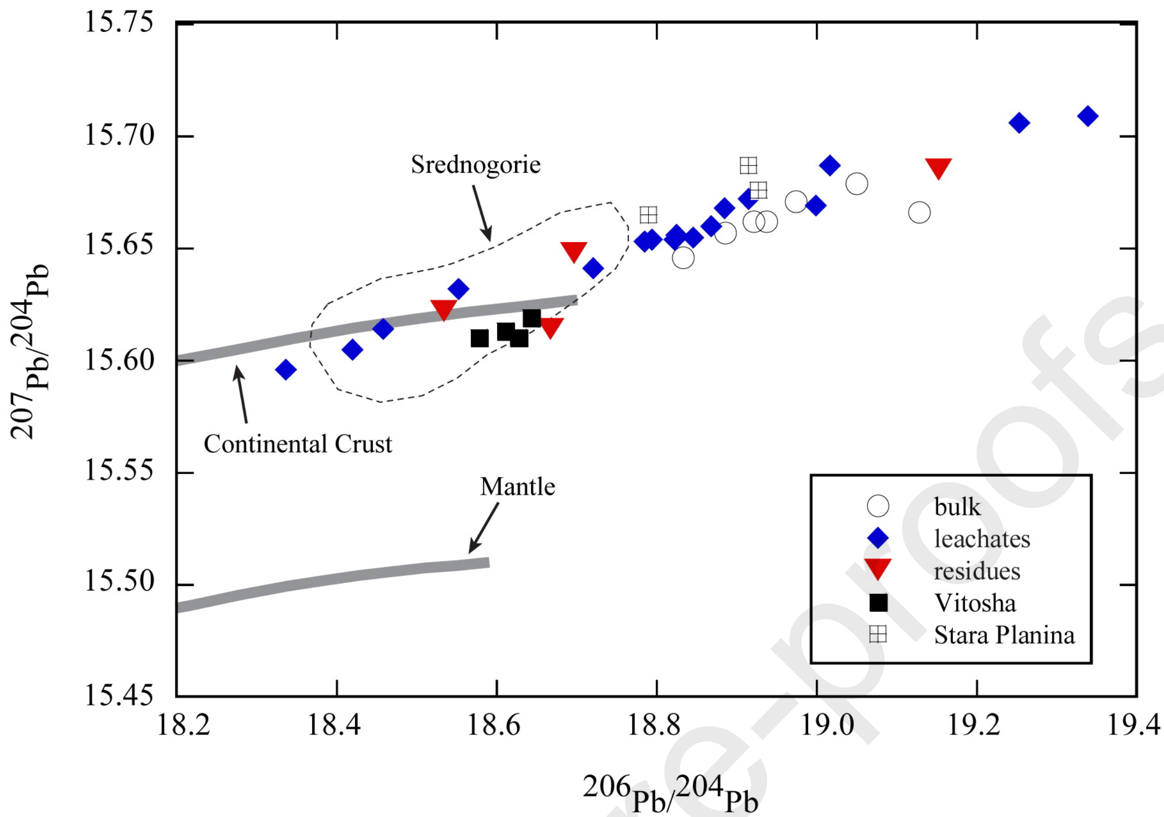

15.75
15.70
15.65
15.60
15.55
15.50
15.45
18.2
18.4
18.6
18.8
19.0
19.2
19.4
$^{207}Pb/^{204}Pb$
$^{206}Pb/^{204}Pb$
Srednogorie
Continental Crust
Mantle
bulk
leachates
residues
Vitosha
Stara Planina

1575

1576

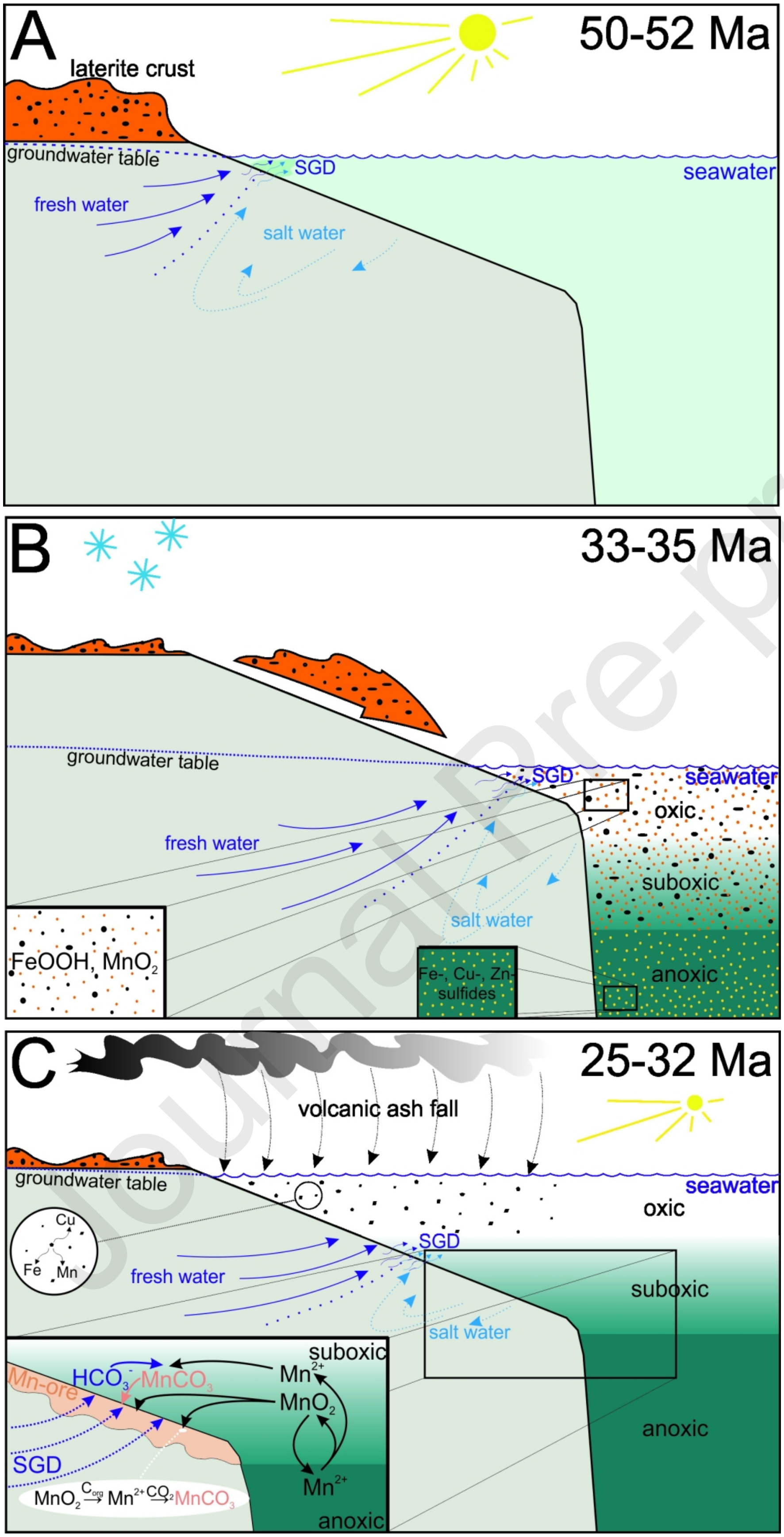
A
50-52 Ma
laterite crust
groundwater table
SGD
seawater
fresh water
salt water
B
33-35 Ma
groundwater table
SGD
seawater
oxic
fresh water
suboxic
salt water
FeOOH, MnO2
Fe-, Cu-, Zn-sulfides
anoxic
C
25-32 Ma
volcanic ash fall
groundwater table
seawater
oxic
Cu
Fe
Mn
SGD
fresh water
suboxic
salt water
suboxic
Mn-ore
HCO3-
MnCO3
Mn2+
MnO2
SGD
Mn2+
MnO2 Corg Mn2+ CO2 MnCO3
anoxic
anoxic

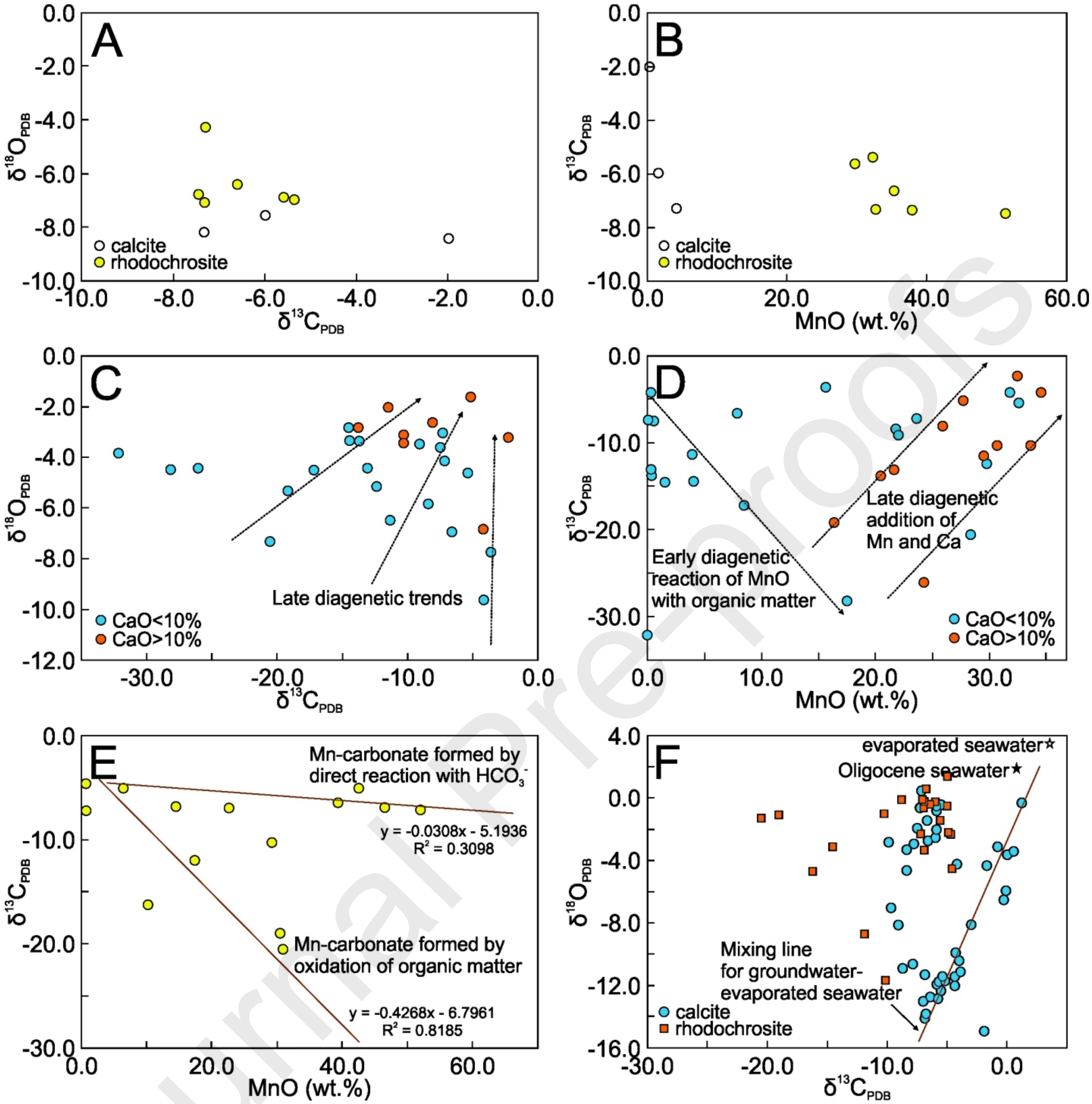
A
calcite
rhodochrosite
δ18OPDB
δ13CPDB
B
calcite
rhodochrosite
δ13CPDB
MnO (wt.%)
C
Late diagenetic trends
CaO<10%
CaO>10%
δ18OPDB
δ13CPDB
D
Late diagenetic addition of Mn and Ca
Early diagenetic reaction of MnO with organic matter
CaO<10%
CaO>10%
δ13CPDB
MnO (wt.%)
E
Mn-carbonate formed by direct reaction with HCO3-
y = -0.0308x - 5.1936
R2 = 0.3098
Mn-carbonate formed by oxidation of organic matter
y = -0.4268x - 6.7961
R2 = 0.8185
δ13CPDB
MnO (wt.%)
F
evaporated seawater
Oligocene seawater
Mixing line for groundwater-evaporated seawater
calcite
rhodochrosite
δ18OPDB
δ13CPDB

1577

1578

1579

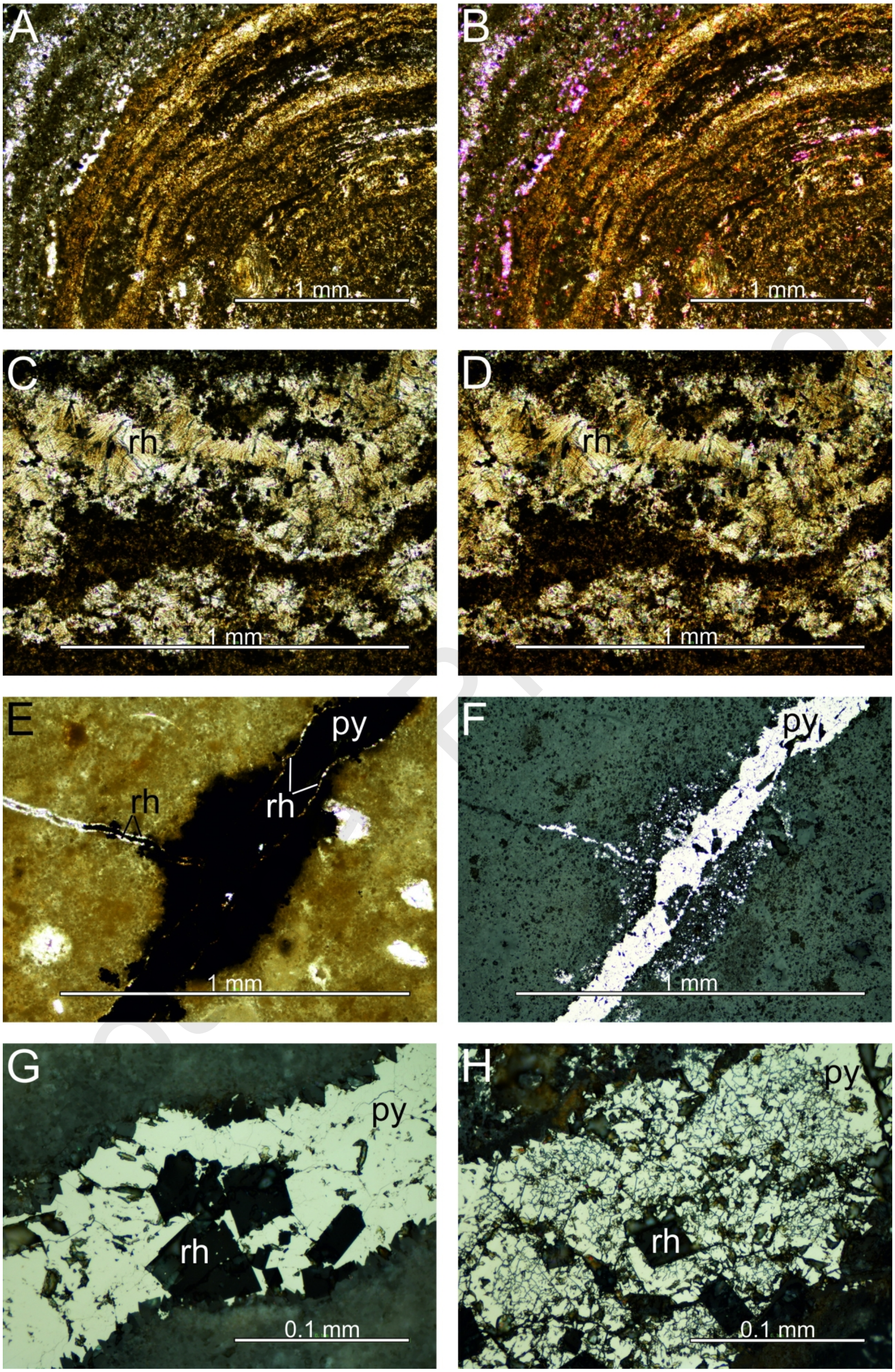
A
1 mm
B
1 mm
C
rh
1 mm
D
rh
1 mm
E
py
rh
rh
1 mm
F
py
1 mm
G
py
rh
0.1 mm
H
py
rh
0.1 mm

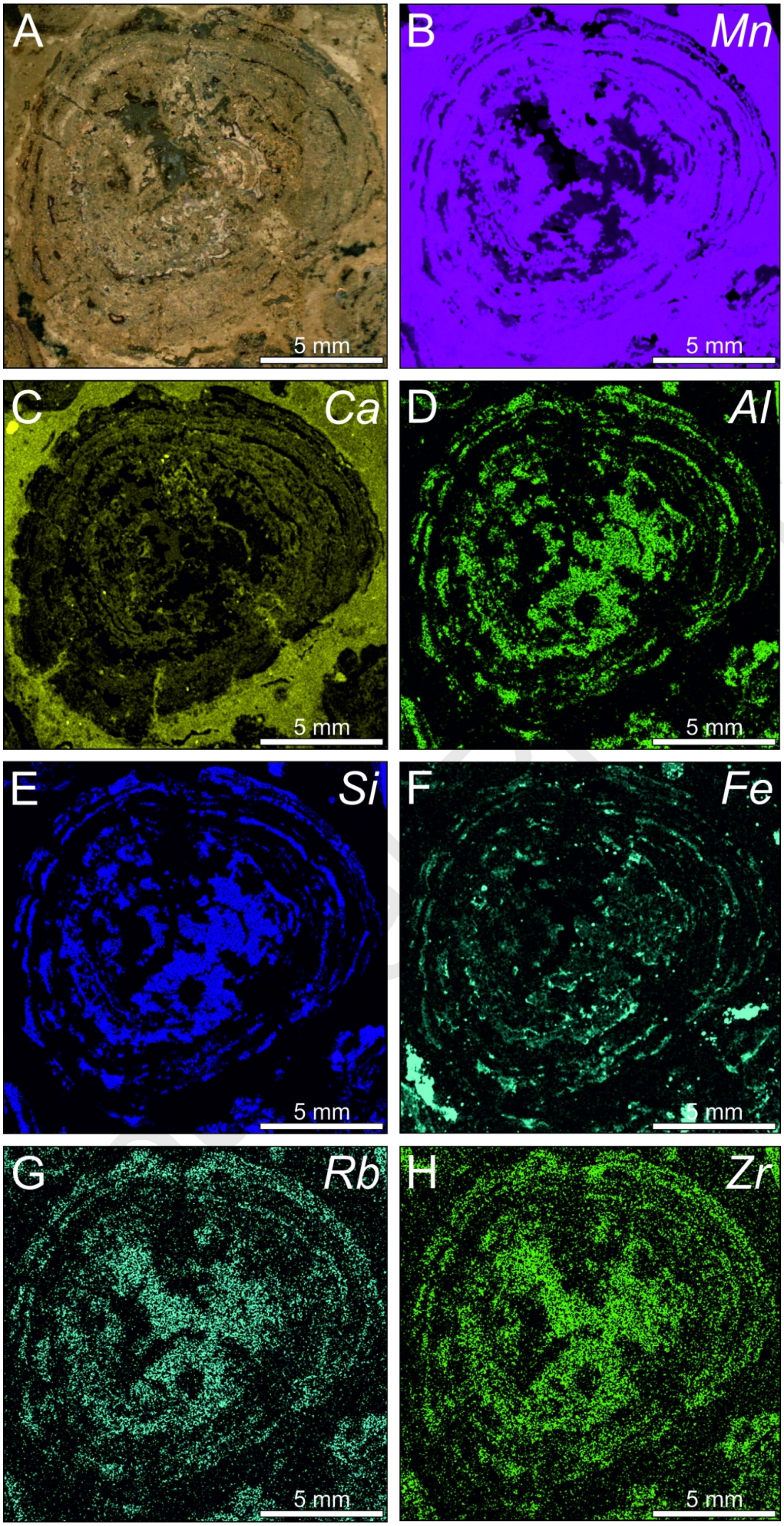

1580

1581 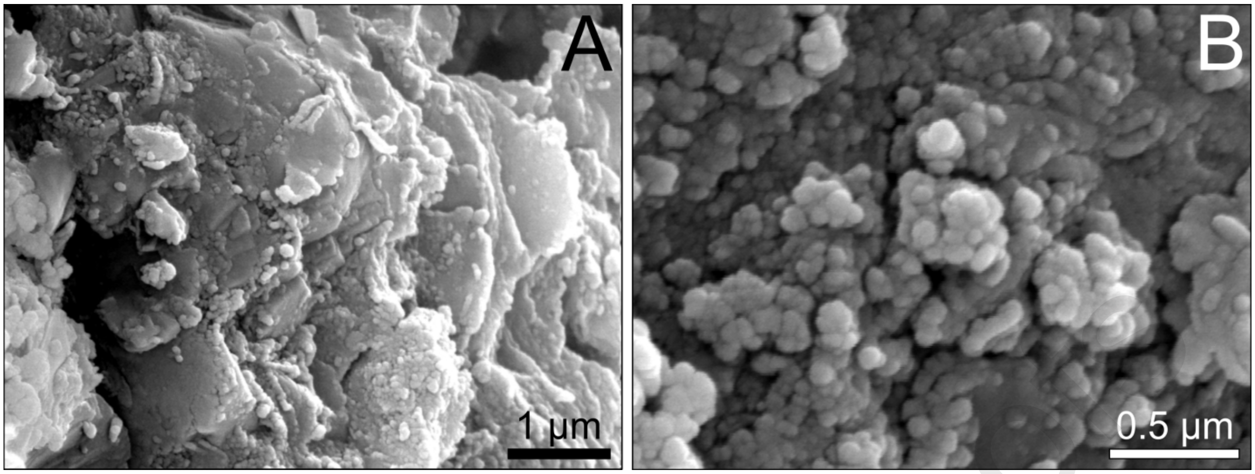

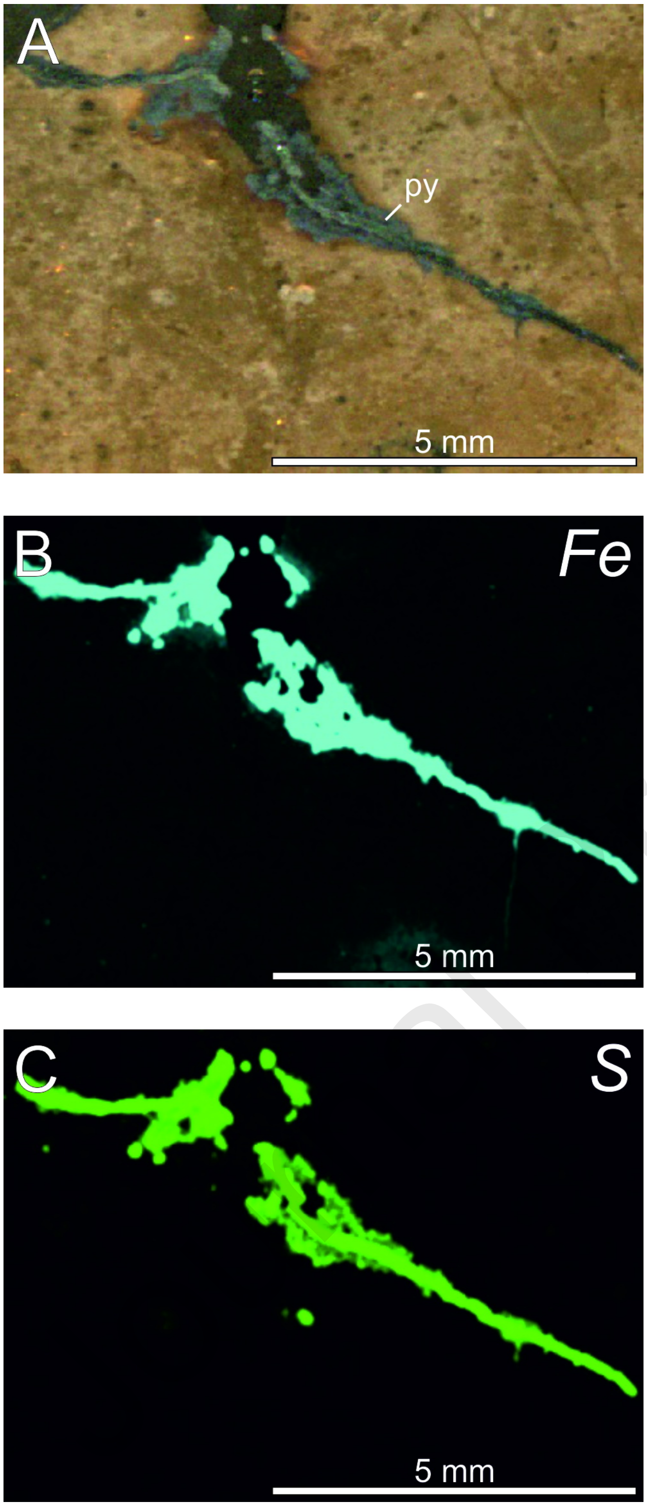
A
py
5 mm
B
Fe
5 mm
C
S
5 mm

1583

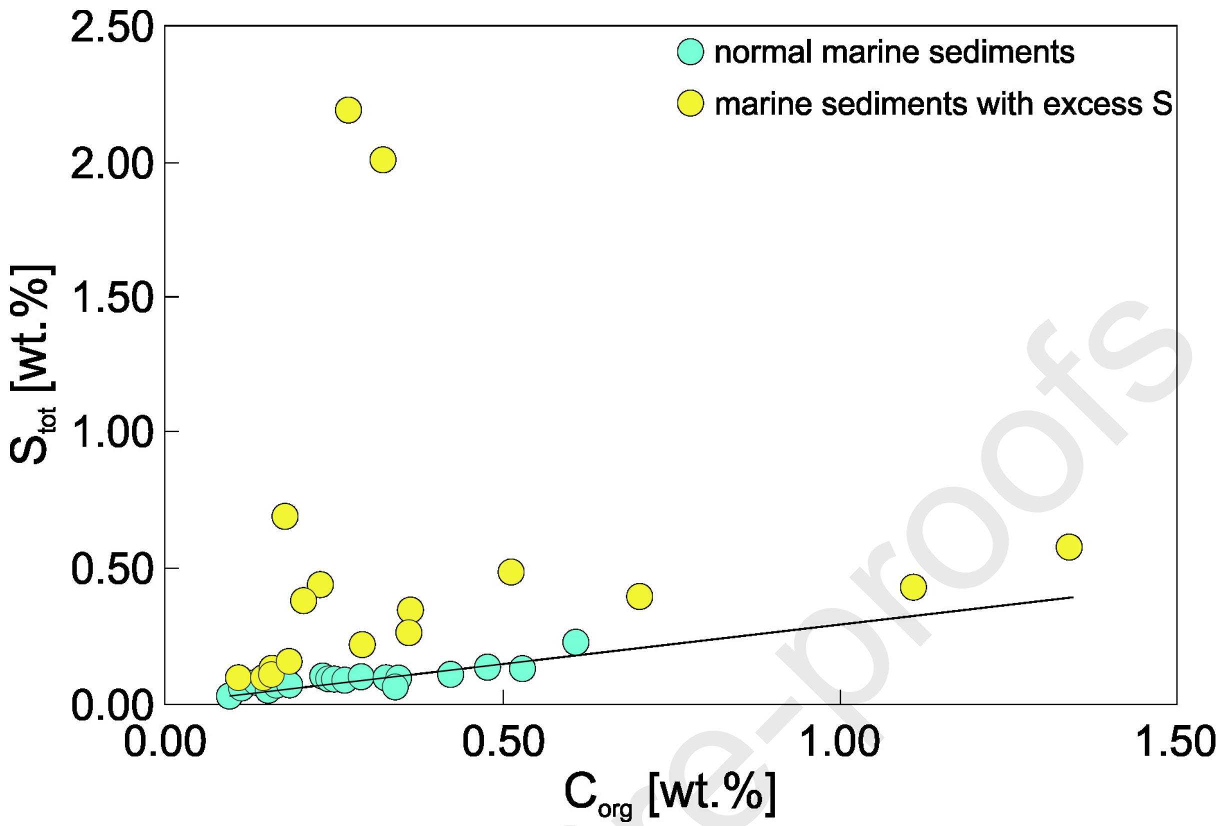

normal marine sediments
marine sediments with excess S
S_{tot} [wt.%]
C_{org} [wt.%]
0.00
0.50
1.00
1.50
2.00
2.50
0.00
0.50
1.00
1.50

1584

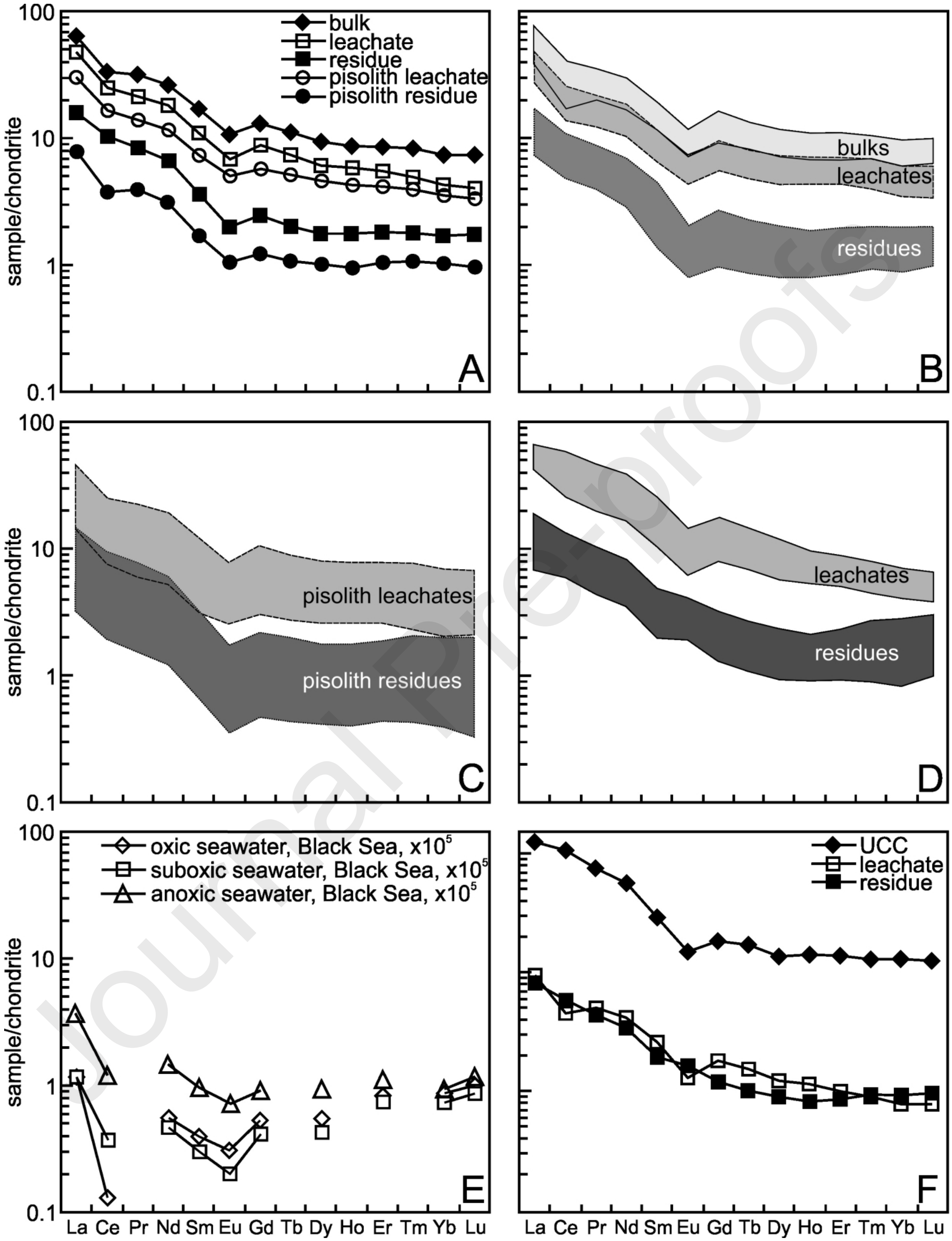

bulk
leachate
residue
pisolith leachate
pisolith residue
A
bulks
leachates
residues
B
pisolith leachates
pisolith residues
C
leachates
residues
D
oxic seawater, Black Sea, x10^5
suboxic seawater, Black Sea, x10^5
anoxic seawater, Black Sea, x10^5
E
UCC
leachate
residue
F
sample/chondrite
100
10
1
0.1
La Ce Pr Nd Sm Eu Gd Tb Dy Ho Er Tm Yb Lu

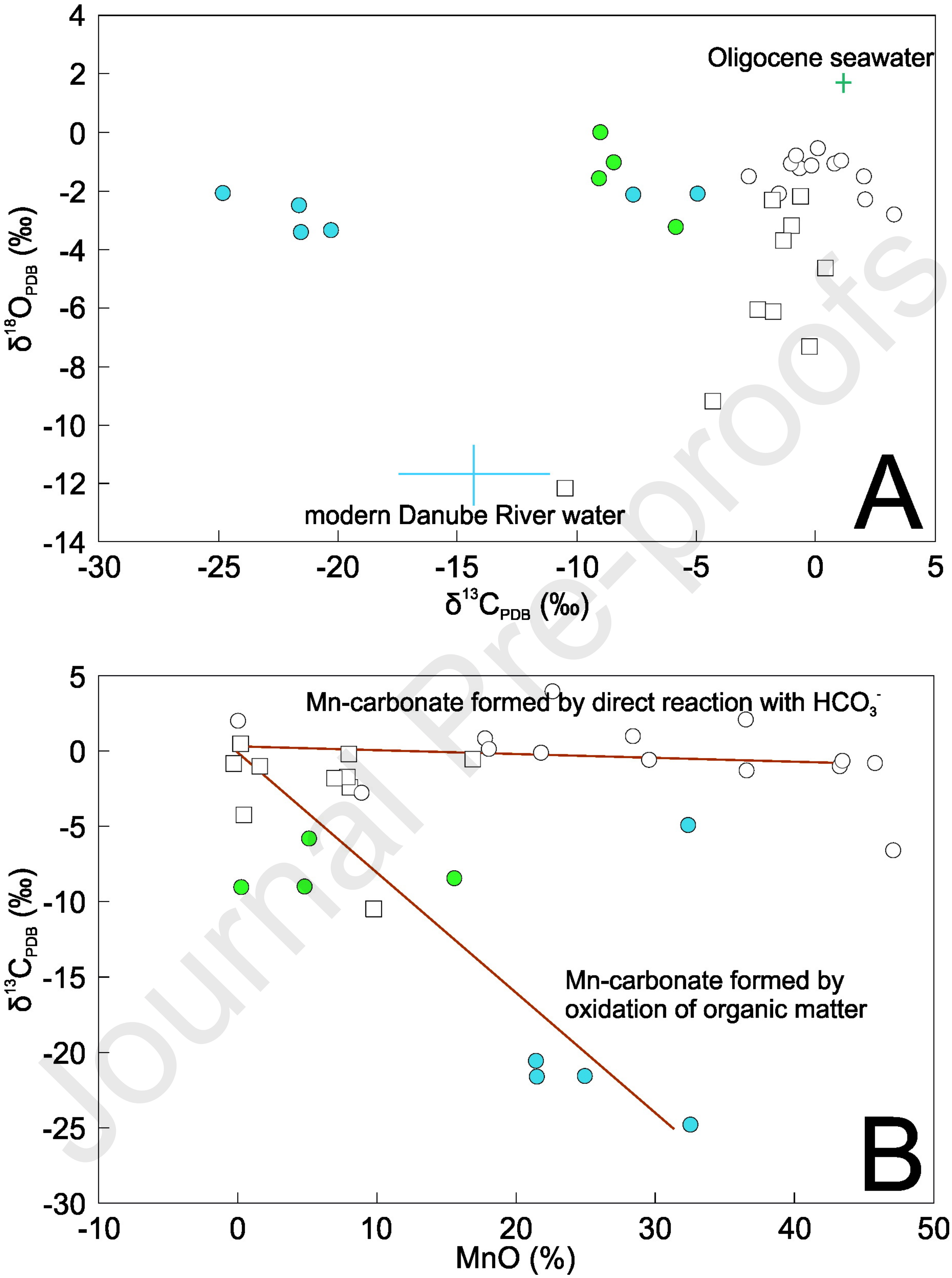
Oligocene seawater
modern Danube River water
A
$\delta^{18}O_{PDB}$ (‰)
$\delta^{13}C_{PDB}$ (‰)
Mn-carbonate formed by direct reaction with HCO_3^-
Mn-carbonate formed by oxidation of organic matter
B
$\delta^{13}C_{PDB}$ (‰)
MnO (%)

1586 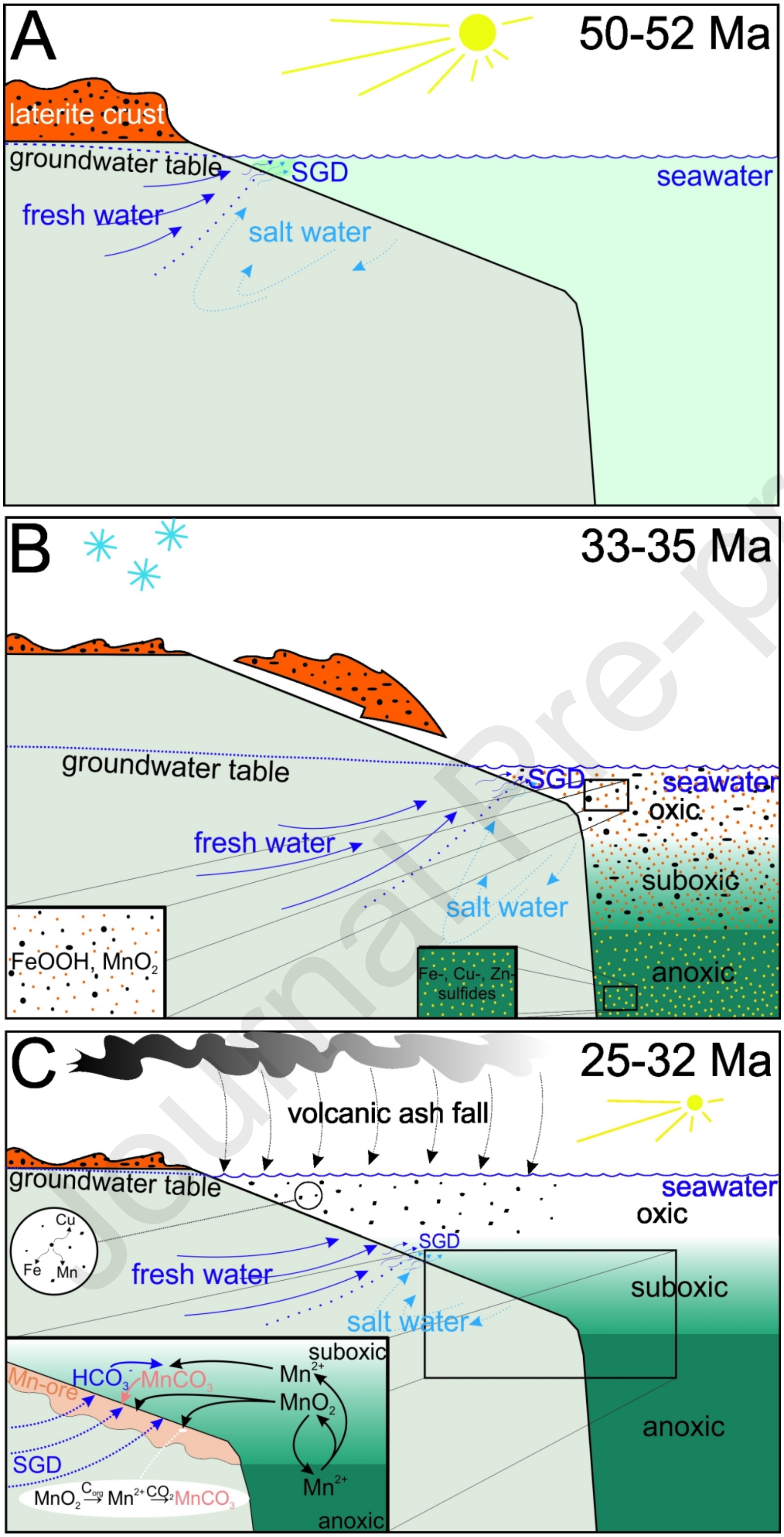
A
50-52 Ma
laterite crust
groundwater table
SGD
seawater
fresh water
salt water
B
33-35 Ma
groundwater table
SGD
seawater
oxic
suboxic
fresh water
salt water
anoxic
FeOOH, MnO2
Fe-, Cu-, Zn-sulfides
C
25-32 Ma
volcanic ash fall
groundwater table
seawater
oxic
Cu
Fe
Mn
SGD
fresh water
suboxic
salt water
anoxic
suboxic
Mn-ore
HCO3
MnCO3
Mn2+
MnO2
Mn2+
SGD
anoxic